

# Part 2: Strength and Fatigue Life Prediction for a Composite Structural Beam

## Table of Contents

<b>1</b>	<b>INTRODUCTION.....</b>	<b>1</b>
1.1	BACKGROUND .....	1
1.1.1	Strongwell’s 36 inch Double Web Beam.....	1
1.1.2	Strength and Life Prediction by Senne .....	2
1.2	LITERATURE REVIEW .....	5
1.2.1	Failure Mechanisms in FRP Composite Beams.....	5
1.2.2	Free Edge Delamination .....	5
1.2.3	Delamination at Ply Drop-Offs or Laminate Tapers.....	8
1.2.4	The Fracture Mechanics Approach to Delamination .....	9
1.2.5	Delamination in Composite Structures .....	11
1.2.6	Fatigue Life Prediction of Composite Structures.....	11
1.3	SUMMARY .....	13
1.4	OBJECTIVES .....	13
<b>2</b>	<b>STRENGTH PREDICTION: METHODS.....</b>	<b>15</b>
2.1	FAILURE TESTS .....	15
2.2	STRESS ANALYSIS USING THE FINITE ELEMENT METHOD .....	16
2.2.1	Global Model .....	16
2.2.2	Free Edge Submodels .....	17
2.2.3	Flange Taper Submodels.....	19
2.2.4	Detailed Flange/Web Junction Model .....	21
2.3	STRENGTH PREDICTION.....	21
2.3.1	Compression Failure .....	21
2.3.2	Delamination Failure .....	22
2.3.3	Effect of Geometry and Span Dependence.....	25
2.3.4	Uniform Loading .....	25
2.3.5	Fracture Mechanics Approach .....	25
<b>3</b>	<b>STRENGTH PREDICTION: RESULTS .....</b>	<b>27</b>
3.1	FAILURE TESTS.....	27
3.2	STRESS ANALYSIS.....	28
3.2.1	Global Model .....	28
3.2.2	Free Edge Submodels .....	29
3.2.3	Flange Taper Sub-models .....	31
3.2.4	Detailed Flange/Web Junction Model .....	33
3.3	STRENGTH PREDICTION.....	34
3.3.1	Compression Failure .....	34
3.3.2	Delamination Failure .....	34
3.3.3	Effect of Geometry and Span Dependence.....	36
3.3.4	Uniform Loading .....	37
3.4	SUMMARY .....	37

<b>4</b>	<b>FATIGUE LIFE PREDICTIONS .....</b>	<b>39</b>
4.1	INTEGRATION OF STRESS ANALYSIS INTO LIFE PREDICTION CODE.....	39
4.1.1	ANSYS® code.....	39
4.1.2	Critical Element .....	39
4.1.3	Off-Axis Stiffness Reduction.....	41
4.1.4	Ply-Level Stresses Calculations.....	43
4.1.5	Procedure .....	44
4.2	FATIGUE PREDICTIONS FOR THE DWB.....	45
4.3	FATIGUE TESTS.....	45
4.4	RESULTS .....	46
<b>5</b>	<b>CONCLUSIONS AND FUTURE WORK.....</b>	<b>48</b>
	<b>FIGURES AND TABLES .....</b>	<b>50</b>
	<b>REFERENCES.....</b>	<b>111</b>
	<b>VITA.....</b>	<b>117</b>

## List of Tables

Table 1. Ply strength values used in the strength and life analyses. ....	100
Table 2. Summary of $F_a$ ranges for off-axis plies at three applied load levels.....	101

## List of Figures

Figure 1. Strongwell's 36 inch DWB (dimensions in inches). ....	50
Figure 2. Four-point bend test set-up for 36 inch DWB (18.3 m or 60 ft span shown).....	51
Figure 3. Failure of the compressive flange of a 36 inch DWB under the loading patch.....	51
Figure 4. Sub-laminate construction of the DWB's flange. Arrows indicate possible delamination sites.....	51
Figure 5. 8 inch DWB fatigue curves: prediction vs. data.....	52
Figure 6. Locations of crack detection gages.....	52
Figure 7. Half-beam model used in FE global analysis (11.9 m span).....	53
Figure 8. Cross-section of global DWB model, showing the location of the elements used in the stress calculations.....	53
Figure 9. Close-up of load patch showing locations of EDGESUB1 (in red). ....	54
Figure 10. End view of DWB showing lay-up detail on both sides of flange. ....	54
Figure 11. Cross-section view of global FE model used for the taper region stress analysis.....	55
Figure 12. Intermediate FE submodel (EDGESUB1) used for the taper region stress analysis..	55
Figure 13. Detailed FE submodel (TAPERSUB2) used in the taper region stress analysis.....	56
Figure 14. Close-up of TAPERSUB2 taper region showing fillet detail.....	56
Figure 15. TAPERSUB3 used in the taper analyses.....	57
Figure 16. Detailed representation of the flange/web junction.....	57
Figure 17. Tensile test specimen to obtain $S_z$ at primary carbon/glass interface.....	58
Figure 18. FEA model of SBS test on flange coupon. Colored contours indicate transverse shear stress, $\tau_{xz}$ . ....	58

Figure 19. Finite element model for the uniform distributed loading case, showing how the load was introduced (area pressure loads indicated by the arrows).....	59
Figure 20. Possible delamination at the taper in two different beams. (Samples taken from near the end of the delamination.) .....	59
Figure 21. Span dependence of the shear capacity for both the 8 inch and 36 inch DWB's.....	60
Figure 22. Span dependence of the moment capacity for both the 8 inch and 36 inch DWB's. The moment capacity has been normalized with respect to the maximum (long span) value to better demonstrate the variation for the 8 inch DWB. ....	61
Figure 23. Axial strain through the thickness of the top flange in the constant moment region of an 11.9 m (39 ft) beam under four-point loading, as predicted using the global FE model and two different MLB/Timoshenko solutions: point loading and patch loading. ....	62
Figure 24. Axial stress through the thickness of the top flange in the constant moment region of an 11.9 m (39 ft) beam under four-point loading, as predicted using the global FE model and two different MLB/Timoshenko solutions: point loading and patch loading. ....	63
Figure 25. Failure function in the outer carbon plies of the top flange, demonstrating the stress concentration at the load patches in a four-point loading test using load patches. (Half-beam schematic at top illustrates geometry for 6.1 m beam only.) .....	64
Figure 26. Qualitative comparison of the FEA predicted and experimentally observed pressure distributions under a load patch. ....	65
Figure 27. The interlaminar normal stress $\sigma_z$ through the thickness of the top flange at the free edge at various locations along the length of an 11.9 m (39 ft) beam under four-point loading.....	66
Figure 28. The interlaminar shear stress $\tau_{xz}$ through the thickness of the top flange at the free edge of the top flange at various locations along the length of an 11.9 m (39 ft) beam under four-point loading. ....	67
Figure 29. The interlaminar shear stress $\tau_{yz}$ through the thickness of the top flange at the free edge of the top flange at various locations along the length of an 11.9 m (39 ft) beam under four-point loading. ....	68
Figure 30. Interlaminar normal stress profiles across the width of at the primary carbon/glass interface in the vicinity of the free edge. ....	69
Figure 31. Close-up of free edge region in Figure 30.....	70
Figure 32. Free edge interlaminar stress profiles at the interface of $\pm 45^\circ$ plies (445 kN, $\Delta T = -114^\circ\text{C}$ ). ....	71

Figure 33. Comparison of the y-direction profiles for the free edge interlaminar tensile stress $\sigma_z$ for $\Delta T = -114\text{ }^\circ\text{C}$ and $\Delta T = 0$ at $x = 419\text{ cm}$ and at mid-span.....	72
Figure 34. Comparison of y-direction profiles for the free edge interlaminar tensile stress $\tau_{xz}$ for $\Delta T = -205$ and $\Delta T = 0$ at $x = 165\text{ inches}$ and mid-span.....	73
Figure 35. Comparison of the y-direction profiles for the interlaminar shear stresses $\tau_{xz}$ and $\tau_{yz}$ at the primary carbon/glass interface for $\Delta T = -114\text{ }^\circ\text{C}$ and $\Delta T = 0$ at $x = 419\text{ cm}$ .....	74
Figure 36. Effect of $\Delta T$ on the free edge $\sigma_z$ profile at the interface between the glass $\pm 45^\circ$ plies. .....	75
Figure 37. Effect of $\Delta T$ on the free edge $\tau_{xz}$ profile at the interface between the glass $\pm 45^\circ$ plies. .....	76
Figure 38. Contour plot of interlaminar normal stress $\sigma_z$ in the flange taper region.....	77
Figure 39. Contour plot of interlaminar normal stress $\sigma_z$ in the flange taper region (outer carbon/CSM sublaminates only shown).....	77
Figure 40. Interlaminar stress profiles at the primary carbon/glass interface across the width of TAPERSUB2 at MID-SPAN (dashed lines correspond to the taper and web coordinates, as shown in the schematic above). ....	78
Figure 41. Interlaminar stress profiles at the primary carbon/glass interface across the width of TAPERSUB2 near a LOAD PATCH ( $x = 424\text{ cm}$ or $167.5\text{ inches}$ ).....	79
Figure 42. Comparison of the interlaminar normal stress $\sigma_z$ along the primary carbon/glass interface at the taper tip at the mid-span and load patch ( $x = 424\text{ cm}$ or $166.75\text{ inches}$ ) locations. ....	80
Figure 43. Interlaminar normal stress profile at the primary carbon/glass interface in the vicinity of the taper near the load patch ( $x = 424\text{ cm}$ or $166.75\text{ inches}$ ).....	81
Figure 44. Mechanical ( $444\text{ kN}$ or $100\text{ kips}$ ) and thermal ( $\Delta T = -114\text{ }^\circ\text{C}$ or $-205\text{ }^\circ\text{F}$ ) components of the interlaminar normal stress at the primary carbon/glass interface in the vicinity of the taper at the load patch. ....	82
Figure 45. $F_a$ in carbon plies in the taper region as a function of distance from the free edge of the taper ( $444\text{ kN}$ or $100\text{ kips}$ load per patch and $\Delta T = -114\text{ }^\circ\text{C}$ or $-205\text{ }^\circ\text{F}$ ).....	83
Figure 46. $F_a$ in carbon plies in the taper region as a function of distance from the free edge of the taper (thermal loading only: $\Delta T = -114\text{ }^\circ\text{C}$ or $-205\text{ }^\circ\text{F}$ ).....	84
Figure 47. Comparison of detailed flange/web junction model with TAPERSUB 2 results: $\sigma_z$ at mid-span.....	85

Figure 48. Comparison of detailed flange/web junction model with TAPERSUB 2 results: $\tau_{yz}$ at mid-span.....	86
Figure 49. Comparison of detailed flange/web junction model with TAPERSUB 2 results: $\sigma_z$ near the load patch ( $x = 424$ cm or 166.75 inches).....	87
Figure 50. Comparison of detailed flange/web junction model with TAPERSUB 2 results: $\tau_{yz}$ near the load patch ( $x = 424$ cm or 166.75 inches).....	88
Figure 51. Effect of sub-laminate refinement on the interlaminar shear stresses at the third-point in the SBS flange specimen. ....	89
Figure 52. Effect of sub-laminate refinement on the interlaminar normal stresses at the third-point in the SBS flange specimen. ....	90
Figure 53. Effect of thermal change on the distribution of the interlaminar shear stress through the flange thickness in the SBS test (at $x = L/3$ ).....	91
Figure 54. Comparison of the predicted shear capacity vs. span length for the compressive failure mode and the experimental results. ....	92
Figure 55. Comparison of the predicted moment capacity vs. span length for the compressive failure mode and the experimental results. ....	93
Figure 56. Effect of stress concentration on moment to failure.....	94
Figure 57. Comparison of the predicted shear capacity vs. span length for the taper edge delamination failure mode using the ply width stress averaging technique and the experimental results. ....	95
Figure 58. Comparison of the predicted moment capacity vs. span length for the taper edge delamination failure mode using the ply width stress averaging technique and the experimental results. ....	96
Figure 59. Comparison of the predicted shear capacity vs. span length for the taper edge delamination failure mode using the volume stress averaging technique and the experimental results. ....	97
Figure 60. Comparison of the predicted moment capacity vs. span length for the taper edge delamination failure mode using the volume stress averaging technique and the experimental results. ....	98
Figure 61. Variation of failure function along the length of the bottom flange using the maximum stress criterion due to a uniformly distributed load (two span lengths shown). ..	99
Figure 62. Compression failure predictions for the 8 inch DWB using laminated beam theory. ....	100

Figure 63. Stiffness reduction data for the quasi-isotropic laminate of Post et al. [83] normalized with respect to ultimate failure load and life. ....	101
Figure 64. Stiffness reduction fit parameters $N_2$ , $m_1$ , and $m_2$ versus $F_a$ . ....	102
Figure 65. Stiffness reduction fit parameters $E_2$ and $N_1$ versus $F_a$ . ....	103
Figure 66. Estimated stiffness reduction curves extrapolated from the dynamic stiffness data of Reference [83]. ....	104
Figure 67. Effect of modeling $\Delta T$ on the ply-level, transverse stress along the length of half of the beam in the outer $90^\circ$ and CSM plies of the bottom flange (100 kips). ....	105
Figure 68. Zone definitions for applying stiffness reductions in off-axis plies. Axial strain for outermost carbon layer shown. ....	106
Figure 69. Predicted fatigue life S-N curve for the 11.9 m (39 ft) four-point loading geometry, compared with the experimental data and the carbon fiber fatigue life curve from Verghese [80]. ....	107
Figure 70. Normalized stiffness reduction vs. normalized life for three load levels. ....	108
Figure 71. Normalized stiffness reduction for the experimental fatigue test at 30% ultimate capacity. ....	109
Figure 72. Remaining strength curves for three load levels. ....	110

# 1 Introduction

Fiber-reinforced polymeric (FRP) composites are increasingly finding use in the areas of civil infrastructure and construction. Specifically, composites are being considered for structural elements such as girders and deck panels in bridge construction as lighter, more durable alternatives to steel and concrete. In order to match stiffness criteria previously met by steel designs, FRP sections which have a deep geometry or utilize carbon fiber are often necessary. The resulting sections will typically exhibit a high factor of safety on strength. Partly for this reason, the long-term durability of FRP in primary structural elements has not received considerable attention. Therefore, the durability of FRP materials in critical, load-bearing structures under the influence of variable environmental factors is not well understood. The polymer matrix, glass fibers, and fiber/matrix interface are susceptible to hygro-thermal degradation, UV damage, and visco-elastic changes such as creep. Furthermore, these damage mechanisms may have synergistic effects with damage caused by mechanical loading such as fatigue.

While experience in the design and applications of FRP structures continues to grow, little effort has been made to understand the fatigue performance and environmental durability of such systems. Most durability studies have been limited to coupon-level testing, and the development of life predictions for structures based on the kinetics of damage mechanisms in coupon specimens is rare. Furthermore, failure often occurs by way of local flange or web buckling, flange/web separation, or delamination within the flanges as opposed to fiber fracture. Therefore, macro-level coupon studies may fail to predict the ultimate failure at the structural level. Careful identification of the competing failure mechanisms in a structure is crucial to accurate strength and life predictions. This task is the primary focus of this study.

## 1.1 Background

### 1.1.1 Strongwell's 36 inch Double Web Beam

The current study is motivated by the need to understand and predict the performance of a particular structural member that has been developed for the infrastructure market. Strongwell Corporation of Bristol, Virginia has developed a 91 cm (36 inch) deep pultruded double web beam (DWB) for use in bridge construction (Figure 1). The beam is a hybrid laminated

composite, composed of both E-glass and carbon fibers in a vinyl ester resin. The DWB is intended for unsupported spans from 9.14 to 18.3 m (30 to 60 feet).

Virginia Tech collaborated with Strongwell, the Virginia Department of Transportation (VDOT), and the Virginia Transportation Research Council (VTRC) to construct a bridge using the 36 inch DWB. The team rehabilitated a short span bridge on Route 601 over Dickey Creek in Smyth County, Virginia with the 36 inch DWB (details in Part 1). In the development phase for the 36 inch DWB, Strongwell first manufactured a 20.3 cm (8 inch) subscale prototype of the DWB. The beam was later implemented in the Tom's Creek Bridge rehabilitation [1].

Following the Tom's Creek Bridge rehabilitation, a number of the 8 inch double-web beams were tested to failure [2]. As tested in three- and four-point bending, the 8 inch DWB consistently failed within the compressive flange at a primary interface between carbon and glass fibers. The failure was considered to be delamination, given the low strains measured on the flange at failure and the consistent location of the separation. Furthermore, the delamination appeared to initiate in the vicinity of the load patches, indicating a stress concentration effect. Schniepp [3] and the author tested nineteen 36 inch DWB's to failure under four-point bending (Figure 2). Again, the failure mechanism appeared to be delamination within the compressive flange (Figure 3), initiating at the load patches. As in the case of the 8 inch DWB, the failure occurs at relatively low in-plane strains, suggesting that the delamination caused premature failure prior to compression failure.

The lay-up of the 36 inch DWB is proprietary, but the flange can be represented as two sub-laminates as shown in Figure 4. The outer sub-laminate essentially consists of alternating layers of unidirectional carbon tows and glass fiber continuous strand mat (CSM), while the inner sub-laminate is formed from half of the web material and is basically a quasi-isotropic lay-up of glass fibers only. Possible delamination initiation sites include the free edge or the inner flange taper at the interface between the two sub-laminates, where the innermost carbon ply is adjacent to a [0/90] glass fabric. The problem of delamination at material and geometric discontinuities such as free edges and tapers is well known.

### **1.1.2 Strength and Life Prediction by Senne**

To develop a strength and life prediction for the 8 inch DWB, Senne [4] developed a simplified stress analysis for composite beams that includes interlaminar stresses at the free edge. This model uses a simple laminated beam theory to determine effective beam stiffness quantities

and then calculates the curvature of the flanges under an applied bending moment. In-plane stresses are determined using CLT, and the DWB is modeled as a rectangular beam by “smearing” the web panel properties. Senne then utilizes a boundary-layer solution developed for laminated plates to determine free-edge stresses in the smeared beam. The two boundary-layer solutions considered include the “Primitive Delamination Model” of Pipes and Pagano [5, 6] and the method by Kassapoglou and Lagace [7-9].

The results of the analysis as applied to the 8 inch DWB suggested that a tensile interlaminar normal stress  $\sigma_z$  at the free edge of the primary glass-carbon interface controls the failure. Following the work of Brewer and Lagace [10], Senne utilized the Quadratic Strength Criterion for delamination to predict failure:

$$\left(\frac{\sigma_{zz}}{S_z}\right)^2 + \left(\frac{\tau_{xz}}{S_{xz}}\right)^2 + \left(\frac{\tau_{yz}}{S_{yz}}\right)^2 = 1 \quad (1-1)$$

An average interlaminar tensile strength  $S_z$  was determined by predicting the critical value of  $\sigma_{zz}$  at failure for each beam tested using both free-edge models above. The back-calculated strength  $S_z$  varied from 0.683 to 2.47 MPa (99 to 358 psi), depending upon the free-edge model and the type of smearing scheme utilized. The interlaminar normal stress  $S_z$  was also measured using a tensile “pull-off” specimen machined from the web-flange interface region of each beam tested. A mean interlaminar tensile strength of  $S_z = 1.14$  MPa (165 psi) was obtained.

Senne developed fatigue life predictions using the initial, back-calculated strength values. The remaining strength approach of Reifsnider et al. [11] was employed (discussed in Section 1.2.6), modeling the boundary layer in the compressive flange as the critical element. Stiffness reduction in the off-axis plies within the tensile flange were accounted for, using stiffness evolution curves taken from coupon fatigue data for glass/vinyl ester composites by Phifer [12]. Senne tested four beams in fatigue. The life predictions are compared with the experimental results in Figure 5. (Note that two different batches of beams were tested, 400- and 500-series. The two batches differed in average ultimate moment to failure and stiffness due to some variation in materials or processing.)

One of the intents of the current study is to improve upon some of the short-comings of the previous approach developed for the 8 inch beam. Notably, it is recognized that failure originates at load patches, suggesting a load concentration effect. This observation suggests using a higher-order model to capture these non-classical effects which are not considered in ordinary beam theory<sup>1</sup>. Therefore, a more robust model for the global analysis is desired. Detailed analyses which can provide accurate interlaminar stresses at material and geometric discontinuities are also required. The smearing approach is used to adapt a free-edge model for laminated plates to thin-walled beams; this violates the stress-free boundary conditions on the inner surface of the flange.

The use of a global-local approach to treat the flange as a plate separately from the global analysis should yield more accurate results. In such a methodology, the far-field stresses might be determined using laminated beam theory (as in Senne's work), and the boundary layer stresses would be determined using a local model. Better estimates of the free edge interlaminar stresses can also be obtained by employing more recently developed boundary layer models, which satisfy more boundary conditions and layer-wise continuity conditions. Ideally, this global-local model would permit a closed-form solution for relatively simple strength predictions, and it would be straightforward to integrate into a life prediction methodology.

A review of the literature will highlight the usual failure mechanisms for FRP structural beams and may provide insight into the nature of the DWB's behavior. Assuming that delamination is in fact the critical failure mode of the DWB, the literature in the area of delamination will be reviewed. Analytical approaches developed for free edge delamination and ply drop-offs on laminates will be reviewed, and studies of larger composite structures will also be considered. The emphasis is on mechanics of materials type approaches, but fracture mechanics or energy based methods will also be reviewed. Specifically, the plausibility of applying a closed-form or explicit approach will be explored. Finally, as the second objective of this study is to predict the fatigue life of the DWB, the remaining strength approach to fatigue life prediction will be reviewed.

---

<sup>1</sup> Consideration of these local effects is important not only for research purposes, but also in designing for real applications. For instance, the abutment support under a bridge girder creates a significant stress concentration (see Section 2.3.4).

## **1.2 Literature Review**

### **1.2.1 Failure Mechanisms in FRP Composite Beams**

A number of researchers have tested FRP structural beams in quasi-static and fatigue loading. In general, several local failure modes can occur when care is taken to avoid lateral-torsional buckling: buckling of the compressive flange [13-18], axial compressive failure of the top flange [14, 16], separation of the flange/web interface [17], delamination within the top flange [14], shear failure [14], and crushing [13, 14]. Local flange buckling appears to be the most common failure mode. Oftentimes, the local buckling is not catastrophic, and ultimate failure does not occur until the post-buckled axial strains exceed the strength of the flange material. In most cases, the ultimate strength is influenced by the stress concentration at the point(s) of loading [14]. Furthermore, failure can also occur at the supports [17].

### **1.2.2 Free Edge Delamination**

A brief overview of free edge problem and analysis methods was given by Senne [4]. More exhaustive reviews can be found in [19, 20]. A brief review of the most pertinent papers is given here. The focus is on stress-based analytical modeling and finite element analysis of the stress state at free edges in thick laminates. Of particular interest are models developed for general laminates under transverse loading.

The earliest work by Pipes and Pagano [5, 21] and others, e.g. [22], demonstrated the free edge effect in which large interlaminar stresses can develop at the free edge of a laminate at the interface between two dissimilar plies. These stresses decay over some distance away from the edge (the “boundary layer”), and if the loading is in-plane, the plane stress state predicted using CLT is recovered. The phenomenon is due to mismatches in Poisson’s ratio and coefficients of mutual influence between adjacent plies. The effect of lay-up and ply properties on the interlaminar stresses was demonstrated by Pagano and Pipes [23] and Rybicki [24]. These works also suggested the existence of a weak singularity in the stresses at the interface between two layers at the free edge. This postulate was later verified by Wang and Crossman [25] using Finite Element Analysis (FEA) and Wang and Choi [26, 27] using an eigenfunction expansion approach.

Kassapoglou and Lagace [7-9] developed an analytical solution using assumed stress shapes of a separable form that are found using the principle of minimum complementary energy. The original formulation was limited to symmetric laminates and in-plane loading, but

the method was later extended to non-symmetric laminates and combined loads [9, 28]. This type of assumed-stress shape energy approach has been tested and modified by a number of researchers, e.g. References [29-31]. The method is efficient for thick laminates, but it does not accurately capture the mismatch in ply properties through the thickness of the laminate. Therefore, the stress-free boundary conditions on the free edge are met only on a point-wise basis, not continuously through the depth.

More recent work has aimed to improve the accuracy of these approaches by using the Kantorovich method with assumed stress functions in the out-of-plane direction and unknown functions in the in-plane direction [32], or by using the Extended Kantorovich method to iteratively converge upon the exact in-plane and out-of-plane functions [33-35]. Despite these recent refinements in the approximate assumed-stress approach, all of these models assume that there are no variations in stress in the primary laminate direction (x-axis). Therefore, local stress concentrations due to loads or supports cannot be captured. Furthermore, transverse shear effects due to applied loads are not considered as the deformation is assumed to be simple bending.

To overcome this limitation, Kim and Atluri [36] derived an assumed-stress solution, which includes the longitudinal degrees of freedom in the stress distributions to address the case of transverse shear loading. The development is similar to that of Kassapoglou and Lagace, but the existence of a gradient in the axial direction complicates the analysis considerably. All boundary conditions and compatibility conditions are satisfied. Cross-ply and angle-ply laminates were considered, and the results suggest that the relative amount of shear to bending changes the shapes and magnitudes of the interlaminar stress distributions. The shapes of the interlaminar stresses under transverse loading were found to be similar to those due to axial loading or pure bending, but the magnitude of the normal and shear stresses were very high, since the transverse loading directly subjects the laminate to interlaminar stresses. The theory is applicable to general laminates, although no results were given for unsymmetric laminates in [36]. Furthermore, verification with other models or FEA was not presented.

Rose and Herakovich [37] generalized the approach of Kassapoglou and Lagace to account for mismatches in Poisson's ratio and coefficients of mutual influence at adjacent plies by including additional terms in the assumed stress expressions. These terms were chosen to have self-equilibrating forms so as not to violate the global equilibrium. Axial loading and

bending only were considered, but the results were greatly improved over those of Kassapoglou and Lagace in comparison to finite element results. Kim and Atluri [38] extended the approach of Rose and Herakovich to combined thermo-mechanical loading. Axial loading and bending with the addition of an arbitrary through-the-thickness temperature distribution was considered, and the authors observed good correlation with Wang and Crossman's FEA results [25].

#### **1.2.2.1 Strength Criteria**

Assuming that the free edge stresses can be calculated accurately, the next step is to properly apply these stresses in an appropriate failure criterion. Kim and Soni [39] utilized a maximum stress type criterion, assuming that the normal stress controls failure. They compared using a point stress value at the free edge with using an average stress in the criterion. The average stress was obtained by averaging over some characteristic length. This approach was first introduced by Whitney and Nuismer [40] for the case of a notched laminate, to avoid errors in the peak stress caused by the existence of a singularity. In Kim and Soni's work, the characteristic length was arbitrarily defined as the ply thickness. Kim and Soni [41] later suggested a failure function containing quadratic terms on both the normal and shear stresses, as well as a linear term on the normal stress, suggesting that a compressive normal stress may suppress delamination.

Brewer and Lagace [10] proposed a purely quadratic strength criterion with no linear terms, Equation (1-1). The criterion did include a quadratic term on compressive normal stresses, but this was later omitted due to a lack of evidence to suggest that compressive normal stresses could initiate delamination. The characteristic averaging length was determined experimentally and was found to depend upon the material properties. The characteristic length was found to be on the order of a ply thickness, but not equal to it. However, the averaging length may be much longer, depending upon the stress shapes. The early work of Pipes and Pagano [21, 42] suggested that the length of the boundary layer may actually be on the order of the laminate's thickness, and this concept has been adopted throughout the literature.

#### **1.2.2.2 Interlaminar strength test methods**

Based on a tensile pull-off test method first introduced by Mandell et al. [43], Lagace and Weems [44] modified the method using a tapered cross-section to measure the normal interlaminar tensile strength of various graphite- and glass-epoxy laminates at specific interfaces. Their results were independent of the lay-up suggesting that the strength is independent of the

properties of the neighboring plies. Senne [4] utilized a similar test to measure the normal tensile strength at the primary carbon/glass interface of the 8 inch DWB flange.

Interlaminar shear strength is typically measured using the ASTM standard methods for the short beam shear test [45] or the V-notch/Iosipescu shear test [46]. These methods must be carefully applied to avoid failure at the loading points and the results must be properly interpreted, due to the localized effects discussed in Part 1 and the sensitivity of the apparent strength to the layup.

### **1.2.3 Delamination at Ply Drop-Offs or Laminate Tapers**

A recent review of analytical and numerical modeling of ply drop-offs and tapered laminates was given by He et al. [47]. A review of some of the more pertinent papers dealing with external ply drop-offs or tapers is given here.

Hoa et al. [48] performed FEA of an internal drop-off in a unidirectional glass/epoxy composite, including the fillet. They determined that the critical stresses were the interlaminar normal and shear stresses and that the peak stresses occur in the corner region. Wu and Webber [49] developed a quasi-3-D FE model of angle-ply laminates with a single step (external) drop-off, assuming that the stresses and strains were independent of the axial coordinate. Their results suggested the presence of a singularity at the corners of the dropped plies. They also observed that the use of a matrix fillet at ends of the taper reduces the stresses significantly. Her [50] developed a finite element model for an internal ply drop-off that represented the enclosed wedge region as a three materials junction. An eigen-function method was utilized to assess the singularities at the corners of the wedge. Daoust and Hoa [51] used FEA to investigate various parameters influencing the interlaminar stresses, including internal versus external drop-offs, fiber orientation, geometry of the drop-off, and the presence of fillets. In particular, their results suggest that internal drop-offs are twice as strong as external drop-offs.

Analytical methods to predict failure at drop-offs are scarce. Thomsen et al. [52] considered soft-core sandwich panels with tapered face laminates (external drop-offs) under axial compression. They modeled the core as a 2-parameter Winkler elastic foundation, neglecting the interaction between the face laminates, and later provided experimental verification of the approach in Reference [53]. Failure of the tapered face sheets was attributed to local bending at the edge of the ply drop-off.

In all of the above studies, the drop-offs were oriented transverse to the direction of the applied load, which was uniaxial stress or extension in all cases. The case of a longitudinal ply taper in which the discontinuity runs parallel to the loading has received much less attention. Most notably, Vizzini [54, 55] has utilized FEA to study laminated composites with internal drop-offs.

#### 1.2.4 The Fracture Mechanics Approach to Delamination

Stress-based criteria for delamination initiation require accurate stress calculations and interlaminar strength measurements, both of which can be difficult. An alternate approach to strength prediction is to use fracture mechanics concepts in which the nature of the stress field around an existing crack tip is considered. The energy to grow the crack can be related to the fracture toughness, a material property, or the strain energy release rate (SERR), a property of both the material and laminate construction. The SERR concept is especially useful for characterizing the tendency for delamination in general composite laminates or laminated structures.

The SERR is derived from an energy balance which equates the energy required to grow a crack to the change in potential energy of a volume of material caused by the crack growth. Specifically, the strain energy release per unit area of crack extension,  $G$ , is

$$G\delta A = \delta W - \delta V \quad (1-2)$$

where  $\delta A$  is the change in crack area,  $\delta W$  is the work done by an external force, and  $\delta V$  is the change in potential energy. Substituting expressions for  $\delta W$  and  $\delta V$  for a particular type loading, one finds that the SERR is proportional to the change in stiffness of the laminate or structure. Therefore, any analytical solution which can accurately predict the structural stiffness as a function of the crack size will yield the SERR. Failure occurs when the SERR reaches some critical value,  $G_c$ .

Crack growth may occur by way of three different modes of deformation: mode I, caused by normal stresses, and modes II and III, caused by shearing stresses. The SERR for a given loading may be comprised of all three modes, although typically mode I dominates. Thus, an appropriate failure criterion may include all three modes of deformation. Reeder [56] and Miraevete [57] discussed several empirical expressions for mode-mixity. Critical SERR's may

be obtained by coupon tests designed to promote delamination growth under static loading. For instance, the mode I critical SERR,  $G_{IC}$ , can be measured using the standardized Double Cantilever Beam (DCB) test [58]. Various other test methods have been proposed to introduce mode mixity that would allow the investigator to determine the mode II contribution to  $G_c$ , including the mixed-mode bending (MMB) and the end notched flexure (ENF) tests (reviewed in Reference [59]).

O'Brien [60, 61] was one of the first to successfully apply the fracture mechanics concepts to composite materials. O'Brien used classical laminate theory and a rule-of-mixtures approach to calculate the change in laminate stiffness due to crack growth. He then derived the SERR in terms of the change in laminate stiffness and the applied strain.  $G_c$  for a given material could be calculated using measured strain to failure data from quasi-static coupon tests. O'Brien observed that the SERR is independent of crack length, except for the initial crack growth in a very small region at the free edge of a laminate, in which case the SERR undergoes a rapid increase. Therefore, he reasoned that any small delamination that formed at the edge would undergo rapid initial growth. Assuming that there are always pre-existing flaws in the material, the SERR crack growth concepts can therefore also be applied to initiation. O'Brien demonstrated his approach on tensile-loaded laminates by relating the SERR to the applied strain. The approach has since been validated extensively, but it is limited to simple geometries and loading. Furthermore, the method cannot distinguish the separate mode contributions.

Application of the SERR concepts to composite structures is usually accomplished using FEA. In a finite element model, a crack can be introduced rather easily, and the change in structural stiffness can be evaluated by considering the structure's response to a given loading. A number of techniques have been devised to calculate the SERR, but the most popular to date is the Virtual Crack Closure Technique (VCCT). The VCCT was originally introduced by Rybicki and Kanninen [62] and later proved rigorously by Raju [63]. Details of its application are given in References [57, 64, 65]. The VCCT is based on Irwin's crack closure integral, which hypothesizes that the amount of energy released during crack extension is the same as the amount of work required to close the crack. Essentially, the SERR is equal to the work done by the nodal forces to displace the nodes at the crack tip. Furthermore, the individual mode contributions to the SERR can be calculated separately if a 2-D or 3-D FEA is performed. Finally, if the mesh is sufficiently refined, then "the stress field behind the crack tip can be

approximated with the stress field ahead of the crack tip.” [57] Thus, the FE model only has to be solved once for one crack length.

### **1.2.5 Delamination in Composite Structures**

The study of delamination in more complex laminated composite structures typically requires use of FE methods such as the VCCT. One of the most widely studied problems is the skin-stiffener debonding which may occur in aircraft structures under internal pressure or post-buckling loads. A number of researchers including [66, 67] have investigated the problem using the VCCT approach. Because the mesh refinement required at the crack tip to provide accurate SERR calculations can become prohibitive, the “shell/3D” modeling technique has been used to reduce the number of degrees of freedom [68]. In this method, the elements in the vicinity of the crack tip are modeled using 3-D solid elements to provide accurate interlaminar stresses and therefore SERR components. Elements in the far field are modeled using shell elements, and continuity of the displacements at the interface between the shell and solid elements is enforced using constraint equations or other methods.

### **1.2.6 Fatigue Life Prediction of Composite Structures**

Predictions developed for fatigue durability in the literature are most commonly based on residual strength degradation, although some are based on modulus degradation or damage tolerance approaches [69]. In the residual strength approaches, fatigue failure is assumed to occur when the residual or remaining strength is equal to the applied stress. In particular, Reifsnider and Stinchcomb [70] postulated that remaining strength can be used as a measure of the damage and that remaining strength is an internal state variable. The remaining strength will depend upon the load level and number of fatigue cycles (or time). In general, the reduction in strength can be non-linear, so that the sequence of damage events can affect the length of life. The ability of this approach to capture such path-dependence is a distinct advantage over linear type models such as Miner’s rule for metals.

In Reifsnider’s approach, the remaining strength of a “critical element” governs the life of the entire structure. Examples of critical elements include the  $0^\circ$  plies in a  $[0/90]$  laminate loaded axially or the boundary layer in a delamination problem. The remainder of the material, e.g. the  $90^\circ$  plies, comprises the “sub-critical elements”. Degradation and eventual failure of the sub-critical elements serves only to redistribute the stress to the critical elements, eventually causing ultimate failure of the structure. Thus, the keys to the critical element approach are to

identify the critical element(s), to determine the fatigue performance of the critical elements, and to identify and quantify the damage mechanisms and their kinetics in the sub-critical elements. Appropriate failure functions must be selected to model the sub-critical damage mechanisms and to calculate the remaining strength in the critical element(s).

Using a non-linear kinetic/rate equation to describe the damage processes, Reifsnider and his coworkers derived a strength evolution integral which has been tested extensively for a variety of problems and materials. This equation has the form

$$Fr = 1 - \int_0^{\tau} (1 - Fa)j\tau^{j-1}d\tau \quad (1-3)$$

where  $Fr$  is the normalized remaining strength,  $Fa$  is the applied stress (or more generally, the failure function such as maximum stress, Tsai-Hill, etc.),  $\tau$  is a characteristic time which describes the damage process, and  $j$  is considered to be a material constant. Thus, the equation can be applied to creep or other time-dependent processes. For the case of fatigue,  $\tau = n/N$ , where  $n$  is the number of fatigue cycles and  $N$  is the number of cycles to failure for the given  $Fa$ . If  $Fa$  is constant, Equation (1-3) becomes

$$Fr = 1 - (1 - Fa)\tau^j \quad (1-4)$$

Note that as damage occurs in the sub-critical elements, the stress level in the critical element increases, and  $Fa$  increases with time or cycles.

To apply the strength evolution integral to predict fatigue life, the following information is required: 1) the fatigue S-N curve for the critical element, 2) the stiffness changes in the sub-critical elements with cycles, and 3) the value of the  $j$  parameter. Items (1) and (2) are typically found by performing coupon fatigue testing. The value of  $j$  is found empirically, and a value between 1 and 1.2 has been found to work well for most composite materials in which the remaining strength decreases at an increasing rate [11].

### 1.3 Summary

This review of the scientific literature suggests that local compression buckling controls failure for most FRP structural beams. Delamination within the flange is rare, but given the thickness of the DWB flange and its hybrid carbon/glass design, delamination is possible. In all cases, the importance of the stress concentration at the loading points is recognized. The free edge delamination problem is well understood, and analytical models are available for laminates which provide sufficient accuracy for most applications. However, the models developed for transverse loading of thick laminates are not as well developed and do not provide high degrees of accuracy. Furthermore, failure predictions for composite structures such as beams and stiffened panels rely primarily on finite element analysis coupled with fracture mechanics concepts to predict delamination onset and growth. The problem of delamination at a ply drop-off or taper is not as well understood as the free edge problem. Most work in this field has focused on axial loading of simple laminates with the taper aligned parallel to the loading direction. Furthermore, little attention has been given to the problem of a taper with external ply drops such as that in the 36 inch DWB. The complexity of the current problem therefore suggests the use of finite element analysis in either a stress based or fracture mechanics based approach.

### 1.4 Objectives

The first objective of this study is to predict the static strength of the 36 inch DWB. The first step is to identify the failure mode, based on the experience with the 8 inch section, failure of the 36 inch DWB is hypothesized to occur by delamination at either the free edge or the inner flange taper. The possibility of compression failure of the carbon fiber plies will also be investigated. Post-failure inspection of the beams coupled with a detailed finite element analysis will be required to identify the failure mode and location. Depending upon which failure mode is found to control the strength of the DWB, the use of analytical models may or may not be possible.

Having determined the failure mode and developed means to predict the strength, the second objective of this study is to predict the fatigue life of the DWB as tested under transverse loading. The stress analysis will be incorporated into a life prediction code using the critical element approach. Stiffness reductions in off-axis plies will be modeled using empirical data from coupon studies. The remaining strength of the carbon plies will be tracked using fatigue-

life curves obtained from coupon testing. The remaining strengths of the delamination sites may also be monitored. A fatigue-life curve will then be constructed for the DWB under transverse loading and compared to experimental data for full-scale fatigue tests.

## 2 Strength Prediction: Methods

The first step in developing a strength prediction is to identify the failure mode. Observations from the static failure tests by Schniepp [3], post-failure inspection of the beams, and finite element analysis were used to attempt to identify the controlling failure mechanism for the 36 inch DWB. The plausibility of compression failure was investigated using a 3-D global FE model of the DWB. Results from this model were then compared to experimental strain measurements and laminated beam theory results. To also investigate the possibility of a delamination failure, a finite element global-local solution was developed using a successive sub-model approach. The free edge and flange taper regions near the load patch were considered as potential “critical elements”. The use of local sub-models allows a more detailed representation of the regions, which is especially necessary when calculating interlaminar stresses.

In the local analysis, individual plies were modeled using 3-D solid elements, and the mesh was refined significantly to capture gradients at the material and geometric discontinuities. In light of Senne’s work [4], the critical stresses were expected to be the interlaminar normal stress,  $\sigma_z$ , and the interlaminar shear stress,  $\tau_{xz}$  where the  $x$ -axis is along the beam’s length, the  $y$ -axis is across the width of the beam, and the  $z$ -axis is through the depth of the beam, in the direction of loading.

Initially, the 11.9 m (39 ft) four-point test geometry was studied, but the analysis was then extended to the other spans to assess the effect of span on the strength. Three-point and uniform loading cases were also considered. Furthermore, the influence of the loading pad on the local stresses was investigated. Finally, the residual thermal stresses due to cool down from cure were estimated, and the influence of these residual stresses on the strength predictions was examined.

### 2.1 Failure Tests

Schniepp [3] and the author tested 19 beams to failure in four-point bending using loads at the third points applied via static hydraulic actuators (Figure 2). In light of previous testing of the 8 inch DWB which suggested a span dependence of the ultimate strength, tests were conducted on the 36 inch beam at spans of 5.49, 9.14, 11.9, and 17.7 m (18, 30, 39, and 58 ft). The test set-up included two actuators located at roughly third points with 23 cm (9 inch) long

steel-reinforced elastomeric bearing pads at both the supports and at the loading points (Figure 2) to reduce the severity of the load concentrations. The set-up was nearly identical to that used in the stiffness measurement experiments, detailed in Part 1. Strain measurements were taken at mid-span to track axial/bending strains, and loads and deflections were also recorded. In an effort to track the origin and direction of the crack growth along the length of the top flange, crack gages were bonded along the free edge of the top flange for four beams as shown in Figure 6.

Because the failures in both the 8 inch and 36 inch DWB initiate near the loading patches, it follows that the concentrated loading has a localized effect on the critical stresses. This stress concentration may be caused by several factors including shear warping and transverse compressibility, as discussed in Part 1. Although these are mainly web effects, they will generate additional local bending curvatures in the flanges and will cause a stress concentration. In order to quantify shear warping behavior, Schniepp [3] measured web shear strains in the vicinity of the load patches and the supports. Strain measurements in the transverse direction were also taken under and near one load patch during a 12 m (39 ft) span test to assess transverse flexibility (Part 1). Axial gages were placed on the top flange surface near the load patches in a few tests to measure any change in strain resulting from the local deformation. These measurements were compared to the mid-span measurements and the results from the FE model.

Following completion of the failure tests, the beams were inspected for damage patterns. Several beams were sectioned using a circular saw to observe the nature of the failure. To identify the possible delamination initiation site(s), cuts were made at the visible end of the crack on the free edge, and sections of the top flange were removed.

## **2.2 Stress Analysis using the Finite Element Method**

### **2.2.1 Global Model**

Half-beam models of the DWB under four-point loading geometry for spans of 9.14, 11.9, and 17.7 m (18, 30, 39, and 58 ft) were constructed in ANSYS<sup>®</sup>, employing symmetry conditions at mid-span to reduce the number of elements (Figure 7). The end constraints were modeled by simply specifying zero displacement at the end nodes on the bottom edge of the beam, since the stresses at the end supports are not important for these spans. All other details, including the representation of the pad/plate assembly, were identical to those of the full-span

models detailed in Part 1. Again, the 3-D 8-noded layered brick SOLID46 elements were used to model the walls of the beam. The beam was meshed with 7.6 cm (3 inch) long elements in the  $x$ -direction, but in the region under the pad and one pad width on either side of the pad, the mesh was refined further (0.5 to 1 inch long elements) to properly capture stress gradients. The model was solved for two values of the change in temperature following cool-down from cure:  $\Delta T = 0$  and  $\Delta T = 24\text{ }^{\circ}\text{C} - 138\text{ }^{\circ}\text{C} = -114\text{ }^{\circ}\text{C}$  ( $75\text{ }^{\circ}\text{F} - 280\text{ }^{\circ}\text{F} = -205\text{ }^{\circ}\text{F}$ ). The first case neglects residual thermal stresses, and the second case models full thermal effects, assuming a cure temperature of  $138\text{ }^{\circ}\text{C}$  ( $280\text{ }^{\circ}\text{F}$ ) and a lab test temperature of  $24\text{ }^{\circ}\text{C}$  ( $75\text{ }^{\circ}\text{F}$ ). Layer-wise stresses were obtained for the select SOLID46 elements shown in Figure 8 using the key option,  $\text{KEYOPT}(8) = 1$ <sup>2</sup>.

The deflection at mid-span on the bottom flange was checked for agreement with the experimental values and MLB model predictions<sup>3</sup>. The predicted in-plane stresses and strains through the depth of the flange at mid-span were also compared with the MLB prediction, assuming no residual stresses due to processing, i.e.  $\Delta T = 0$ . Particular attention was paid to in-plane strains in the vicinity of the load patch. Axial strains on the top flange and transverse strains on the web underneath the load patch were compared with experimental measurements. To assess the effectiveness of the load pad representation in the FE model, pressure-sensitive film (Pressurex<sup>®</sup>) was used to qualitatively characterize the normal stress distribution under the loading pad. The resulting stress profile was then compared to the FE predicted pressure distribution (the normal stress  $\sigma_z$  from the top surface nodes).

### 2.2.2 Free Edge Submodels

Using the sub-modeling feature in ANSYS<sup>®</sup>, a sub-model at the free edge was developed (Figure 9). The free edge was idealized with perfectly flat and uniform plies. This is a significant oversimplification of the actual beam cross-section shown in Figure 10 which shows significant ply waviness and variability in the vicinity of the free edge. The plies appear to be “bunched” together on both sides causing plies to fold upward. The effect is usually more pronounced on one side than the other, due to the fact that the DWB is pultruded on its side. The weight of the material causes the material to sag, resulting in more “bunching” on one side of the flange. The validity of the sub-model idealization is dubious, given the sensitivity of the free

---

<sup>2</sup> Setting  $\text{KEYOPT}(8) = 1$  causes results for all layers in a SOLID46 layered element to be stored.

<sup>3</sup> For comparison with beam theory, the 39 ft full-span model with nodal fixity boundary conditions at the neutral axis from Part 1 was actually used to check stresses and strains.

edge stress state to lay-up. Nevertheless, identifying and modeling a more realistic lay-up/construction that is common to all manufactured beams would be extremely difficult. Furthermore, the nature of the free edge is likely to vary across different production runs. The idealized model provides a simplified means to predict strength and investigate the sensitivity of the interlaminar stresses to loading conditions and beam construction.

The procedure actually consisted of two sub-modeling steps. In the first step, a 22.9 cm long by 6.35 cm wide (9 inches by 2.5 inches) section of the top flange centered at the edge of the pad ( $x = 423$  cm or 166.5 inches for the 39 ft case) was modeled (EDGESUB1 in Figure 9). Thus, half the sub-model is under half of the load patch, and half is outside the patch. The pad and plate volumes and the applied pressure on the steel plate were included. EDGESUB1 was meshed using the SOLID46 3-D element, but each ply was modeled as a single layer of elements. The decision to model each layer individually was based on a refinement study conducted during the analysis of the short beam shear specimen which was used to measure the interlaminar shear stress (see Section 2.3.2.1). Note that the use of even greater mesh refinement such as multiple elements per ply has been recommended by a number of researchers to obtain accurate interlaminar stresses. However, such refinement is difficult to obtain for such a thick laminate as the DWB flange. Furthermore, the stress averaging technique eliminates the need for highly accurate estimates of the free edge singularities.

EDGESUB1 was also meshed to provide additional refinement over the global model in the other two coordinate axes. Element dimensions were 1.27 cm (0.5 inch) in the  $x$ -direction and 0.254 cm (0.1 inch) in the  $y$ -direction. Following the sub-modeling approach in ANSYS<sup>®</sup>, the nodes on the “cut” boundaries of EDGESUB1 were isolated and saved to a file. Returning to the solved global model, the degree of freedom (displacement) results were interpolated to cut boundary nodes. Finally, back in the sub-model, the boundary displacement values were imported as boundary conditions, and the sub-model was solved.

In order to provide additional refinement at the free edge, where gradients in stress are known to be very large, a second sub-model, EDGESUB2 (not shown), was constructed. This sub-model was a 2.54 cm long by 2.54 cm wide by 2.62 cm thick (1 inch x 1 inch x 1.032 inch) volume to be centered along the free edge at the location of interest between  $x = 411$  and 434 cm (162 and 171 inches), the region modeled using EDGESUB1. Each ply was modeled using individual SOLID191 elements, the quadratic version of the SOLID46 element to obtain more

accuracy with the same number of elements. The mesh was refined in the  $x$ -direction so that element lengths were 5.08 mm (0.2 inch). In addition, the mesh in the  $y$ -direction was refined so that the element width in the outer 2.54 mm (0.1 inch) wide portion of the free edge was 0.254 mm (0.01 inch); this dimension is slightly less than the thickness of the thinnest ply. The cut boundary nodal interpolation procedure above was repeated, using the results of EDGESUB1 as the input for EDGESUB2. Results were obtained at locations under and just outside the load patch:  $x = 414, 419, 422, 424, 427, \text{ and } 429$  cm (163, 165, 166, 167, 168, and 169 inches)<sup>4</sup>. (Note that for the  $x = 414$  cm location, a modified intermediate sub-model was created to cover the entire length of the pad; this was necessary to avoid local stress concentrations associated with the applied displacement boundary conditions on the cut boundaries. Finally, the complete procedure was repeated for the mid-span location by excluding the pad and plate volumes.)

For each location, average element results for the  $\sigma_z$  and  $\tau_{xz}$  were output for the column of free edge elements in the center of the sub-model. The stress profiles across the width of the boundary layer at several ply interfaces, including that of the primary carbon/glass interface, were also obtained. To assess the influence of thermal residual stresses and to estimate the failure load, the thermal and mechanical loadings were simulated separately. The thermal only loading was modeled by applying the change in temperature  $\Delta T = -205$  °F (-114 °C) and a very small load (0.0445 N or 0.01 lb) to the load patch. The mechanical loading was modeled by applying the full 445 kN (100 kips) per patch and setting  $\Delta T = 0$ . The two effects were then combined using superposition, and the failure load was determined by calculating width-averaged stresses and then scaling the mechanical stresses to obtain a maximum failure function  $Fa = 1$ .

### 2.2.3 Flange Taper Submodels

To model the flange taper region, a similar successive sub-modeling approach was used. The global model used above was modified to include the taper and the flange-web fillet (Figure 11). The taper and fillet regions were modeled as isotropic materials using the effective properties of the web laminate and the flange sub-laminate 2. Furthermore, the fillet was approximated as a wedge shaped volume. These approximations were made to aid the meshing process – the use of effective properties was not expected to introduce significant error as the

---

<sup>4</sup> Recall that the center of the load patch is at  $x = 411$  cm (162 inches) and the inner edge of the pad is at  $x = 423$  cm (166.5 inches).

global model is simply being used to calculate nodal displacements for use as boundary conditions in the first sub-modeling step.

The first sub-model (TAPERSUB1) for the taper analysis included a 23 cm (9 inch) long portion of half the flange width (Figure 12). As in the free edge case, this first sub-model was constructed primarily to capture gradients in the  $x$ -direction. Again, each layer was modeled with separate elements. The hexahedral element lengths in the  $x$ -direction were 5.72 mm (0.225 inch), and the widths in the  $y$ -direction varied between 1.51 and 1.75 cm (0.596 and 0.688 inch). Half of the pad was included to capture the stress concentration at the inside edge (nearest mid-span) of the pad. Furthermore, the round fillets were modeled using the exact geometry, but again the fillet material was modeled as isotropic.

The nodal results from TAPERSUB1 were then applied as boundary conditions to a subsequent sub-model, TAPERSUB2, shown in Figure 13. TAPERSUB2 can be positioned anywhere along the length of TAPERSUB1 to capture the through-the-thickness profile of the interlaminar stresses. However, based upon the experience with the free edge analysis, the TAPERSUB1 taper results were used to identify the location of maximum interlaminar normal stress,  $\sigma_z$ . TAPERSUB2 was positioned at this critical location, as well as at mid-span.

In TAPERSUB2, the taper region was modeled with plies terminating in a step-wise fashion. The element dimensions were 2.54 mm (0.1 inch) in the  $x$ -direction, and between 0.734 and 4.70 mm (0.0289 and 0.185 inch) in the  $y$ -direction. The smooth taper was accomplished by adding a wedge-shaped resin-only region, as shown in Figure 14. This is the approach taken by other researchers [48, 51]. As observed by Her [50], this representation results in singularities at both the tip and the interior corner of the wedge. An examination of the  $y$ -direction stress profiles later revealed that the TAPERSUB2 mesh possessed insufficient refinement at the taper end to adequately capture the behavior near these singularities. Therefore, a third and final submodel (TAPERSUB3) was created to provide additional  $y$ -direction mesh refinement at this location (Figure 15).

The TAPERSUB3 sub-model was only 2.54 mm (0.1 inch) long in the  $x$ -direction and 3.18 cm (1.25 inch) wide in the  $y$ -direction. Again, each layer was modeled with a separate element, except for the two plies composing the primary carbon/glass interface (at the boundary between the two flange sub-laminates). In these two plies, four elements (around 0.102 mm or 0.004 inch thick) through the thickness were used to ensure sufficient refinement of the interlaminar

stresses. The length was meshed with 0.635 mm (0.025 inch) long elements with widths ranging from 0.584 to 0.635 mm (0.023 to 0.025 inch) in the constant thickness portions of the flange. In the taper region, the element widths varied depending upon the ply thicknesses (around 0.762 mm or 0.03 inch).

Using the TAPERSUB3 results, the  $y$ -direction stress distributions were then examined to calculate width-averaged interlaminar stresses at several key interfaces, including the primary carbon/glass interface between sub-laminates 1 and 2. Following the procedure used in the free edge analysis, the averaging length was taken as the tip of the taper and the location where the normal stress switched sign. A volume averaging method was also explored as discussed later in Section 2.3.2.2.

#### **2.2.4 Detailed Flange/Web Junction Model**

The results of the taper sub-modeling analysis (to be discussed in Section 2.2.3) indicate very high tensile stresses at the flange/web junction away from the load patch. However, the accuracy of these predictions is questionable given the manner in which the junction was modeled. Recall that the connection of the flange and web was simply modeled as a T-joint with orthotropic fillet material (Figure 13). In reality, the web material folds around the corner to form the fillet and the resulting gap space at the junction is filled with glass roving (Figure 10). To more accurately model this construction, TAPERSUB3 was modified as shown in Figure 16. The folded web material was modeled as a homogeneous orthotropic material using the effective properties of the web. The gap space was modeled as an orthotropic material with the properties of the glass roving. While still fairly crude, this representation should reduce the stress concentrations induced by the corners in the original model.

### **2.3 Strength Prediction**

#### **2.3.1 Compression Failure**

A stress-based approach was followed to predict failure of the 36 inch DWB under static loading. First, the axial compressive stresses in the top flange were checked for possible failure using the maximum stress criterion. Compressive strength data for the carbon/vinyl ester plies were obtained by testing 26 specimens machined from the outer flange sublaminate, which is composed of carbon fiber and CSM. The Wyoming End-Loaded Side Supported (ELSS) test method [71] was chosen due to its relative ease of use. The specimen dimensions were 12.7 mm wide x 3.18 mm thick x 143 mm long (0.5 inch x 0.125 inch x 5.625 inch). The width and

thickness dimensions are standard, and the length was chosen to permit the maximum gage section possible without encountering buckling failure (determined using the buckling analysis in [72]). Classical laminate theory was then used to back calculate the carbon ply stresses at the failure load of each specimen. The mean compressive strength was obtained using Weibull statistics [73]

To check for compression failure in the DWB, the maximum stress failure criterion was applied to the outer carbon fiber ply in the top flange (where the bending stresses are greatest). The stresses along the length of the beam were determined from the appropriate global model for each test geometry considered. Again, the mechanical and thermal analyses were conducted separately and the results were superimposed. The failure loads were predicted by scaling the mechanical stresses and determining the load at which  $Fa = 1$ .

For verification purposes, Hashin's failure criterion for compressive failure in the fiber mode accounting for shear instability [74] was also applied to the FE results. The criterion has a quadratic form:

$$\left( \frac{\sigma_{11}}{X_{11}^c} \right)^2 + \left( \frac{\sigma_{12}}{X_{12}^s} \right)^2 = 1 \quad (2-1)$$

The in-plane shear strength  $X_{12}$  was taken from Phifer's data [12].

### 2.3.2 Delamination Failure

Next, the possibility of delamination at the free edge or taper region was investigated. Due to the sudden, catastrophic failure mechanism observed experimentally, ultimate failure for this failure mode will be defined as the onset of delamination. The Quadratic Strength Criterion (Equation 1-1) was utilized to predict the onset of delamination. The interlaminar stresses at the free edge were averaged over a characteristic length to be determined. Interlaminar strength values were obtained experimentally as described in the next section. As in the case of compression, the interlaminar stress profiles were obtained for thermal and mechanical loading separately and then superimposed. The predicted failure loads were obtained by scaling the mechanical loads until the Quadratic Strength Criterion was satisfied.

### 2.3.2.1 Interlaminar strength values

Williams et al. [75] measured the interlaminar tensile strength  $S_z$  of the flange using a tensile pull-off test method. Specimens measuring 2.54 cm (1 inch) in diameter were drilled from the flange of one DWB at locations away from the free edge, the taper region, and the flange-web interface to minimize the degree of ply waviness and “bunching”. The specimens were then bonded to aluminum posts, as shown in Figure 17. The specimens were tested in quasi-static tension in displacement control at a loading rate of 2.54 mm/min (0.1 inch/min) until failure, as detected by a loss in the applied load. The location through the thickness of the fracture and the peak load were recorded. The peak load was converted to an average stress using the total cross-sectional area of the specimen. A total of 20 specimens were tested.

To estimate the interlaminar shear strength  $S_{xz}$  of the flange material, thirty-seven 15.2 cm x 2.54 cm x 2.62 cm (6 inch x 1 inch x 1.032 inch) specimens cut from the same areas as the tensile specimens were tested using the short beam shear (SBS) three-point bending test [45]. The SBS test does not promote a pure state of shear due to the presence of bending [76], as well as stress concentrations at the load point and supports. Therefore, the SBS test is traditionally used only for qualitative comparisons of the apparent shear strength between different materials. The unsymmetric layup of the DWB flange also complicates matters, making it impossible to calculate the interlaminar stresses at failure without the use of FEA. Based on the results of this investigation, the full 57 sub-laminate model was utilized for the shear strength estimates.

Thus, a finite element model of a 15.2 cm (6 inch) long coupon specimen cut from the flange under three-point bending was constructed. The model, as shown in Figure 18, was meshed using the SOLID46 element. Initially, the flange was modeled by grouping the plies into sub-laminates which were each modeled using a single SOLID46 layered element. To investigate the effect of sub-laminate size on the convergence of the solution, the flange was modeled using 2, 4, 6, 12, 26, and 57 sub-laminates. The mesh was refined across the beam width and length to permit convergence of the far field stress values (away from load points, supports, and free edges). The load was modeled as a simple line load across the width of the specimen, and the supports were modeled by specifying zero nodal displacements on the bottom surface.

In order to estimate the interlaminar shear strength for each specimen, the failure location through the thickness and the failure load were recorded. The FE results were then scaled

according to the failure load, and the predicted shear stress at the failure location was output. This stress was assumed to be equal to the shear strength of the material (assuming that the failures occurred in the constant shear region). All failures within the carbon/CSM region were included in the analysis to calculate the average interlaminar shear strength of the carbon/vinyl ester plies. The testing and analysis was repeated for 16 specimens cut from the web panels of the DWB to estimate the interlaminar shear strength of a glass/vinyl ester ply. Additional details of the testing and analysis can be found in Williams et al. [75].

### **2.3.2.2 Ply Width and Volume Averaging of Interlaminar Stresses**

Following the average stress approach of Whitney and Nuismer [40] and Kim and Soni [39], the interlaminar stresses at the free edge were averaged over a characteristic length across the width of the flange. This length was taken as the length over which the normal stress remains tensile, e.g. from the free edge to the point that the normal stresses changes sign. The average value was determined by integrating the stresses over the characteristic length using the Trapezoidal Rule and then dividing by the characteristic length. The average stresses due to mechanical and thermal loading were superimposed, and the mechanical contribution was scaled to obtain the predicted failure load at  $Fa = 1$ .

A similar procedure was followed to assess failure at the taper location. However, due to the strength of the taper wedge singularities, the stress concentrations were observed to decay over a much larger distance than the free edge singularity. In the free edge problem, the free edge stresses can quickly change magnitude and sign through the thickness of the laminate as the ply properties or orientations change. In the drop-off problem, all of the surrounding plies above and below the geometric discontinuity experience high stress levels. Therefore, the concept of volume averaging was utilized as an alternate means of predicting the strength. This concept also captures the well-known observation that delamination strength is dependent upon the laminate thickness [77], i.e. delamination resistance is volume-dependent.

A routine was written to output element (average) stresses from all carbon ply elements within a certain radial distance of the taper end. To volume average the stresses, the stresses from each element were inserted into the Quadratic Strength Criterion to calculate the element failure function  $Fa$ . The product of  $Fa$  and the element volume for each element were then summed, and the average  $Fa$  value was obtained by simply dividing by the total volume of the elements. This procedure was applied for each test geometry to predict the ultimate failure load.

(The use of the term “volume averaging” here is somewhat misleading as the procedure technically averages over only a circular area since the volume considered is only one element in length.)

### **2.3.3 Effect of Geometry and Span Dependence**

Schniepp’s experimental results suggest a span dependence for the moment capacity of the DWB. In an effort to reproduce this observation analytically, a failure envelope was constructed for the four-point geometry using the strength predictions for each failure mode. Curves for each failure mode were constructed by predicting the failure load (or moment) at each span. This envelope was then compared to the experimental data to further elucidate the actual failure mode.

### **2.3.4 Uniform Loading**

Although the experimental test procedure dictates that concentrated loads be taken into account, the loading will likely be much less concentrated in real applications. In fact, the critical locations may become the supports, which act as concentrated loads. To assess the likelihood of the DWB failing at a support under less concentrated loading, finite element models were constructed for the case of a uniform distributed load. The pad support was modeled in a manner identical to that of the load patches. The uniform load was represented as a pressure load acting on the top flange over only the areas formed by the underlying web panels (see Figure 19). Stresses in the bottom flange in the vicinity of a support were obtained, and the maximum stress failure criterion was utilized to predict failure.

### **2.3.5 Fracture Mechanics Approach**

Due to the uncertainty surrounding the propensity for delamination in the 36 inch DWB, the uncertainty being the result of both the manufacturing quality and the difficulty in the analysis, the energy approach was also considered as an alternate means for predicting failure. The Virtual Crack Closure Technique (VCCT) was investigated for use with the FE model and analytical beam models to calculate the strain energy release rate as a function of applied loading and crack length.

Under the assumption that mode I deformation (caused by the interlaminar normal stress  $\sigma_z$ ) dominates, the Double Cantilever Beam (DCB) test was used to measure the critical mode I strain energy release rate,  $G_{IC}$ . Smith et al. [78] conducted DCB tests on specimens cut from the DWB flange in both the longitudinal and transverse directions. The transverse direction, while

more appropriate since the debond is theorized to grow across the width of the flange, was difficult to test because of the irregularity of the lay-up in the vicinity of the free edge and flange-web junction. Specimens cut from the longitudinal direction were more regular and were therefore used for the majority of the testing. The current author also applied the VCCT in FEA of the DCB test specimen to check the  $G_{IC}$  values obtained by Smith and to estimate the individual mode contributions.

The results of Smith et al.'s DCB testing suggested a very large critical strain energy release rate, between 1250 and 2460 J/m<sup>2</sup>, depending upon the technique used to calculate  $G_{IC}$  (e.g. modified beam theory or the direct integration method) and the cut direction of the specimen (longitudinal vs. transverse) [78]. A review of various carbon fiber composites in the literature indicates a range of  $G_{IC}$  values of only 140 to 540 J/m<sup>2</sup>. The high values measured by Smith were attributed to considerable fiber bridging and possibly some other non-linear behavior. Based on these extraordinarily high values, the fracture mechanics approach was abandoned as a means to predict delamination failure.

### 3 Strength Prediction: Results

#### 3.1 Failure Tests

The response of the 36 inch DWB in the quasi-static tests was linear-elastic up to failure, with little or no warning. Failure occurred suddenly with no visible warning signs, and upon initiation, the crack propagated instantaneously along the length of the beam. The visible debond extended between the two load patches, and in some cases, extended beyond the load patches up to roughly three-fourths of the beam length. In all cases, the top flange also showed signs of compression failure as shown in Figure 3, but it was not known whether this damage preceded or followed the delamination, since delamination of the top flange could likely cause local buckling.

Although the failure was “brittle” in the sense that the behavior was linear-elastic up to failure, only the top flange and part of the web in the vicinity of the load patches showed signs of damage. Thus, the failure was not catastrophic. In fact, post-failure testing indicated that the beams could still carry significant load, with a loss in stiffness of about 20% [3]. However, the addition of higher load would likely grow the delamination further along the length of the beam, reducing the stiffness with load. (These tests were conducted in displacement control.)

Tracking the crack growth during the tests using crack detection gages proved to be difficult, but in three of the four beams instrumented with crack detection gages, the first detectable change in strain occurred at the inside edge of a loading pad, indicating that failure initiates at the load patches, as expected. Subsequent gage readings suggested that the crack propagated inward toward mid-span. The readings on the fourth beam were inconclusive.

Local strain measurements on the web in the vicinity of the load patches indicate fairly significant transverse compressive strains directly under the load (see Figure 28 in Part 1). Furthermore, the compressive strains measure along the  $x$ -axis just under the top flange appeared to change sign just outside the load patch, in a manner similar to that of a beam on an elastic foundation (see Schniepp [3]). These measurements were compared with the finite element predictions in Part 1.

Post-failure inspection of the beams was also inconclusive. Inspection of the failure far away from the load patches suggests that the delamination initiates at the inner flange tapers and then propagates towards the free edges. This is evidenced by sections taken near the end of the

delaminations, which show delamination only at the taper and not at the free edge (Figure 20). Of course, this conclusion assumes that as the crack grows along the length of the beam, the growth also occurs inside-out, i.e. from the taper to the free edge. Given the amount of energy released at failure, it is impossible to know with certainty if this is true. Furthermore, it is still not clear whether the delamination precedes or follows compression failure. The inspection also revealed that only one side of the flange typically delaminates completely. In most cases, the visible crack at one free edge extends much longer along the length of the beam than the crack on the other free edge. This observation is consistent with the manufacturing variabilities from one side of the flange to the other.

The resulting strengths at each span and A- and B-allowables calculated using Weibull statistics were reported by Schniepp [3]. The shear load at failure was found to follow a linear dependence upon span length or aspect ratio (Figure 21), suggesting that the failure is moment controlled since the moment varies linearly with shear span length. However, the moment to failure was also found to vary with span, as shown in Figure 22. Moreover, the variation appears to be non-linear at shorter spans, as evidenced by the 8 inch DWB data<sup>5</sup>.

## **3.2 Stress Analysis**

### **3.2.1 Global Model**

The FE predicted deflection for all spans is within 0.1% and 3% of the MLB/Timoshenko beam theory prediction for point loads and patch loads, respectively, using the nodal fixity boundary condition at the neutral axis. The comparison of ply-level response with beam theory is also good, as shown in Figure 23 and Figure 24. Interestingly, the best match is found using the MLB point load solution rather than the patch load solution, which more closely matches the actual case as modeled in FEA. Using the point load MLB results, the axial strains and stresses are within 2% of the FEA solution in all plies, except for the  $\pm 45^\circ$  glass plies, where the error is around 20 to 25%. Web shear strains also show reasonable agreement, as evidenced by the far-field distributions shown previously in Part 1.

The theoretical strain predictions on the top surface are as much as 9% higher than the experimental strain “measurement” (calculated using the mean measured bending modulus).

---

<sup>5</sup> Note that the three shortest spans for the 8 inch DWB were tested using three-point loading, while all other data points are from four-point tests. Furthermore, the 36 inch DWB’s tests at a span of 5.49 m (18 ft) actually failed at the supports by local bending at the flange-web interface; this data point is included for comparison only.

This is due to the lower modulus resulting from the lay-up specified in the models. The modulus predicted using laminated beam theory is 42.3 GPa (6.13 Msi), whereas the mean measured value was 45.0 (6.53 Msi).

Figure 25 shows the variation of the failure function in the outermost carbon ply of the top flange in four-point loading tests under 445 kN (100 kips) per patch. The load patch causes a fairly significant stress concentration equal to approximately  $Fa = 0.12$ . This is an increase of between 10 and 30% over the mid-span stress level, depending upon the span. Similarly, the results from the three-point test models indicate stress concentrations between 15 and 45%. The stress concentrations are likely due to the increased local flange curvature caused by the transverse flexibility and warping effects discussed in Part 1.

The “measured” pressure distribution under the load patch is compared with the FE predicted distribution taken from the global model in Figure 26. The experimentally observed distribution suggests that most of the load is introduced in the flange region between the free edge and the taper. Furthermore, the pressure distribution is observed to be fairly uniform over the  $x$ -direction length of the flange, suggesting that the use of an elastomeric bearing pad provides a fairly uniform pressure distribution on the top surface of the flange. The FE results also demonstrate good pressure uniformity confirming the effectiveness of the pad representation in the model.

### 3.2.2 Free Edge Submodels

The free edge interlaminar stress distributions through the thickness of the top flange at seven different locations along the length of the beam are shown in Figure 27, Figure 28, and Figure 29. The inner edge of the loading pad is located at  $x = 423$  cm (166.5 inches), and the center of the pad is located at  $x = 411$  cm (162 inches), so the results should indicate the location of maximum stresses. However, these free edge values are approximations of singularities whenever the adjacent materials at an interface are different, so the actual magnitudes of the values have little meaning. Nevertheless, these figures demonstrate the general character of the through-the-thickness stress distributions.

At all locations, the free edge value of the interlaminar normal stresses  $\sigma_z$  is observed to be compressive at the primary carbon/glass interface, although there is a large jump from negative to positive. However, as we shall see below, the normal stress quickly changes sign at small distance away from the edge. In contrast to the normal stress, the interlaminar shear stress

$\tau_{xz}$  at the free edge is negligible at mid-span and then reaches a maximum (within the carbon/CSM sub-laminate) very near the carbon/glass interface, as shown in Figure 28, and the maximum appears to occur just outside the load patch at  $x = 424$  cm (167 inches). The other interlaminar shear stress  $\tau_{yz}$  also shows peaks near the primary carbon/glass interface, but the values are relatively low.

To calculate the width-averaged stresses for use in the Quadratic Strength Criterion, the variation of  $\sigma_z$  across the width of the flange at the primary carbon/glass interface is shown in Figure 30 and Figure 31 for the case of 445 kN (100 kips) per patch and  $\Delta T = -114$  °C (-205 °F). The normal stress  $\sigma_z$  is observed to increase initially from zero to a tensile value and then decrease to a compressive (possibly singular) value at the free edge. This effect has been observed in cross-ply and quasi-isotropic laminates at the interface between the 0° and 90° plies [25, 79], and these researchers have shown that the opposite effect (normal stress goes from zero to negative to positive singular) can be achieved by changing the lay-up.

The compressive values at the free edge would suggest that there is no mechanism to initiate delamination. However, for completeness, it is assumed here that the tensile portion of the normal stress profiles, just a short distance from the free edge, could promote delamination. Therefore, the width-averaging procedure is followed to calculate average free edge interlaminar stresses. Averaging over the tensile region,  $\sigma_z$  is found to be greatest at  $x = 419$  cm (165 inches) which is just inside the pad, although the value is only 262 kPa (38 psi). Similarly, the width-averaged shear stress  $\tau_{xz}$  is found to be only 2.21 MPa (321 psi). At  $x = 424$  cm (167 inches), where  $\tau_{xz}$  is highest, the width-averaged value is 15 MPa (2177 psi). However, just outside the pad, the average normal stress  $\sigma_z$  is only 131 kPa (19 psi).

The FE results actually indicate that the highest tensile normal stresses at the free edge occur in glass plies. For example, at  $x = 419$  cm (165 inches), large interlaminar normal and shear ( $\tau_{xz}$ ) stresses are observed at the interfaces between the  $\pm 45^\circ$  plies, as evident in Figure 27 and Figure 28. The  $y$ -direction stress profiles at this location are shown in Figure 32. Averaging over the very short tensile region only, the average interlaminar normal stress is 8.83 MPa (1280 psi). This high value suggests failure may occur within the all-glass portion of the flange (sub-laminate 2), contrary to experimental observations.

To investigate the effect of residual thermal stresses on the interlaminar stresses, the analysis was repeated for the case of no temperature change, i.e.  $\Delta T = 0$ . The ply-level stress

profiles for the primary carbon/glass interface are shown in Figure 33, Figure 34, and Figure 35. The results suggest that neglecting the residual thermal cure stresses reduces the interlaminar shear stresses but increases the interlaminar normal stress. The shear stress  $\tau_{xz}$  changes sign and becomes negligible at mid-span. The interlaminar shear stress  $\tau_{yz}$  also changes sign and decreases in magnitude.

Regarding the free edge stresses at the  $\pm 45^\circ$  glass ply interfaces, separation of the thermal and mechanical effects reveals that neglecting the change in temperature decreases the peak interlaminar stresses fairly significantly as shown in Figure 36 and Figure 37. However, even without the thermal effect, the mechanical contribution is still significant. For example,  $\sigma_{z,avg} = 5.58$  MPa (809 psi) for the case of  $\Delta T = 0$ .

### 3.2.3 Flange Taper Sub-models

Based on the results of the free edge analyses, the maximum stresses at the taper were expected to be located at the edge of the loading pad. The exact location of maximum stress was identified by examining the resulting stress contours in TAPERSUB1. The peak stresses were found to be located just outside the load patch at  $x = 424$  cm (166.75 inches). Therefore, the detailed sub-models TAPERSUB2 and TAPERSUB3 were positioned at this location, as well as at the mid-span location for comparison.

Contour plots of the interlaminar normal stress  $\sigma_z$  at the tip of the flange taper are shown in Figure 38 and Figure 39. The first figure indicates stress concentrations at not only the end of the taper, but also at two locations within the all-glass inner sublaminar. These last two locations correspond to interfaces between 0 and  $45^\circ$  plies (one of these interfaces was observed to experience high stresses at the free edge). The presence of tensile stresses throughout the volume is clearly demonstrated in Figure 39.

The  $y$ -direction stress profiles from TAPERSUB2 are shown in Figure 40 and Figure 41 for the mid-span and load patch locations, respectively. These stresses were calculated at the primary carbon/glass interface from the tip of the taper ( $x = 4.88$  cm or 1.92 inches, denoted by the leftmost dashed line) across the width of the flange to the free edge. The point at which the taper ends and the flange reaches its full thickness ( $x = 6.40$  cm or 2.52 inches) is denoted by the second dashed line. The web region is denoted by the third and fourth dashed lines. Note that in addition to the taper region response, the analysis also captures the local behavior in the vicinity of the flange/web junction at the free edge, although the latter results are not very accurate given

the coarseness of the mesh at the free edge. Interestingly, the normal stress at this interface is predicted to be tensile over the web panels at mid-span; near the load patch, the normal stress becomes highly compressive due to the applied load. The interlaminar shear stresses near the flange/web junction are also predicted to be much higher near the load patch.

The normal stress profiles in the local region around the taper tip for both the mid-span and load-patch locations are compared in Figure 42. Note that the stresses are much higher at the load patch location, as expected, with the normal stress changing sign and becoming compressive just inside the end of the taper ( $y = 6.40$  cm or 2.52 inches). The mid-span profile is smaller, yet still tensile, and the stress remains tensile across the entire width of the flange. Due to the lack of mesh refinement near the taper tip, the normal stress does not immediately go to zero at  $y$  less than 4.88 cm (1.92 inches), despite the fact that this is a free surface.

The TAPERSUB3 sub-model was constructed to provide greater mesh refinement at the taper tip. The resulting normal stress profile is compared with the previous TAPERSUB2 profile in Figure 43. The additional refinement confirms that the stresses do go to zero at the free surface. Elsewhere, the two profiles match very well. It is also interesting to observe the second smaller peak in the  $\sigma_z$  profile, which occurs just inside of the primary peak. This second peak corresponds to the singularity caused by the back corner of the fillet wedge, as shown in the inset image of Figure 43.

To assess the influence of the residual thermal stresses on the taper tip values, the analyses were repeated for the case of no mechanical loading and  $\Delta T = -114$  °C (-205 °F). The mechanical and thermal components of the  $\sigma_z$  profile at the load patch location are compared in Figure 44. The thermal curve is observed to be fairly large and remains tensile over the entire width of the flange. This behavior is likely an artifact of the FE representation of the flange/web junction and may explain the tensile normal stress across the width of the flange observed at mid-span. As discussed later in Sections 3.3.2.3 and 3.3.3, this feature of the thermal stresses causes problems in the ply width stress-averaging technique.

As in the free edge analyses, average stress values were obtained by averaging over a characteristic length of the flange width. In the case of the normal stress, the averaging length was defined as the distance between the taper tip and the point at which the stress changes sign and becomes compressive. The shear stresses are not considered here because they do not return to zero in the interior of the flange (this issue is explored further in the next section). The

average normal stress due solely to the thermal effect is 800 kPa (116 psi), while the mechanical component is 1.31 MPa (190 psi) at 445 kN (100 kips) applied load per patch. The total normal stress at 445 kN is 1.41 MPa (205 psi).

To check tensile stresses for possible failure within the all-glass portion, the nodal stresses along the 0/45° interface discussed previously were also determined. Then the ply-averaging method was used to calculate the average interlaminar stresses. The results suggest that the mechanical contribution to the normal stresses  $\sigma_z$  is 1.38 MPa (200 psi) at 445 kN, and the thermal contribution is 585 kPa (84.8 psi). The total normal stress becomes 2.03 MPa (295 psi). The interlaminar shear stresses are however rather small.

The results of the volume averaging technique are reviewed next. The resulting failure function calculated using the Quadratic Strength Criterion versus the distance away from the tip of the flange taper is shown in Figure 45 for the case of combined mechanical (445 kN) and thermal ( $\Delta T = -114$  °C) loading. The data points were empirically fit with a power law curve, which is the form of the stress concentration encountered in fracture mechanics. The resulting failure function due to only the thermal component is shown in Figure 46, and again the thermal component is found to be significant. Here, the influence of the multiple stress concentrations in the taper region can also be observed, as indicated by the breadth of the scatter between the two empirical curves.

### 3.2.4 Detailed Flange/Web Junction Model

The results of the detailed flange/web junction model analysis are reviewed next. The  $y$ -direction stress profiles at the primary carbon/glass interface are compared with the results from the previous TAPERSUB2 analysis in Figure 47 and Figure 48 for the mid-span location. The character of the  $\sigma_z$  profile is significantly different above the web junction, with even higher tensile stresses being predicted using the detailed model. Furthermore, the far-field response of TAPERSUB2 is recovered, i.e. far-field stress remains tensile. The interlaminar shear stress  $\tau_{yz}$  is also found to increase significantly near the web panel. The same profiles at the load patch location are shown in Figure 49, and Figure 50. Here again, large compressive stresses are predicted over the web panels, but the severity of the stress concentration is predicted to be much less using the detailed model. The shear stress  $\tau_{yz}$  is also predicted to be much smaller near the load patch. The other shear stress  $\tau_{yz}$  (not shown) remained negligible.

The results are inconclusive, but they illustrate the sensitivity of the stress field to the manner in which the geometric and material discontinuities are modeled. A more accurate representation would obviously model the filler portion of the web material as a layered material. However, aligning layered anisotropic elements so that the elemental coordinate systems follow the curved profile is a tedious process and was beyond the scope of the current study.

### **3.3 Strength Prediction**

#### **3.3.1 Compression Failure**

Using the End-Loaded Side Supported (ELSS) compression test, the Weibull mean compressive strength was calculated to be 518 MPa (75.1 ksi), and the Weibull scale parameter  $\alpha$  is 5.18. For comparison, Verghese reported around 350 MPa (50.8 ksi) for carbon/vinyl ester unidirectional composites with volume fractions between 55 to 58% and various sizing types [80]. Lesko [81] tested carbon/epoxy composites with volume fractions between 59 and 65% and various fiber sizings using the IITRI compression test method. He obtained values between 731 and 1100 MPa (106 and 160 ksi). As a point of reference, strengths as high as 1380 MPa (200 ksi) are not uncommon for carbon/epoxy composites. The low compression strength measured here is attributed to incompatibility between the carbon fiber with standard sizing and the vinyl ester resin, as well as fiber misalignment and significant matrix porosity.

The average measured strength value above was utilized in the maximum stress failure criterion to predict compression failure. Analysis of the compressive stresses indicated that the in-plane shear stresses were relatively small, so that the refinement gained by using the Hashin quadratic compression failure criterion was minimal. At the 11.9 m (39 ft) span, the predicted failure load is 458 kN (103 kips). This is in excellent agreement with the experimental value (95 kips).

#### **3.3.2 Delamination Failure**

##### **3.3.2.1 Interlaminar strength values**

Williams tested a total of 20 tensile specimens from the flange, and most failures occurred at the primary carbon/glass interface. The Weibull mean strength was found to be  $S_z = 1.16$  MPa (168 psi). This compares very well with the value obtained by Senne [4] for the 8 inch DWB, 1.14 MPa (165 psi). Senne also obtained a strength value for an all-glass version of the 8 inch DWB of 1.83 MPa (265 psi).

The results of the refinement study for the short beam shear specimen are summarized in Figure 51 and Figure 52 for the third-point ( $L/3$ ) location, which is far away from the loading point and supports. The results suggest that an accurate estimate of the interlaminar requires a fairly detailed refinement through the thickness. The use of 12 sublaminates or more was found to be necessary to accurately capture the stress distributions. The inclusion of temperature change from cure was found to have a significant effect on the stresses in the all-glass region, as well in the middle of the carbon/CSM region (Figure 53). This behavior is similar to that observed in the actual DWB model (Section 3.2.2). Interestingly, the stresses near the critical carbon/glass interface appear to be relatively insensitive to the change in temperature.

A total of 37 short beam shear specimens were tested using the short beam shear (SBS) test method to estimate the transverse shear strength,  $S_{xz}$ . The test samples were observed to fail at one of several key carbon/glass interfaces, including the primary interface. The resulting delamination was first observed at the ends of the beam. Following the procedure described in Section 2.3.2.1 and using the full 57 sub-laminate model (1 element per ply), the Weibull mean interlaminar shear strength  $S_{xz}$  was found to be 32.3 MPa (4670 psi). The procedure was repeated for 16 SBS samples taken from the all-glass web section, and the shear strength was determined to be 37.4 MPa (5430 psi).

### 3.3.2.2 Free Edge

At the location of maximum interlaminar normal stress  $\sigma_z$ , at  $x = 165$  inches, an applied load of 445 kN (100 kips) per load patch yields a failure function  $Fa$  of only 0.43, using the Quadratic Strength Criterion. Scaling the mechanical stresses to obtain a value of  $Fa = 1$ , the failure load at the 11.9 m (39 ft) span is predicted to be 2.28 MN (512 kips). At the location of maximum interlaminar shear stress  $\tau_{xz}$ , at  $x = 424$  cm (167 inches), 445 kN (100 kips) per patch yields  $Fa = 0.48$ . The predicted failure load found by scaling the mechanical contribution is 890 kN (200 kips) when  $\tau_{yz}$  is neglected. Given the mean failure load of 420 kN (94.5 kips) in the laboratory, these results obviously do not suggest failure by free edge delamination at the primary carbon/glass interface.

### 3.3.2.3 Taper Region

Using the width-averaged stresses computed in Section 3.2.3, the predicted failure at the 12.2 m span is 390 kN (87.7 kips) when  $\Delta T = 0$  and 359 kN (80.6 kips) when  $\Delta T = -114$  °C. These results are in good agreement with the experimental value of  $420 \pm 97.9$  kN ( $94.5 \pm 22$

kips). However, because of the large tensile stresses caused by the thermal loading which are predicted to extend across the entire flange width, the characteristic length changes with the amount of mechanical stress (applied load). Moreover, the average stress calculation is found to be very sensitive to the characteristic length. Consequently, the predicted failure loads are highly dependent upon the inclusion of the thermal component.

The volume-averaged stresses depend upon the radial characteristic used. Here, a length of 1.75 cm (0.688 inch), the thickness of the outer flange sub-laminate, was chosen. This length corresponds to about a 95% decay of the stress concentrations as shown in Figure 45. When the volume-averaged stresses are used and  $\Delta T = -114$  °C, the predicted failure load is 890 kN (200 kips). When  $\Delta T = 0$ , the predicted failure load is 1.17 MN (264 kips). Again, these predictions are much higher than the experimental value<sup>6</sup>.

Finally, using the interlaminar normal strength for the all-glass interface measured by Senne, failure at the 0/45° glass interface is predicted to occur at 379 kN (83.5 kips) per load patch. This value is in good agreement with the experimentally observed strengths, but failure within the all-glass laminate was never observed in any of the full-scale beam tests. Therefore, these results are questionable.

### 3.3.3 Effect of Geometry and Span Dependence

Given the success of both the compression and taper delamination analyses to predict failure at the 11.9 m (39 ft) span, the analyses were repeated for the 6.10 and 17.7 m (20 and 58 ft) span lengths. At each span, the two thermal cases were again considered:  $\Delta T = 0$  and  $\Delta T = -114$  °C. The resulting predicted shear loads and moments at failure for the compression failure mode are plotted against the experimental data in Figure 54 and Figure 55. Excellent agreement is found between the FEA prediction and the experimental results. Furthermore, inclusion of the residual thermal stresses provides the best fit. The span dependence of the moment capacity is also captured<sup>7</sup>.

Figure 56 shows the error in the strength prediction when the stress concentrations due to the load patches are neglected. Here the far-field (mid-span) stresses were used to predict failure. The failure loads are overestimated by 15 to 45% (corresponding to the stress

---

<sup>6</sup> These results were determined by volume averaging only over the carbon plies. Including the glass plies in the calculations would lower the average failure function  $Fa$  and therefore increase the predicted loads at failure (and the error relative to the measured value), because the interlaminar strengths of the glass material are higher.

<sup>7</sup> Recall that failure in the 6.10 m or 20 ft test was actually due to bearing at the support.

concentrations). It is also noteworthy that using the far-field stresses appears to eliminate the span dependence of the moment to capacity, suggesting that in fact the non-linearity of the moment-to-failure versus span curve is due to the stress concentrations at the load points.

Due to the lack of agreement between the FEA and experimental results at the 11.9 m (39 ft) span, the free edge analysis was not conducted at any other spans. The predicted shear load and moments at failure for the taper edge delamination failure mode were however calculated at each span using the ply-averaging method, and the results are compared with the experimental data in Figure 57 and Figure 58. Despite good agreement at the 12.2 and 18.3 m (40 and 60 ft) spans, we see that the predicted strength at the 6.10 m (20 ft) span is in gross error of the experimental results. Furthermore, when the residual thermal stresses are neglected, the error in predicted failure loads at all spans becomes worse, and the proper trend of decreasing shear capacity versus span is lost.

The predicted shear and moment capacities versus span using the volume stress averaging approach are shown in Figure 59 and Figure 60, respectively. Using this technique, the agreement at all spans is observed to be even worse with much higher strengths predicted. Furthermore, the shear capacity results show no span dependence.

#### **3.3.4 Uniform Loading**

The resulting failure function in the carbon plies in the bottom flange for the case of uniform loading is shown in Figure 61 for the case of 9.14 m (30 ft) and 12.2 m (40 ft) long beams. The stresses, and therefore the failure functions, were scaled to obtain a maximum value of  $Fa = 1.0$ . The resulting loads are reported in the figure. In both cases, failure is predicted at the supports, which in this case were modeled as standard bridge-type bearing pads. These results demonstrate the importance of accounting for stress concentrations in failure predictions, even for more realistic situations where concentrated loading does not occur.

### **3.4 Summary**

The results of the failure analysis of the 36 inch DWB, while not completely conclusive, suggest that the failure in four-point loading occurs by compression failure of the carbon fiber plies in the top flange near a load patch. The high compressive stresses, coupled with the relatively low measured compression strength for the carbon fiber plies leads to a relatively simple strength prediction. The evidence for compression failure is further reinforced by the

span-dependence of the shear/moment capacity. Consideration of the stress concentrations at the load patches improves the prediction, suggesting that simple laminated beam theory analysis which neglects the load patch contact problem will be in error and non-conservative.

While the failure has the appearance of a delamination event, the detailed analyses conducted in this study do not support this hypothesized failure mode. The free edge analyses at the 11.9 m (39 ft) span indicate relatively small interlaminar stresses at the primary carbon/glass interface. The prediction based on the taper analysis results at the same span showed excellent agreement with the experimental data, but the results at the other spans were in poor agreement with the experiment. Furthermore, in both cases, large interlaminar stresses were predicted within the all-glass inner flange sub-laminate at a location not consistent with the observed failure surfaces. Thus, the results of the finite element analyses for the free edge and taper analyses are dubious. Given the sensitivity of the free edge stresses to mesh refinement, lay-up, material properties, and thermal effects, as well as the considerable material variability in the actual beam, the results of the delamination analyses are inconclusive.

These results for the 36 inch DWB raise the question of whether the failure mode in the 8 inch DWB is really delamination. To check for possible compression failure in the 8 inch DWB, a simple laminated beam analysis using the MLB model (see Part 1) was completed. The carbon fiber ply stresses at mid-span were calculated, with  $\Delta T = -114$  °C. The failure load at each of the three spans tested was then estimated using the maximum stress failure criterion. Because the MLB model cannot capture the stress concentration at the load patch, predicted strengths are expected to be slightly high.

The resulting predicted failure curve for the 8 inch DWB is compared with the test data in Figure 62. Note that the predicted shear loads are significantly lower than the data points, but the slope of the curves are very close. The compression strength of the 36 inch DWB carbon plies (518 MPa or 75.1 ksi) was utilized in this prediction; a higher carbon fiber strength (e.g. 827-896 MPa or 120-130 ksi) would improve the fit considerably, and it is possible that the carbon plies in the 8 inch DWB are stronger in compression due to the use of a different carbon fiber (Hercules AS4D 36k as opposed to Fortafil 80k in the 36 inch DWB) and better processing. Therefore, these results are inconclusive.

## 4 Fatigue Life Predictions

An approach similar to that of Senne [4] was followed to develop fatigue life predictions. However, based on the evidence suggesting that the failure mode is compression failure of the carbon plies, the delamination analysis was not utilized. The finite element stress analysis developed in the previous sections was integrated into a code that accounts for stiffness reductions with cycles due to matrix cracking in the off-axis plies of the tensile flange. Shear stiffness reduction in the web panels were not considered due to the relatively low shear strains observed and the limited effect that the web performance has on the flange stresses. Empirical expressions for the stiffness reduction were taken from glass/vinyl ester coupon data. The remaining strength of the carbon fiber critical element was tracked using the critical element model of Reifsnider et al. [70]. Finally, fatigue predictions were generated for the 36 inch DWB at various load/stress levels. These predictions were then compared to results from two full-scale fatigue tests.

### 4.1 Integration of Stress Analysis into Life Prediction Code

#### 4.1.1 ANSYS® code

The ANSYS® Parametric Design Language (APDL) was used to automate the global model solution and post-processing employed in the stress analysis and failure prediction. The analysis was then inserted into a DO-LOOP structure, in which the cycle count  $n$  is incremented by a user defined amount,  $\Delta n$ . During each cycle, the critical element is checked for failure by comparing the remaining strength to the applied loading (failure function). If failure occurs, the code stops. Otherwise, the stresses in the off-axis plies are checked for failure and then discounted or degraded according to stiffness reduction curves specified by the user. The code can save the results of each model analysis in separate database files and parameter files, and writes  $Fr$  and  $Fa$  for the critical element to a summary output file. The entire process is repeated until ultimate failure occurs. The code is included in Appendix B.

#### 4.1.2 Critical Element

Given the lack of evidence to suggest delamination failure, only one critical element was monitored: the unidirectional carbon plies. Only the outermost ply was tracked, as the outer fibers experience the largest axial strain in bending. The variation of  $Fa$  in the carbon fiber plies

along the length of the beam was recorded at each cycle, but the maximum value near the load patch controlled failure.

The failure functions,  $Fa$ , were calculated using the appropriate strength criteria discussed in Chapter 2. The ply strength quantities used are summarized in Table 1. The remaining strength of each critical element was calculated using the iterative form of the remaining strength evolution integral suggested by Case [82]:

$$Fr_i = Fr_{i-1} - (1 - Fa_i) \left[ \left( \frac{no_i + \Delta n_i}{N_i} \right)^j - \left( \frac{no_i}{N_i} \right)^j \right] \quad (4-1)$$

where

$$Fr_1 = 1 - (1 - Fa_1) \left( \frac{\Delta n}{N_1} \right)^j \quad (4-2)$$

and

$$no_i = \left( \frac{1 - Fr_{i-1}}{1 - Fa_i} \right)^{1/j} N_i \quad (4-3)$$

and  $\Delta n_i$  is the cycle increment for the  $i^{th}$  iterative step. The quantity  $no_i$  is the number of “pseudo cycles” representing the elapsed cycles as if the fatigue process occurred at the current stress level  $Fa_i$  for the entire life until reaching the current remaining strength  $Fr_i$ .

The fatigue life of the carbon fiber plies was taken from fatigue data by Verghese [80] for the case of notched unidirectional laminates comprised of unsized carbon fibers in a vinyl ester matrix with a volume fraction between 55 and 59% fatigued at 10 Hz and a load ratio  $R = -1$  (tension-compression). The data was fit to a log-linear form suggested by [11]:

$$N_{fail} = 10 \left( \frac{Fa-A}{B} \right)^{1/p} \quad (4-4)$$

The constant parameters  $A$ ,  $B$ , and  $p$  were determined by fitting Verghese's data for the unsized fiber case and were found to be 1.348, -0.3287, and 0.5938, respectively. Verghese suggests that a fatigue limit may occur below  $Fa = 0.285$  (a stress level of around 150 MPa), but this suggestion is based on run-outs (no failure) at 1 million cycles. In the current analysis, it was assumed that no such limit exists and that the response above  $Fa = 0.285$  could be extrapolated to lower stress levels.

#### 4.1.3 Off-Axis Stiffness Reduction

As in Senne's work, stiffness reduction due to matrix cracking was assumed to occur in the tensile flange and in the tensile sub-flange [4]. Furthermore, damage was only assumed to occur in the off-axis glass plies. Damage in the CSM plies was neglected due to the low stress levels in the CSM and the negligible contribution of the CSM to the flange stiffness. Due to the low stress levels observed in the FEA results for web panels, they were assumed to maintain their initial stiffness. Coupon level stiffness reduction data was obtained from Post et al. [83]. They tested glass/vinyl ester laminates which were essentially quasi-isotropic (containing  $0^\circ$ ,  $90^\circ$ , and  $\pm 45^\circ$  plies and a CSM core). Dynamic stiffness reduction data using changes in extensometer strain was obtained for laminate stress levels  $Fa = 0.25$ ,  $0.30$ , and  $0.35$ , as shown in Figure 63. These curves demonstrate the three regions of damage which are typically observed in fiber-reinforced polymeric laminates: the initial region (I) in which a sharp drop in stiffness occurs due to matrix crack nucleation, an intermediate region (II) in which matrix cracks grow and reach a saturation level and delaminations form, and a final region (III) in which delaminations grow, fibers begin to fracture, and all of the various forms of damage begin to interact causing a "sudden death" [11].

The data also indicate a clear stress level dependence. To apply the data, however, it is necessary to estimate the ply-level stresses or failure functions  $Fa(ply)$  in the off-axis plies which are degrading over time. Classical laminate theory and the maximum stress criterion were used to back-calculate  $Fa(ply)$  as a function of the laminate levels,  $Fa(lam)$ . Ply-level strength values were taken from the work of Phifer [12] (see Table 1). Phifer extracted ply-level strengths from laminate tests using CLT, and the resulting ply strength values were found to depend upon the

type of laminate tested. The average measured transverse tensile strength  $Y_t$  and in-plane shear strength  $S$  were utilized for the current study.

The CLT analysis indicates that the failure function in the 90° plies is initially 3.8 times the laminate applied stress level prior to any stiffness changes, i.e.

$$Fa(90^\circ) = (3.8) Fa(lam) \quad (4-5)$$

Similarly,

$$Fa(\pm 45^\circ) = (1.8) Fa(lam)$$

Therefore, the data from Post et al. [83] corresponds to  $Fa$  ranges of 0.95 to 1 for the 90° plies, and 0.45 to 0.63 for the  $\pm 45^\circ$  plies. However, the ply level stresses in the off-axis plies calculated in the FE models are lower, as shown in Table 2 (discussed in next section). Using the relationships above, the  $Fa$  range in the 90° plies requires stiffness reduction data at  $Fa(lam) = 0.11$  to 0.25, which is below the ranges tested by Post et al. Similarly, the  $\pm 45^\circ$  plies require  $Fa(lam) = 0.20$  to 0.31. Obtaining stiffness reduction data at such low stress levels is impractical given the long lives required. Therefore, extrapolation was used to estimate the stiffness reduction curves at the lower applied stress levels.

First, it is noted that the CLT calculations suggest that the 90° plies in the laminate of Post et al. are nearly failed in the first fatigue cycle for even the lowest applied stress level. This is supported by quasi-static test data which demonstrates a gradual “knee” in the stress-strain response at the stress level required to crack the 90° plies. Thus, the initial stiffness reduction in the curves of Figure 63 is likely due mainly to the degradation of the 90° plies, as well as some cracking of the  $\pm 45^\circ$  plies and possibly the CSM. The gradual stiffness reduction in region II is likely due to (slower) crack development in the  $\pm 45^\circ$  and CSM plies. Therefore, the laminate stiffness curves are comprised of separate contributions from the damage modes of the 90°,  $\pm 45^\circ$ , and CSM plies. In the current study, however, it is assumed that the shapes of the stiffness reduction curves for the 90°,  $\pm 45^\circ$ , and CSM plies are the same. This assumption will simplify the process of applying the curves to the FE model.

In order to estimate stiffness reduction curves for the lower ply-level stress levels calculated above, the following extrapolation process was used. First, the data in Figure 63 were

fit using non-linear regression. The following form, similar to that used commonly in the area of visco-elasticity to model reductions in mechanical properties caused by temperature changes [84], was found to work well for the current stiffness reduction data:

$$\hat{E} = (\hat{E}_1 - \hat{E}_2) \exp\left[-\left(\frac{\hat{n}}{N_1}\right)^{m_1}\right] + \hat{E}_2 \exp\left[-\left(\frac{\hat{n}}{N_2}\right)^{m_2}\right] \quad (4-6)$$

The hat (^) symbol is used to denote normalized quantities. Thus,  $\hat{E}$  is the normalized stiffness, which is a function of the normalized life,  $\hat{n}$ . The first stiffness parameter  $\hat{E}_1$  is the initial normalized stiffness and is therefore equal to 1. The second stiffness parameter  $\hat{E}_2$  is a normalized stiffness plateau that might exist in a cross-ply laminate and roughly describes the stiffness at half-life ( $n/N_{fail} = 0.5$ ) for the quasi-isotropic laminates. The parameters  $N_1$  and  $N_2$  roughly correspond to the normalized lives at the transition from one region to another. Finally,  $m_1$  and  $m_2$  are parameters which describe the shape or breadth of the transitions.

The three curves of Figure 63 were fit using Equation (4-6), and the unknown parameters determined. To extrapolate to lower load levels, the parameters three values for  $N_2$ ,  $m_1$ , and  $m_2$  each were averaged, as they showed little variation with  $Fa$  (Figure 64). The parameters  $\hat{E}_2$  and  $N_1$ , however, demonstrated a clear dependence upon  $Fa$  and were therefore fit with a parabolic curve and exponential curve, respectively (Figure 65). In the former case,  $\hat{E}_2$  was forced to equal 1 at  $Fa(lam) = 0$  to recover the initial stiffness at a zero damage state. The use of an exponential form for  $N_1$  was based on the best fit; note that the exponential function causes  $N_1$  to decay to zero at  $Fa(lam) = 0$ . The projected curve at a lower stress level is found using the average parameters  $N_2$ ,  $m_1$ , and  $m_2$ , and the projected parameters  $\hat{E}_2$  and  $N_1$ . The resulting extrapolations at lower  $Fa(ply)$  values are shown in Figure 66, along with the original data.

#### 4.1.4 Ply-Level Stresses Calculations

To apply the estimated stiffness reduction curves, the ply-level stresses were extracted from each layer of the bottom flange inner sub-laminate and the bottom sub-flange in the global model, and the  $Fa(ply)$  values were calculated using the maximum stress criterion. The  $Fa(ply)$  values vary along the length of the beam, because of the gradient in moment resultant.

Furthermore, the length of the flange is composed of 139 elements. It would be impractical to attempt to apply separate stiffness reductions to each element, so a simpler scheme was devised. The half-span length was divided into 10 zones, so that the change in strain in any given zone was around 10%. Representative elements within each zone were then selected, and the average element stresses for all elements in each zone were averaged to obtain an average zone stress level.

A review of the  $y$ -direction variation in stresses indicated little change across the width of the flange, so elements located between the free edge and flange-web interface were monitored (refer to Figure 8). These elements were set to calculate ply-level stresses in all layers (using KEYOPT(8)=1 in ANSYS®). Specifically, the stresses in representative  $90^\circ$  and  $\pm 45^\circ$  plies were extracted for the bottom flange inner sublaminates and the bottom subflange. The maximum initial stresses in each ply were shown previously in Table 2. The in-plane stress  $\sigma_{22}$  in representative off-axis plies along the length of the beam is shown in Figure 67. The effect of including the residual thermal stresses is indicated by two curves for the cases of  $\Delta T = -114^\circ\text{C}$  and  $\Delta T = 0$ . The results suggest that accounting for the residual thermal cure stresses increases the stress levels in the off-axis plies significantly.

Once the average zone ply stresses are computed, Equations (4-5) are solved for  $Fa(lam)$  and the projected stiffness reduction curve is determined using the extrapolation method described above. To illustrate the use of zones for the stiffness reductions, the FE predicted variation of axial strain along the flange (half-span) length for a 11.9 m (39 ft) beam under four-point loading with 445 kN (100 kips) per load patch is shown in Figure 68.

#### 4.1.5 Procedure

Once all of the material inputs are specified, the fatigue life prediction can be executed. However, a few technical issues remain. First of all, in order to apply the stiffness reduction curves and to capture the entire reduction (regions, I, II, and III), the fatigue life must be known *a priori*. But of course, the life is the unknown that we are trying to determine. Therefore, the typical approach is to assume a life, run the analysis to failure, and then compare the predicted life to the assumed life. If necessary, the analysis is then re-run with a new assumed life. This process is repeated until the assumed life and predicted life converge [85]. The second issue is how to choose an appropriate cycle increment,  $\Delta n$ . Usually, an iterative procedure is used to check for convergence of the predicted fatigue life as  $\Delta n$  becomes smaller. However, as the

results will indicate, the change in  $Fa$  with cycles is very small, so the results will be relatively insensitive to the size of the cycle increment.

## 4.2 Fatigue Predictions for the DWB

The procedure developed above was employed to generate a fatigue-life ( $S-N$ ) curve for the DWB under the transverse loading. Only the 11.9 m (39 ft) span length was considered. Predictions for both four-point and three-point loading were generated to compare with the fatigue test results (below). The three-point model was constructed in the same manner detailed above for the four-point model. A similar 10-zone division was utilized in the three-point model to calculate ply level  $Fa$  values and apply stiffness reductions. Normalized stiffness reduction curves for the effective bending modulus of the DWB were also constructed by calculating the maximum deflection at mid-span for each cycle increment. Because the total deflection is comprised of a shear component, the change in deflection actually yields a change in effective bending stiffness, not the actual bending stiffness.

## 4.3 Fatigue Tests

Due to the limited availability of the beams for destructive testing, only two DWB's were tested in fatigue using MTS actuators and control system. The first beam was tested in four-point geometry with loads applied at the third points, as in the static testing. The beam length was slightly over 12.2 m (40 ft), and the center-of-bearing (COB) to COB span length was 11.9 m (39 ft). The beam was loaded to a maximum deflection equal to 1.52 cm (0.6 inches), approximately two times the maximum predicted service deflection in the Route 601 Bridge. The corresponding load was 133 kN (30 kips) per actuator, which corresponds to about 30% of the ultimate static failure load (94.5 kips). A load ratio of  $R = 0.1$  and a frequency of 1.1 Hz was used. The test was stopped after 4.9 million cycles due to mechanical problems.

The second beam was loaded to approximately 60% ultimate failure stress to promote failure within a reasonable time. This stress level corresponds to 267 kN (60 kips) in the four-point test geometry; however, the capacity of the actuators was only 222 kN (50 kips). Therefore, the test geometry was changed to a three-point loading geometry to utilize a larger 890 kN (200 kip) actuator that was available. Again, a 11.9 m (39 ft) COB-to-COB span length was used; the second beam was slightly longer at 13.4 m (44 ft), yielding a 33 cm (13 inch) overhang on each end. Because three-point test results were not available, the ultimate failure

for this geometry was estimated using the static strength prediction developed in Chapter 2. The predicted strength for the compression failure mode is 302 kPa (68 kip) shear capacity or 2.49 MN-m (1835 kip-ft) moment capacity. The resulting center point test load was 60% x 2 x 302 kN = 363 kN (81.6 kip). The test at the 60% load level was incomplete at the time of publication, so results for this level are not available.

In both tests, stiffness reduction was monitored by periodically interrupting the fatigue cycling to perform quasi-static loading tests. During the quasi-static tests, the mid-span deflections and inner corner pad deflections at one end were measured. Furthermore, axial flange strains and web shear strains were measured. The effective bending modulus was calculated using the flange strains, since the deflection measurements are less accurate. This yields the change in the actual bending stiffness only, which is slightly different than the change in effective bending stiffness calculated using the FEA results. However, the web panels are not expected to experience significant stiffness reduction and the shear deformation accounts for only 15% of the total deflection at the 11.9 m (39 ft span), so the error between the two methods is likely to be small.

#### **4.4 Results**

The resulting fatigue life curve for the 11.9 m (39 ft) four-point test geometry is shown in Figure 69. The results suggest that at the 133 kN (30 kip) load level, failure is predicted to occur at 4.4 million cycles, while the experimental test (indicated as a run-out in the figure) was stopped 4.9 million cycles with no signs of damage. Failure is predicted to occur at 32,000 cycles for the 363 kN (81.6 kip) load level; the testing is incomplete.

The predicted stiffness reduction curves for the three load levels are shown in Figure 70. The cycle count has been normalized by the cycles at failure for each load level. The reductions in stiffness are quite small: a maximum of only 0.5% at the 133 kN (30 kip) load level. The experimentally observed stiffness reduction for the lower load level is shown in Figure 71. The data show considerable noise due to the inherent limitations of the measurements, but the variation in stiffness is no larger than 0.2% at the 133 kN (30 kip) load level. Thus, the results indicate that the off-axis ply damage has little effect on the beam's performance.

The maximum possible stiffness reduction can be estimated by completely discounting the 90°, ±45°, and CSM plies in the bottom flange (sub-laminate 2) and the bottom sub-flange. Laminated beam theory analysis with these plies completely discounted indicates less than a 1%

reduction in beam stiffness. In the life prediction methodology, the plies are of course only partially degraded according to their stress level. Furthermore, that stress level decreases moving away from the load patches towards the ends of the beam. So, it is not surprising that so little stiffness reduction is observed.

The result is that the stress level in the critical element, the carbon plies, essentially remains constant over the entire life of the beam. This is shown in Figure 72, where the remaining strength ( $F_r$ ) and applied stress curves ( $F_a$ ) for the three load levels are given. The fact that  $F_a$  remains constant in the critical element makes the life prediction trivial, as the cycles at failure can be estimated by simply determining  $F_a$  from the stress analysis and picking off the cycles at failure from the  $S-N$  curve for the carbon/vinyl ester ply. It is important, however, to consider the effect of the stress concentration on the fatigue life. A 30 to 45% increase in the carbon ply  $F_a$  at the load patch may decrease the fatigue life by one or two decades on a logarithmic scale. Therefore, analytical beam models which cannot capture this effect will cause large errors in the predicted fatigue performance.

The carbon ply  $S-N$  curve from Verghese [80] is also shown in Figure 69 for comparison. Note that the beam predicted lives are slightly less than those predicted directly using the carbon ply  $S-N$  curve; part of this difference may be due to the (slight) stiffness reduction, and part may be due to the size of the cycle increment  $\Delta n$  used in the analyses.

## 5 Conclusions and Future Work

The first objective of this study was to develop a strength prediction for the 36 inch DWB. A strength based approach to predict delamination onset was followed in which average interlaminar stresses at the critical locations were compared to the interlaminar strengths using the Quadratic Strength Criterion. Detailed finite element analysis of the free edge, utilizing successive sub-models, did not indicate failure at that location. The analysis of the taper region was inconclusive, as the ply-averaged stresses were found to be very sensitive to the definition of the characteristic length. This was partly due to the existence of multiple singularities in the taper fillet regions, as well as the strong influence of the residual thermal stresses. The simplified FE representation of the flange/web junction may have also influenced the behavior of the interlaminar stresses.

On the other hand, the predicted beam strengths assuming compression failure in the carbon plies of the top flange demonstrated excellent agreement with the experimental data. In addition, this analysis was able to capture the span dependence of the moment capacity which was observed experimentally. Therefore, despite the appearance of a delamination failure, the analyses suggest that the actual failure mode is compression. However, the possibility of a delamination failure or interaction between the compression and delamination modes remains. A check for possible compression failure in the 8 inch DWB was inconclusive, as the actual compression strength of the material is unknown.

Based on the assumption of compression failure, a fatigue life prediction was conducted using a remaining strength damage model. Stiffness reductions in the off-axis plies of the tensile flange and sub-flange were modeled using data extrapolated from coupon tests, but the resulting change in the stress level of the critical element was negligible. Therefore, the life at a given applied load level can be predicted simply by determining the stress level in the carbon plies and determining the corresponding cycles to failure from the fatigue curve for the carbon/vinyl ester material. The validity of the prediction could not be verified due to limited fatigue test data.

A strength prediction based on an in-plane compression failure mode is greatly simplified, as only in-plane stresses in the flange are required. This would suggest the use of a closed-form solution such as laminated beam theory. However, the stress concentration at the load patch (or a support) can increase the local stresses by as much as 45% depending upon the

type of loading and test geometry, and the error in predicted life from neglecting this effect can be as much as two decades. Ordinary beam theory cannot capture these stress concentrations, so finite element analysis is recommended. The use of a more sophisticated analytical model might prove useful in capturing the stress concentration.

To further understand the failure of the 36 inch DWB and to develop a closed-form stress analysis, the author recommends the following additional work:

- Compression testing of the 8 inch DWB flange material should be conducted to check for compression failure.
- A finite element analysis of the 8 inch DWB is also recommended to more accurately calculate the compressive stresses and to check the interlaminar stresses predicted using Senne's approach.
- The third order laminated beam theory (TLBT) and the higher order sandwich theory of Frostig, examined in Part 1, should be investigated as possible means of capturing the load patch stress concentration.
- The fatigue testing started as part of this study should be completed. The beam tested at 267 kN (60 kips) per load patch should be run to failure to capture any possible stiffness reduction and to observe the fatigue life. The first beam tested at 133 kN (30 kips) should be tested to failure to assess the remaining strength.

# Figures and Tables

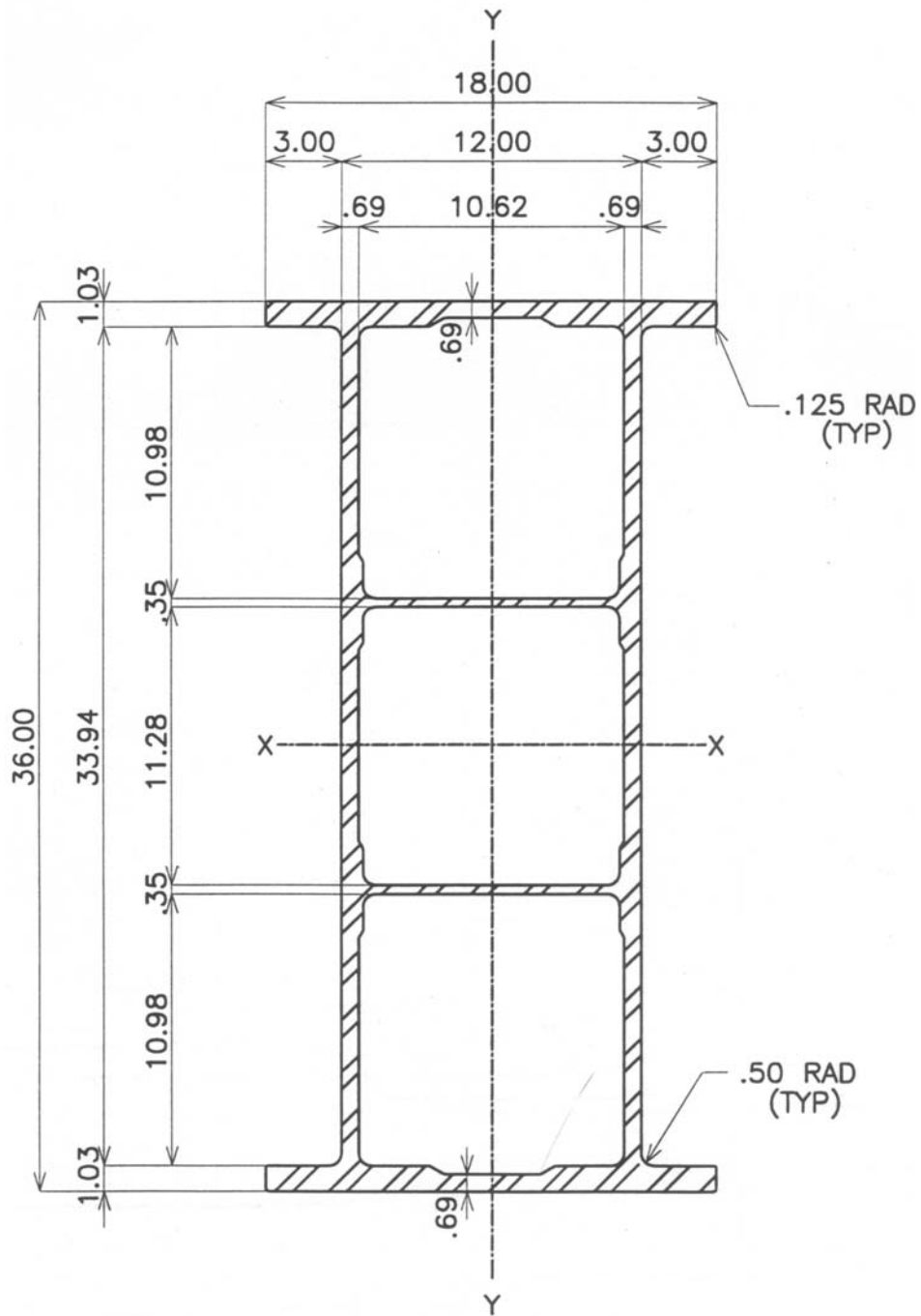


Figure 1. Strongwell's 36 inch DWB (dimensions in inches).

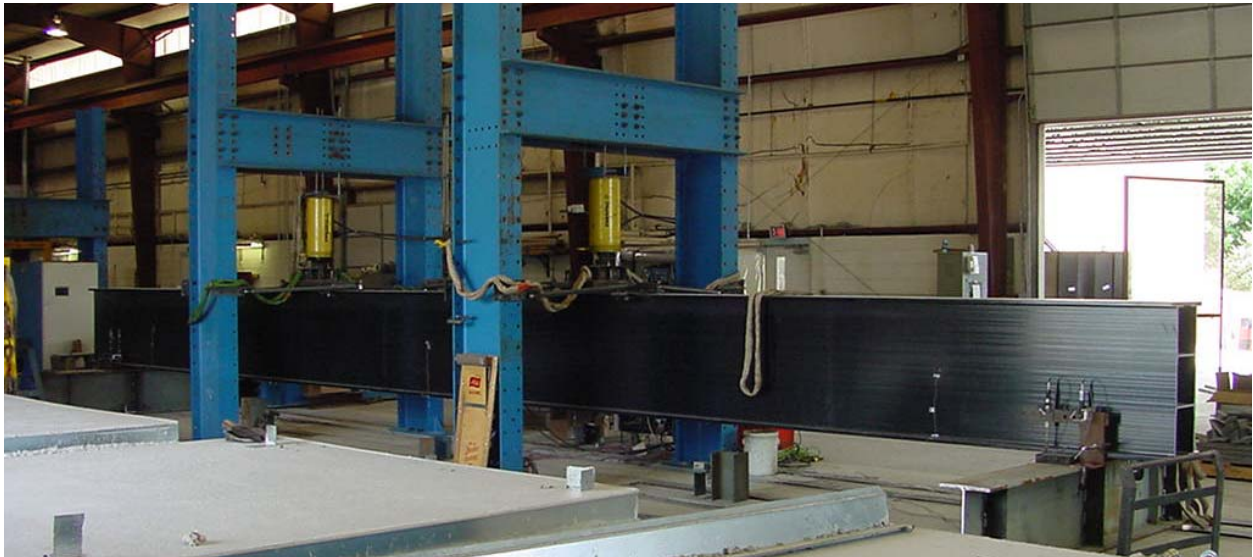


Figure 2. Four-point bend test set-up for 36 inch DWB (18.3 m or 60 ft span shown).



Figure 3. Failure of the compressive flange of a 36 inch DWB under the loading patch.

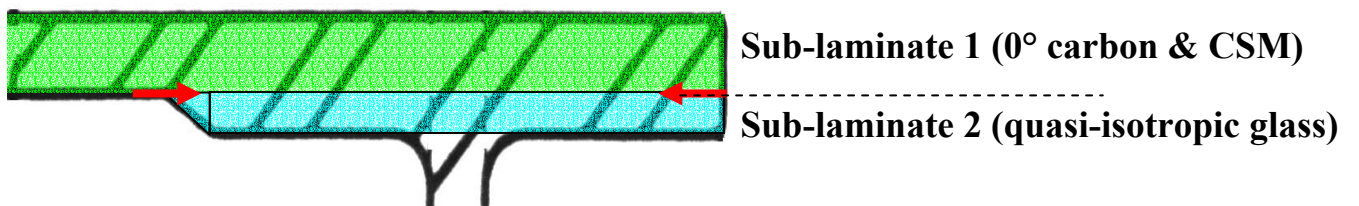


Figure 4. Sub-laminate construction of the DWB's flange. Arrows indicate possible delamination sites.

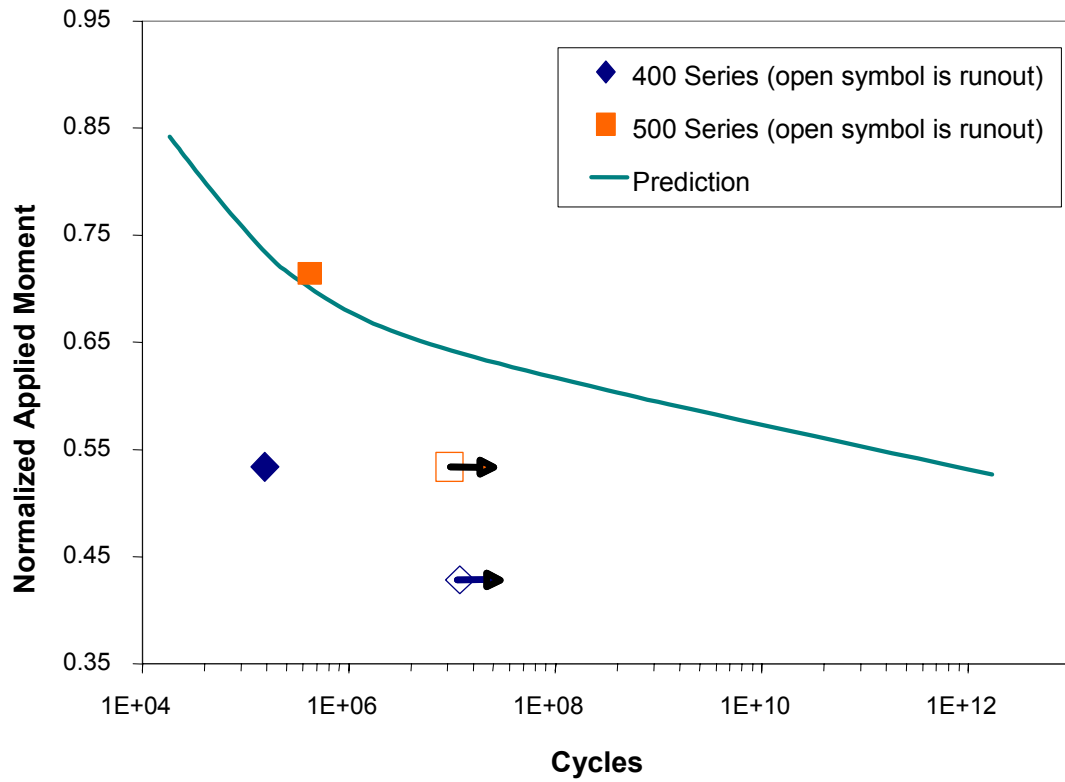
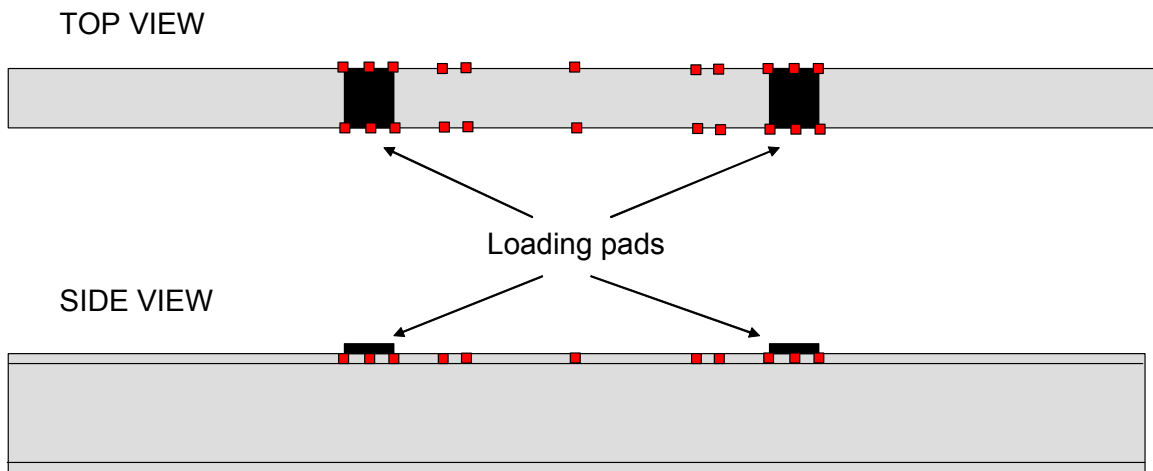


Figure 5. 8 inch DWB fatigue curves: prediction vs. data.



■ ■ ■ ■ Crack detection gages bonded to free edge of top flange

Figure 6. Locations of crack detection gages.

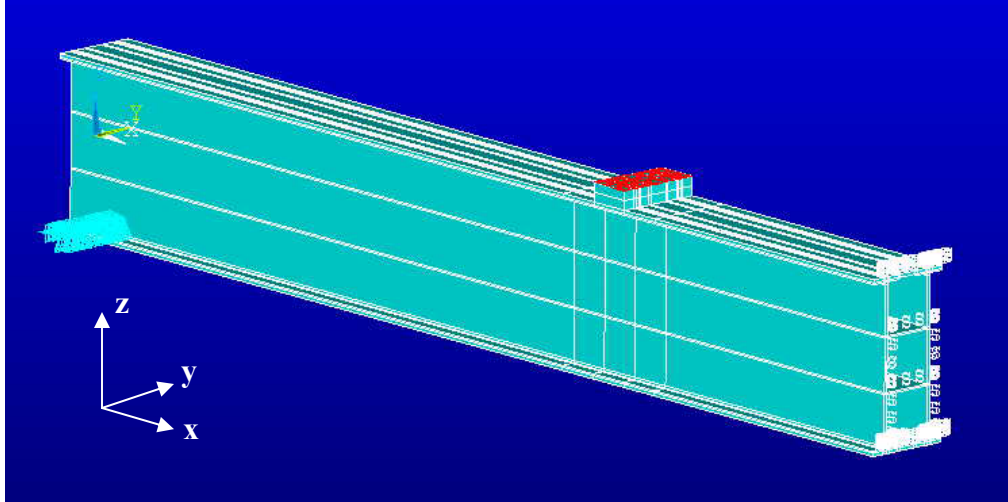


Figure 7. Half-beam model used in FE global analysis (11.9 m span).

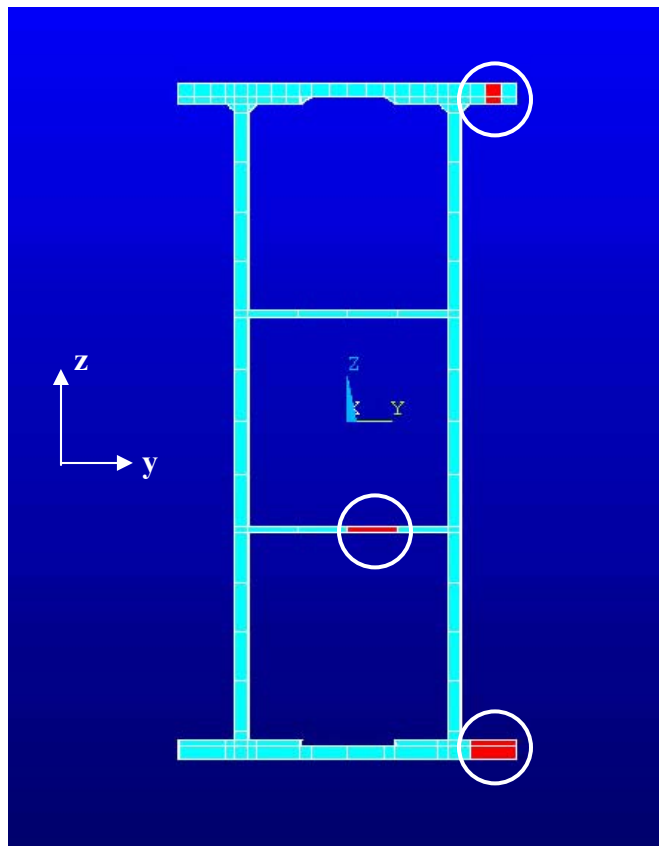


Figure 8. Cross-section of global DWB model, showing the location of the elements used in the stress calculations.

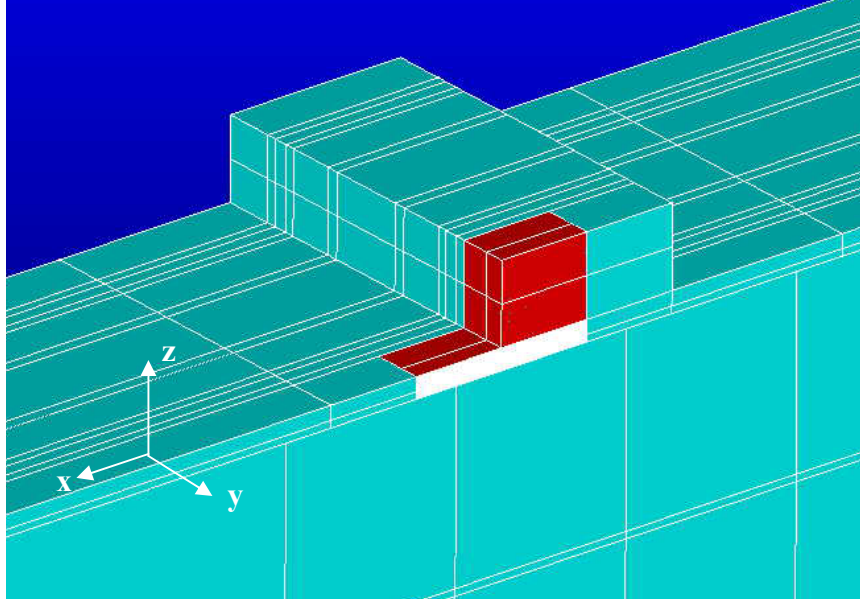


Figure 9. Close-up of load patch showing locations of EDGESUB1 (in red).

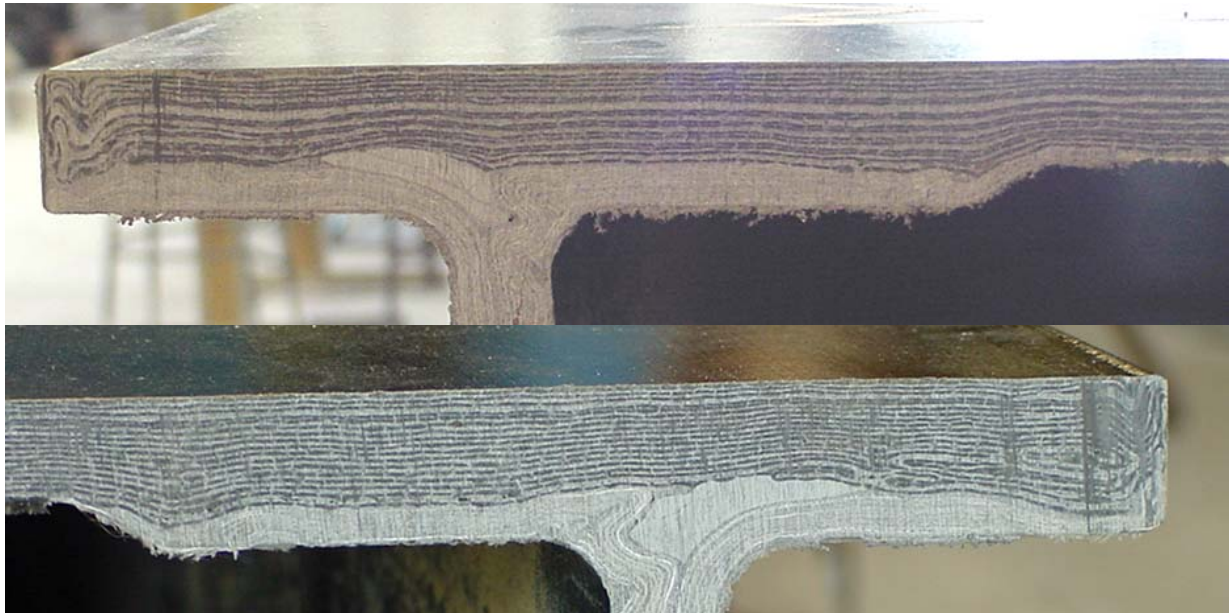


Figure 10. End view of DWB showing lay-up detail on both sides of flange.

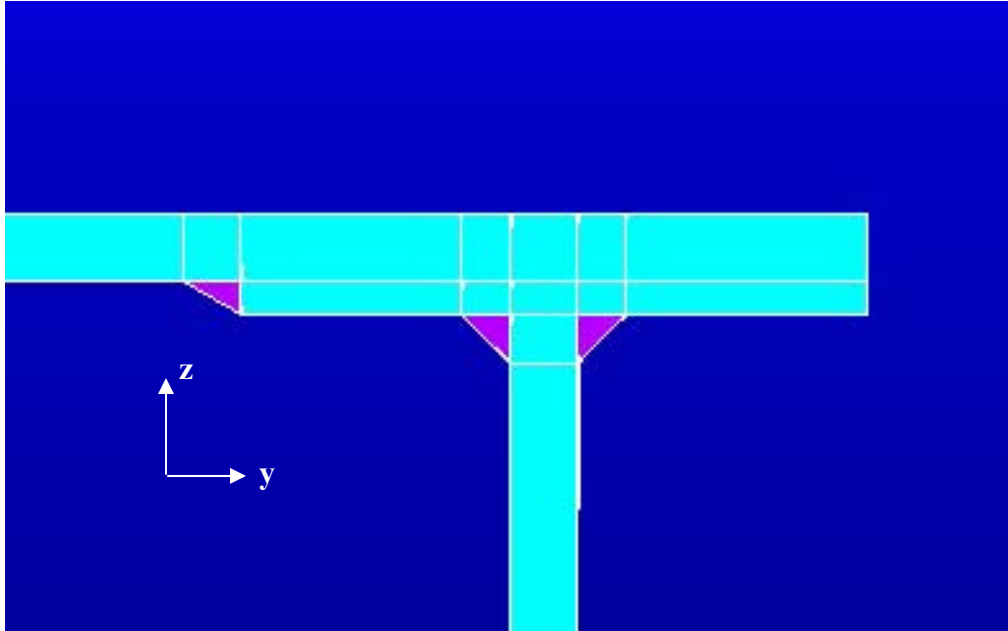


Figure 11. Cross-section view of global FE model used for the taper region stress analysis.

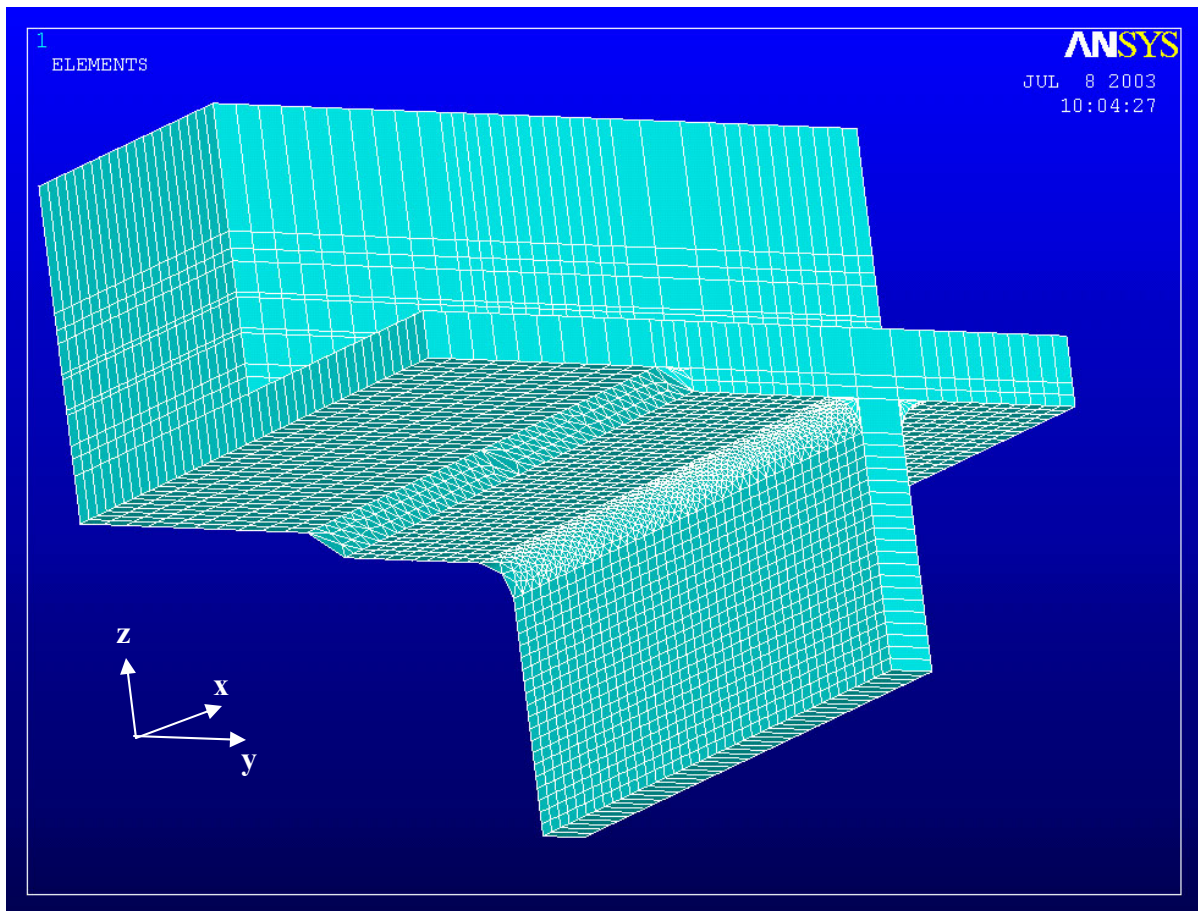


Figure 12. Intermediate FE submodel (EDGESUB1) used for the taper region stress analysis.

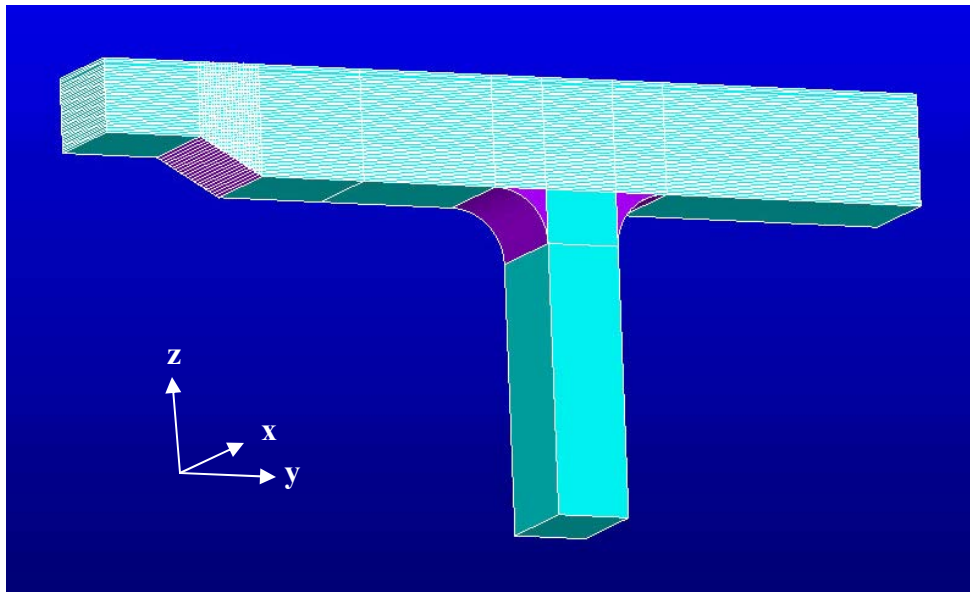


Figure 13. Detailed FE submodel (TAPERSUB2) used in the taper region stress analysis.

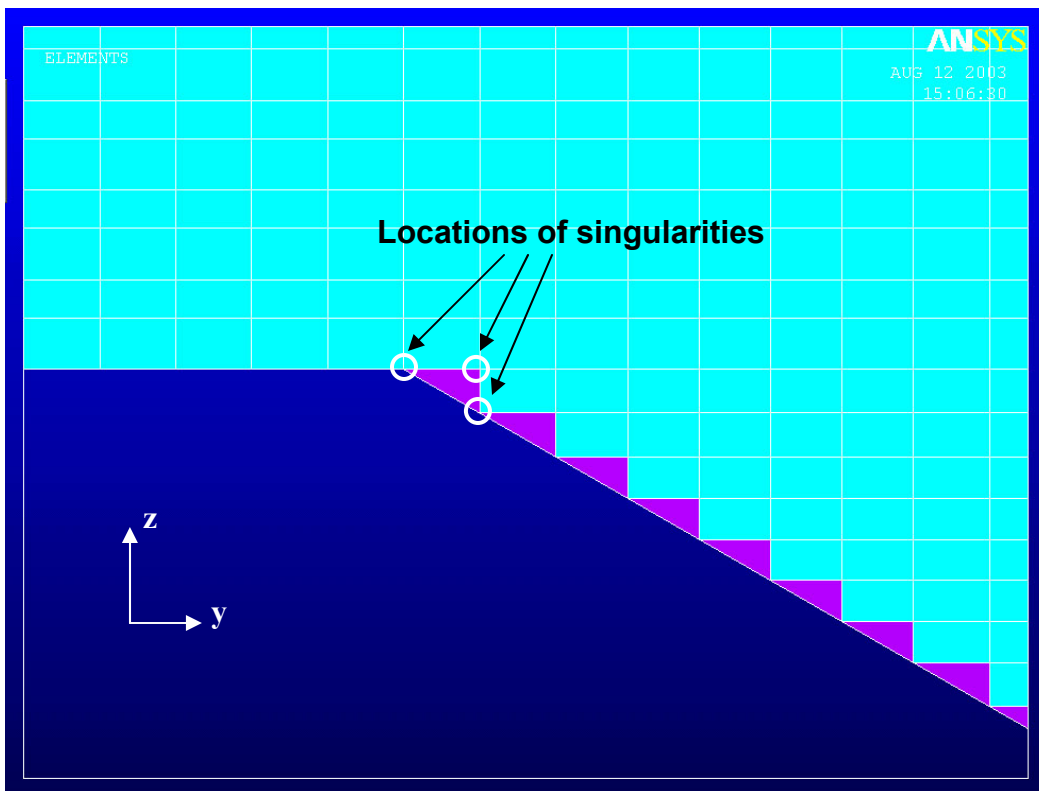


Figure 14. Close-up of TAPERSUB2 taper region showing fillet detail.

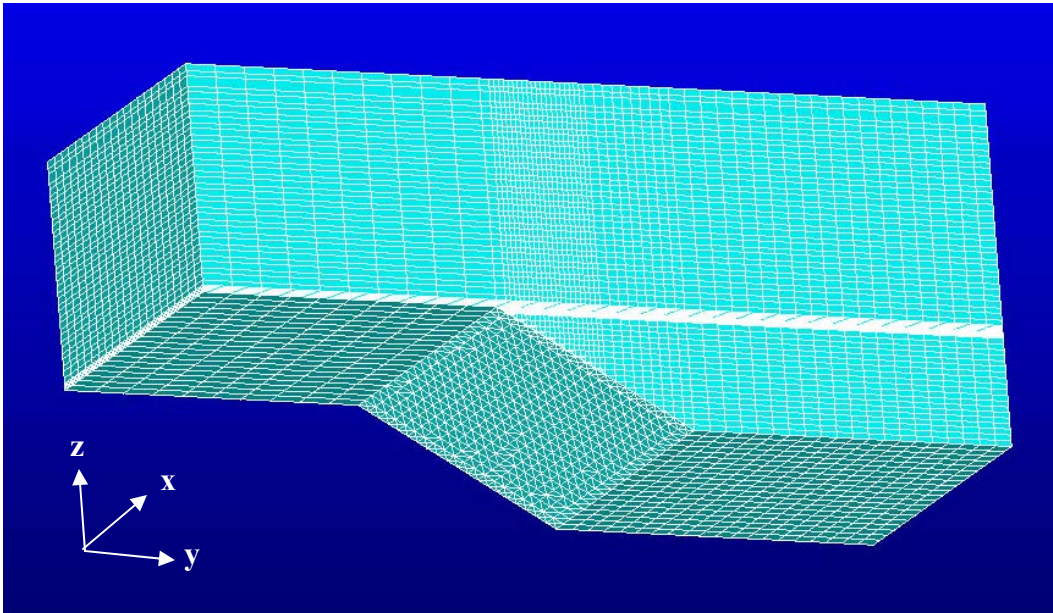


Figure 15. TAPERSUB3 used in the taper analyses.

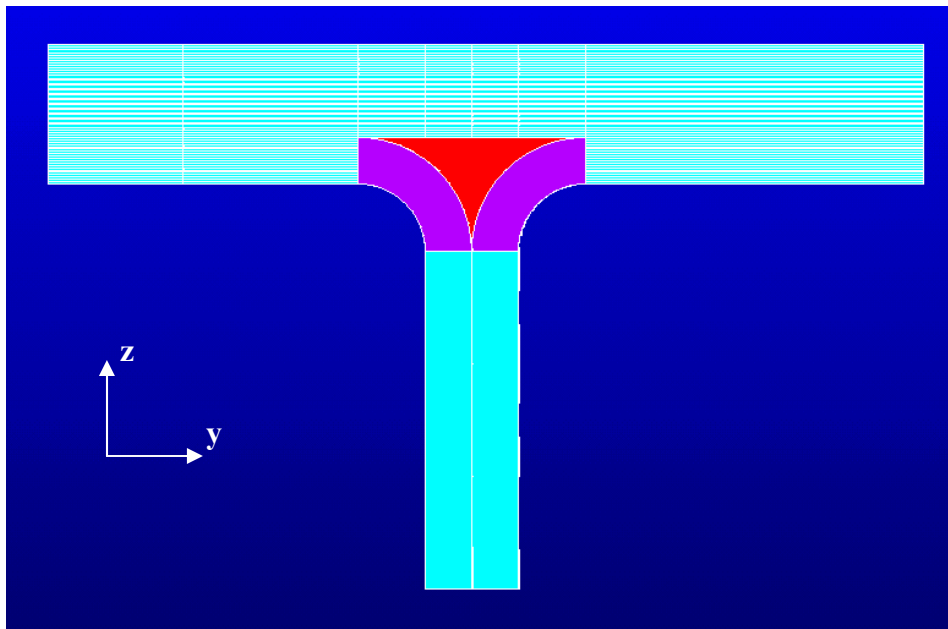


Figure 16. Detailed representation of the flange/web junction.



Figure 17. Tensile test specimen to obtain  $S_z$  at primary carbon/glass interface.

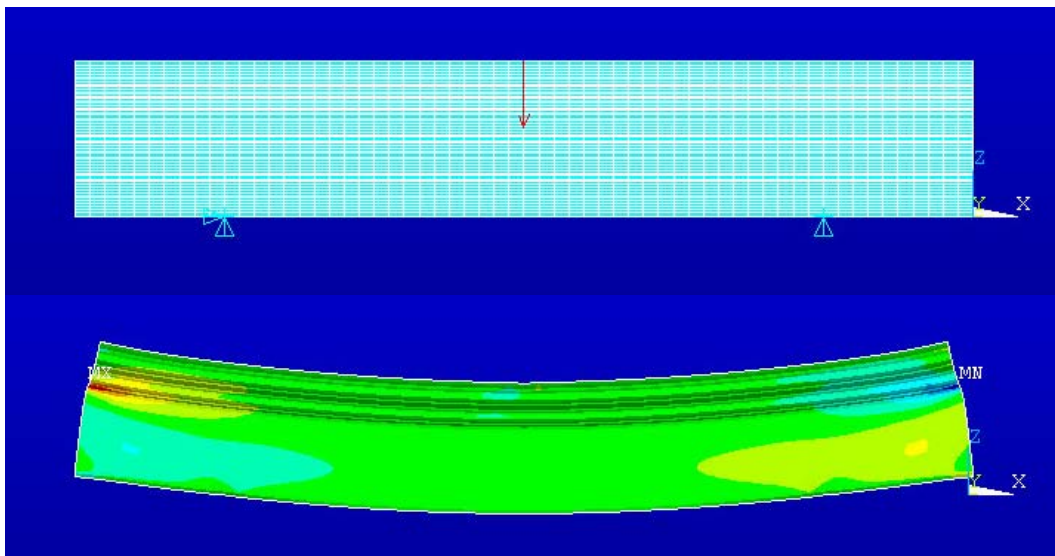


Figure 18. FEA model of SBS test on flange coupon. Colored contours indicate transverse shear stress,  $\tau_{xz}$ .

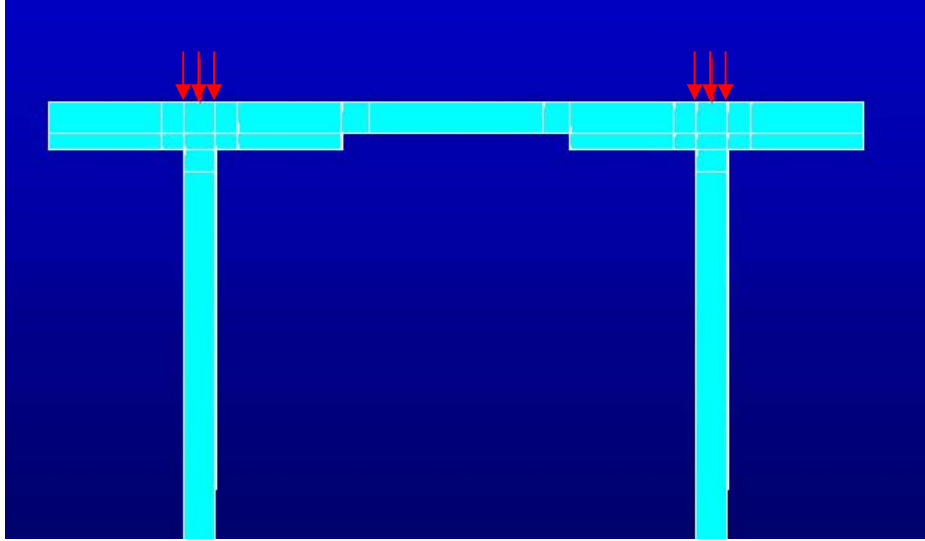


Figure 19. Finite element model for the uniform distributed loading case, showing how the load was introduced (area pressure loads indicated by the arrows).

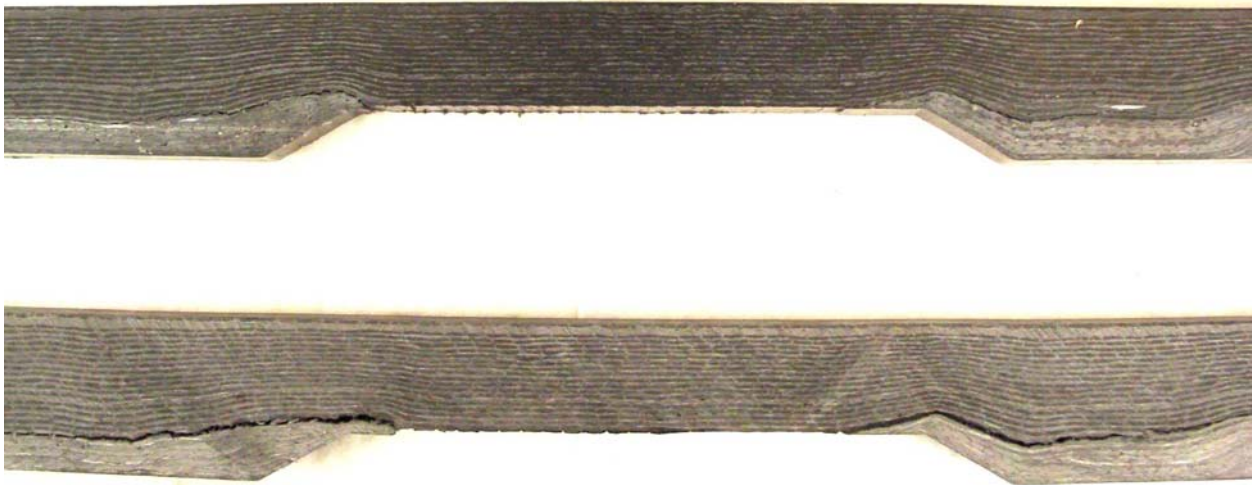


Figure 20. Possible delamination at the taper in two different beams. (Samples taken from near the end of the delamination.)

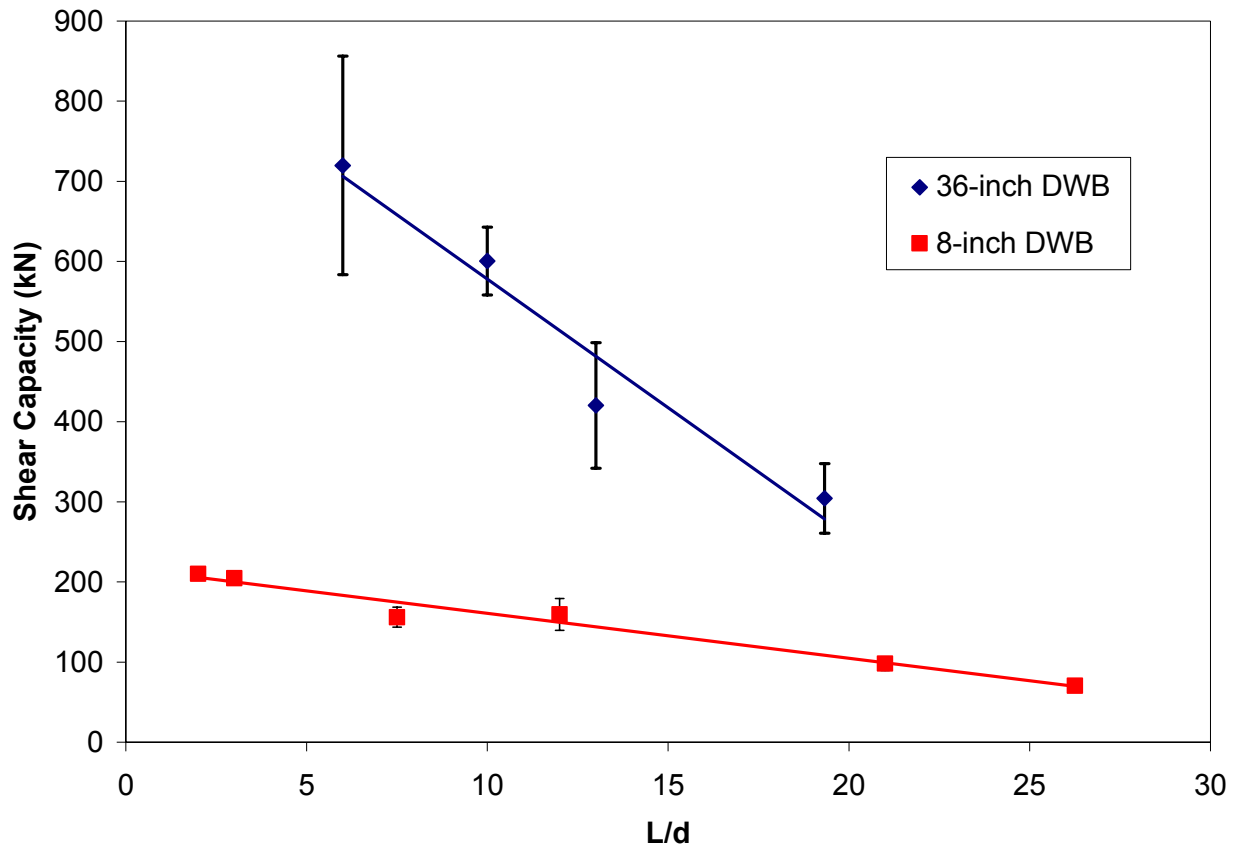


Figure 21. Span dependence of the shear capacity for both the 8 inch and 36 inch DWB's.

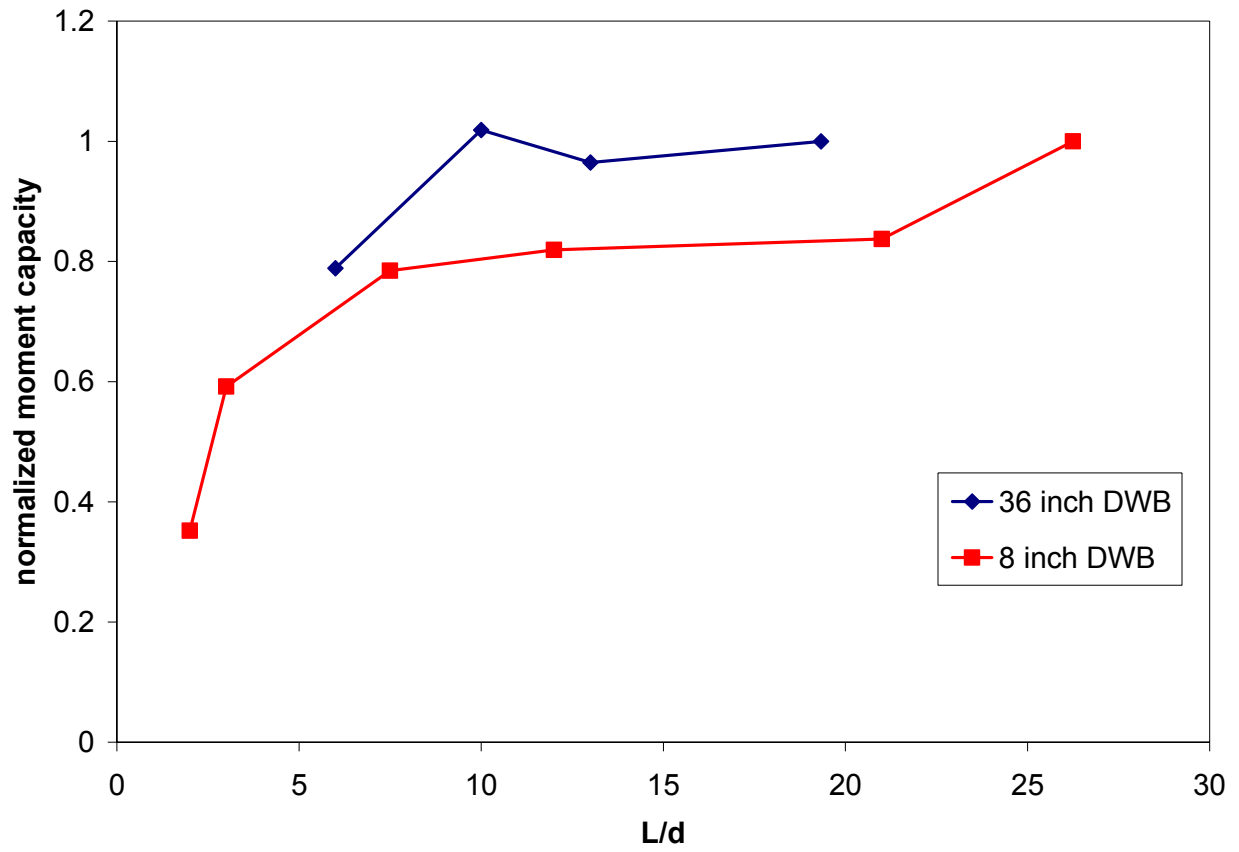


Figure 22. Span dependence of the moment capacity for both the 8 inch and 36 inch DWB's. The moment capacity has been normalized with respect to the maximum (long span) value to better demonstrate the variation for the 8 inch DWB.

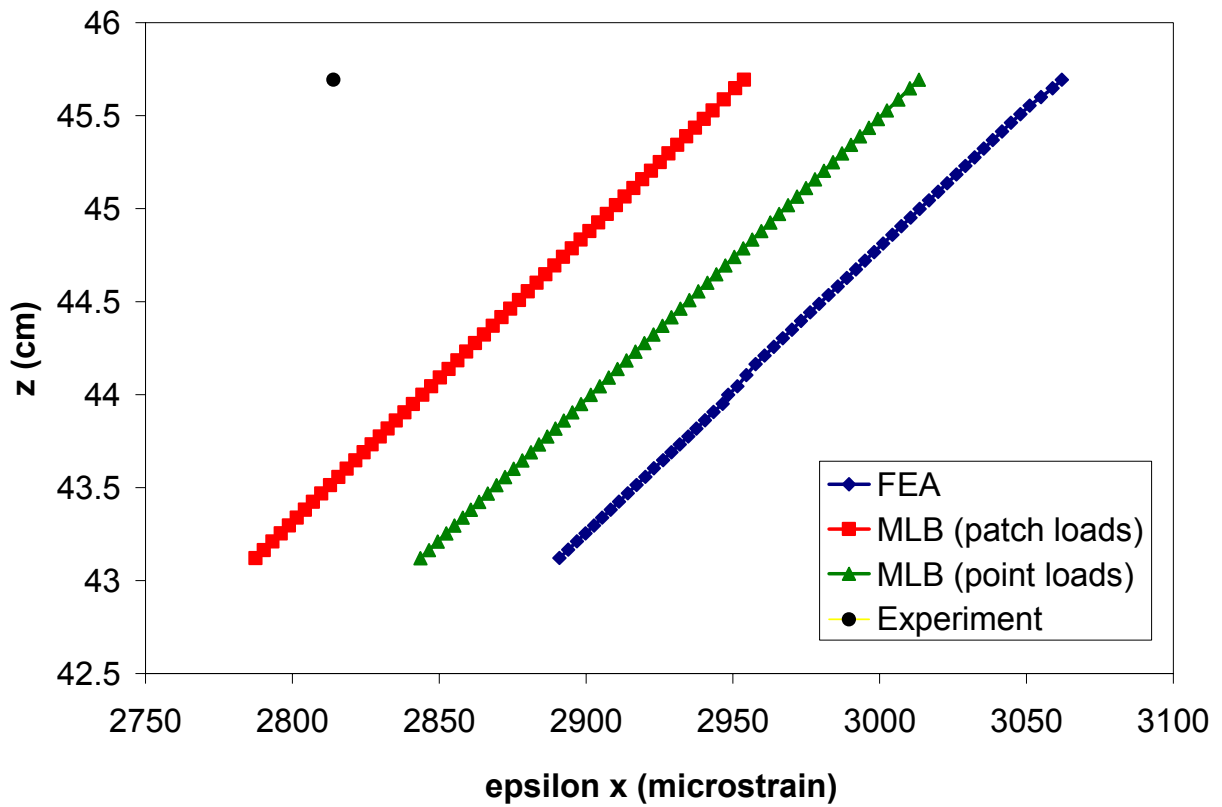


Figure 23. Axial strain through the thickness of the top flange in the constant moment region of an 11.9 m (39 ft) beam under four-point loading, as predicted using the global FE model and two different MLB/Timoshenko solutions: point loading and patch loading.

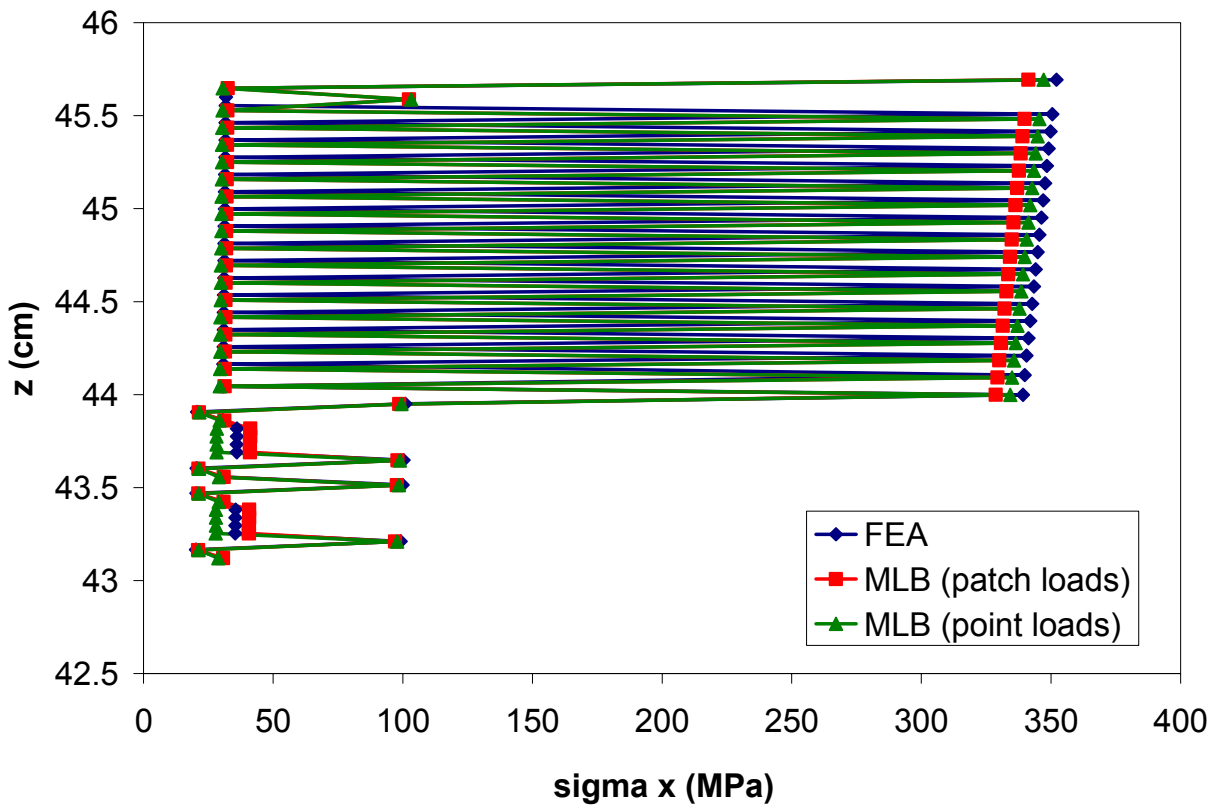


Figure 24. Axial stress through the thickness of the top flange in the constant moment region of an 11.9 m (39 ft) beam under four-point loading, as predicted using the global FE model and two different MLB/Timoshenko solutions: point loading and patch loading.

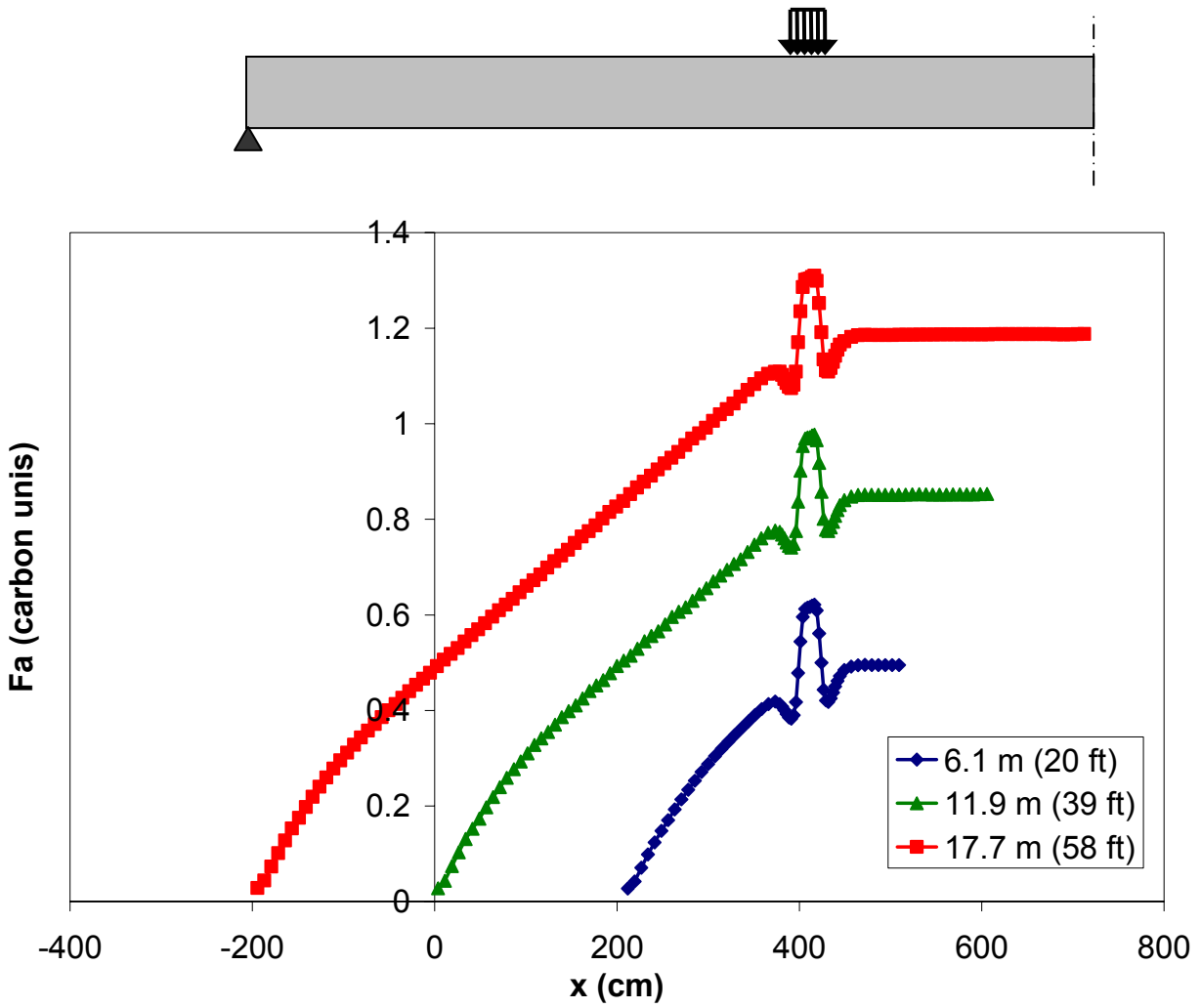


Figure 25. Failure function in the outer carbon plies of the top flange, demonstrating the stress concentration at the load patches in a four-point loading test using load patches. (Half-beam schematic at top illustrates geometry for 6.1 m beam only.)

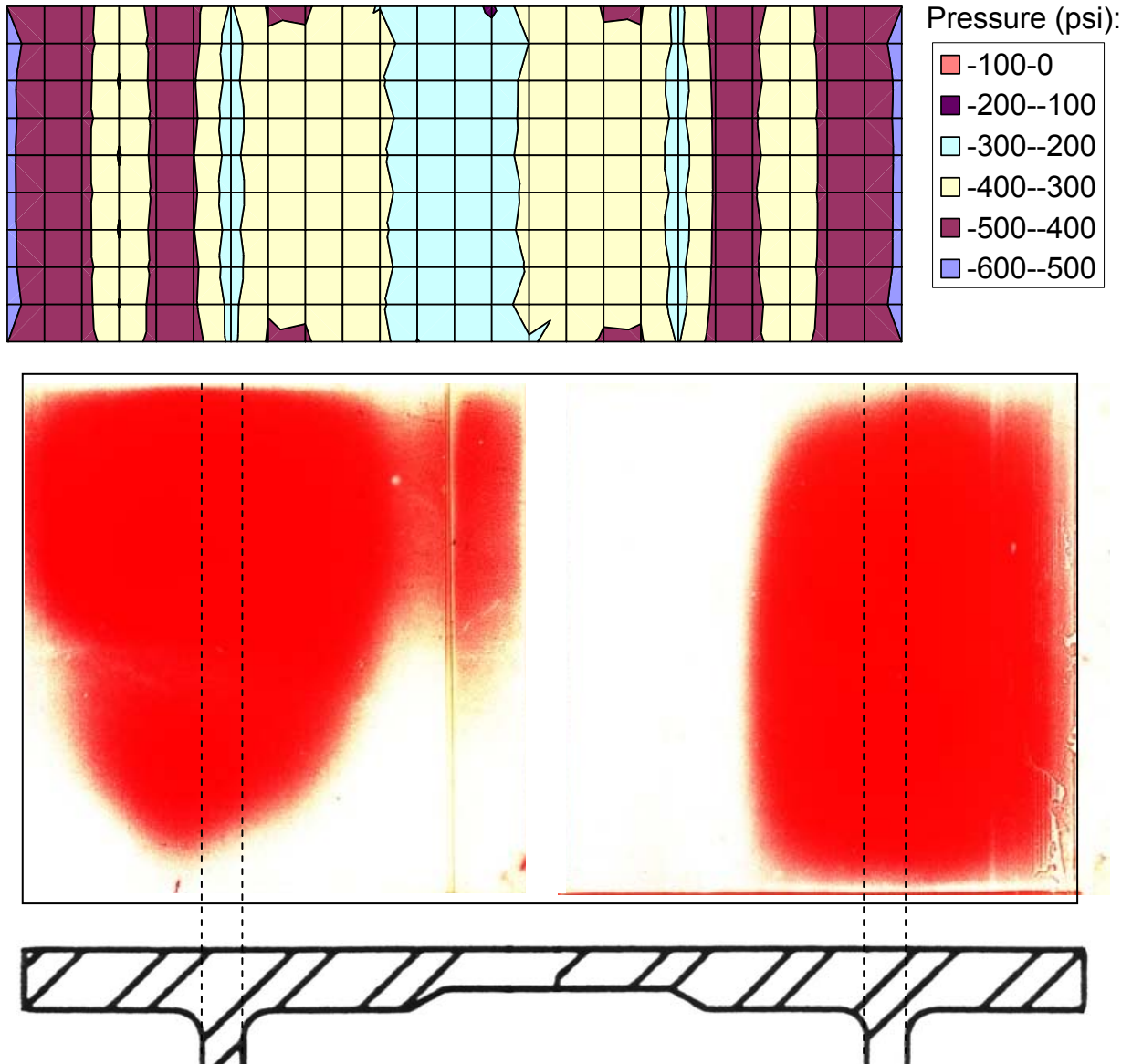


Figure 26. Qualitative comparison of the FEA predicted and experimentally observed pressure distributions under a load patch.

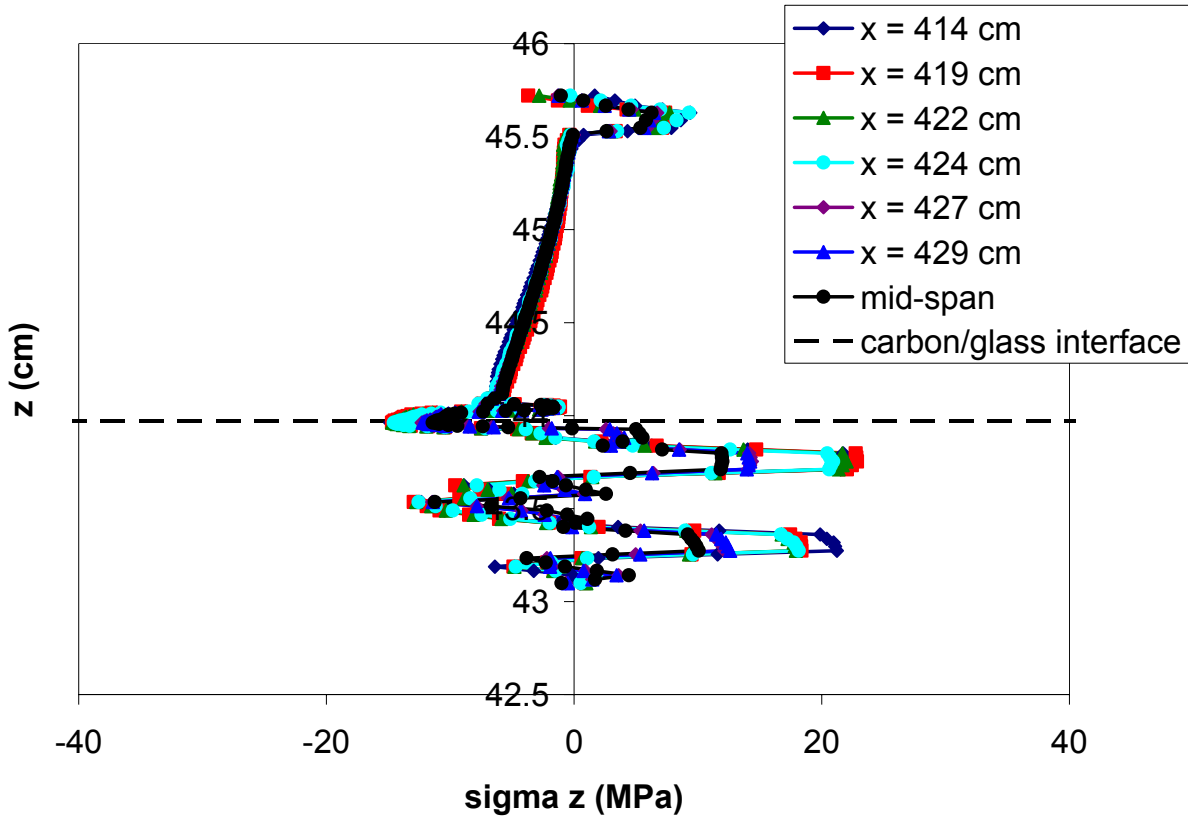


Figure 27. The interlaminar normal stress  $\sigma_z$  through the thickness of the top flange at the free edge at various locations along the length of an 11.9 m (39 ft) beam under four-point loading.

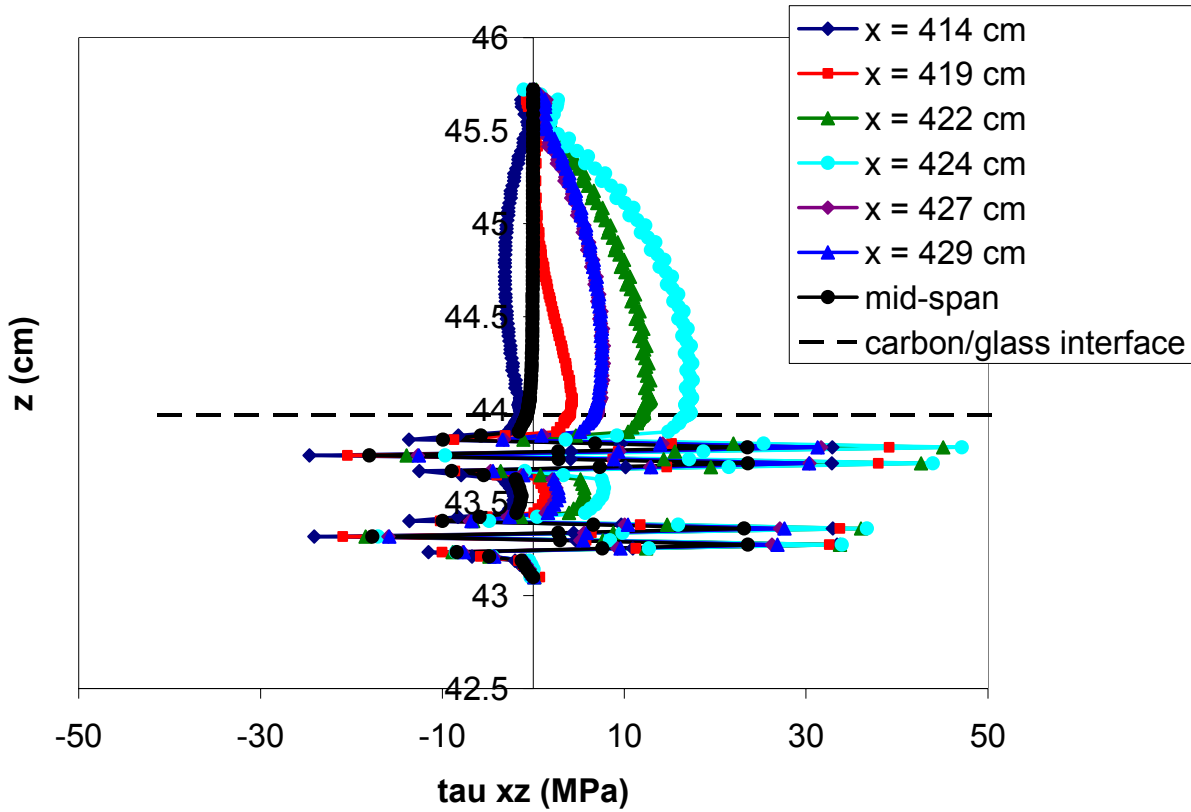


Figure 28. The interlaminar shear stress  $\tau_{xz}$  through the thickness of the top flange at the free edge of the top flange at various locations along the length of an 11.9 m (39 ft) beam under four-point loading.

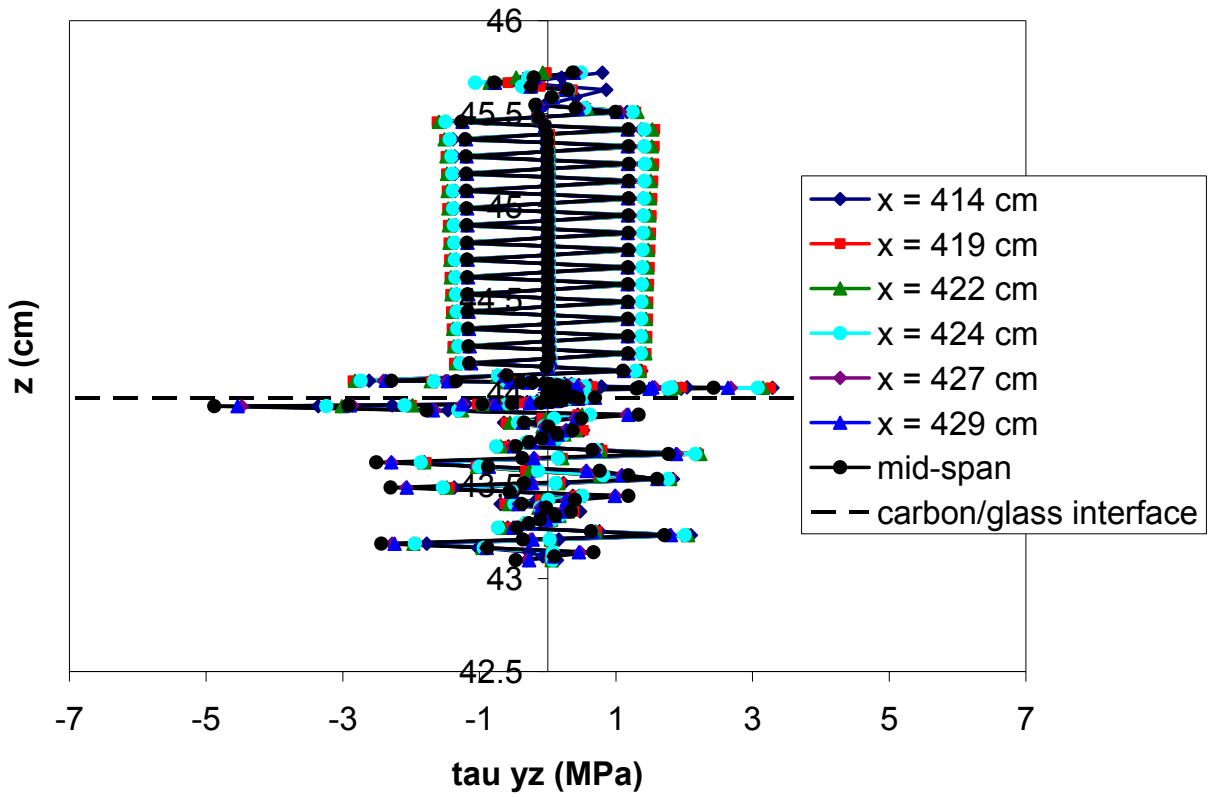


Figure 29. The interlaminar shear stress  $\tau_{yz}$  through the thickness of the top flange at the free edge of the top flange at various locations along the length of an 11.9 m (39 ft) beam under four-point loading.

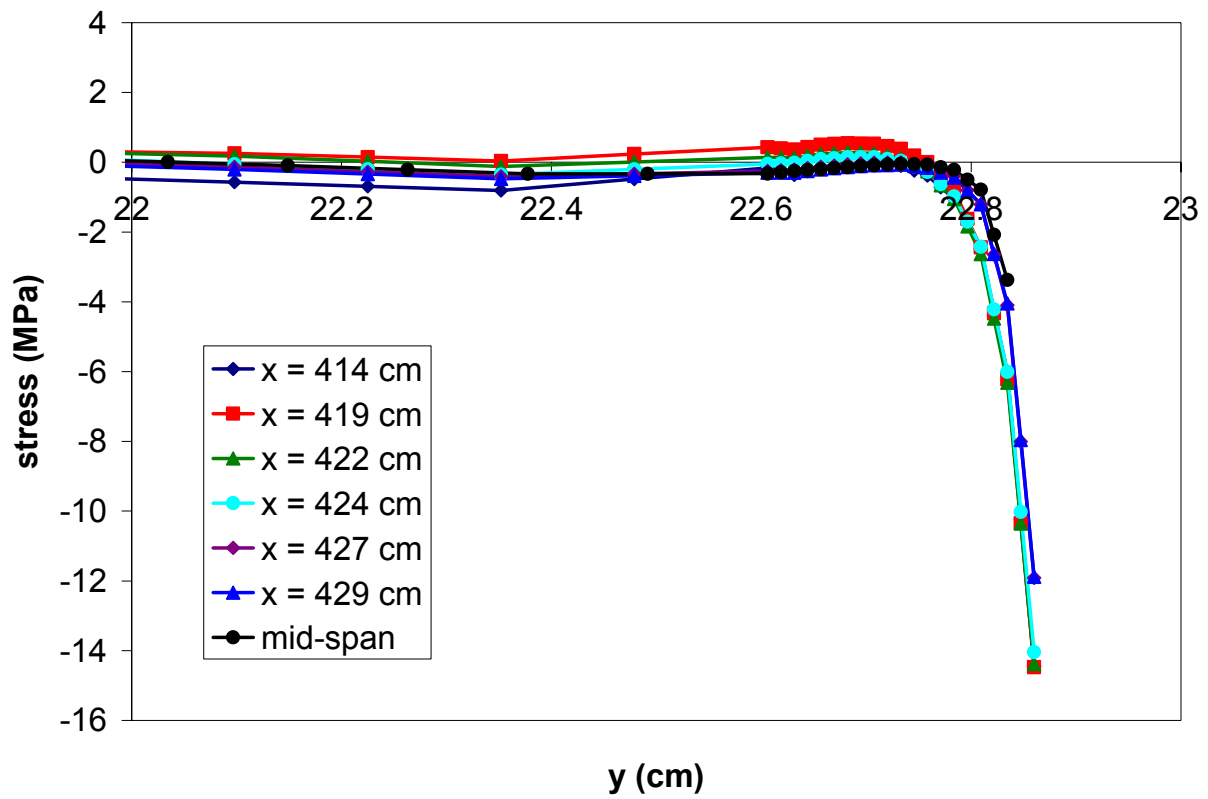


Figure 30. Interlaminar normal stress profiles across the width of at the primary carbon/glass interface in the vicinity of the free edge.

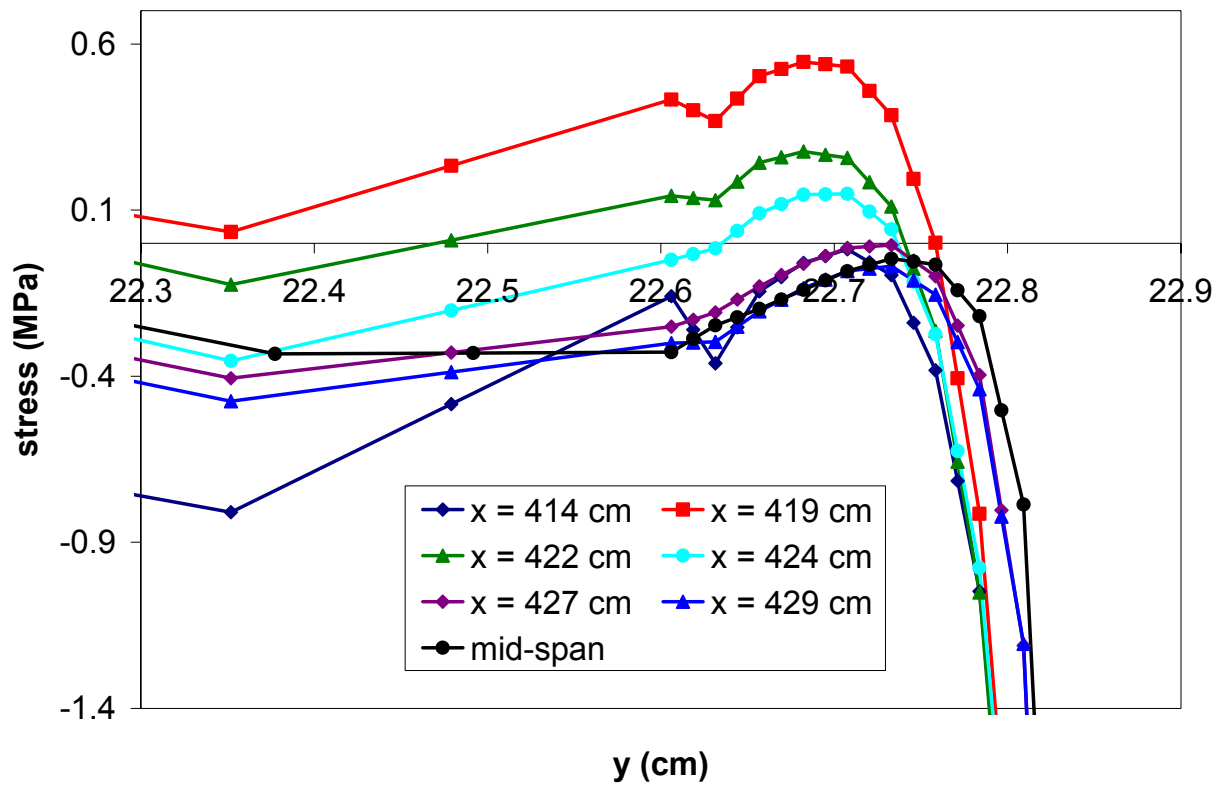


Figure 31. Close-up of free edge region in Figure 30.

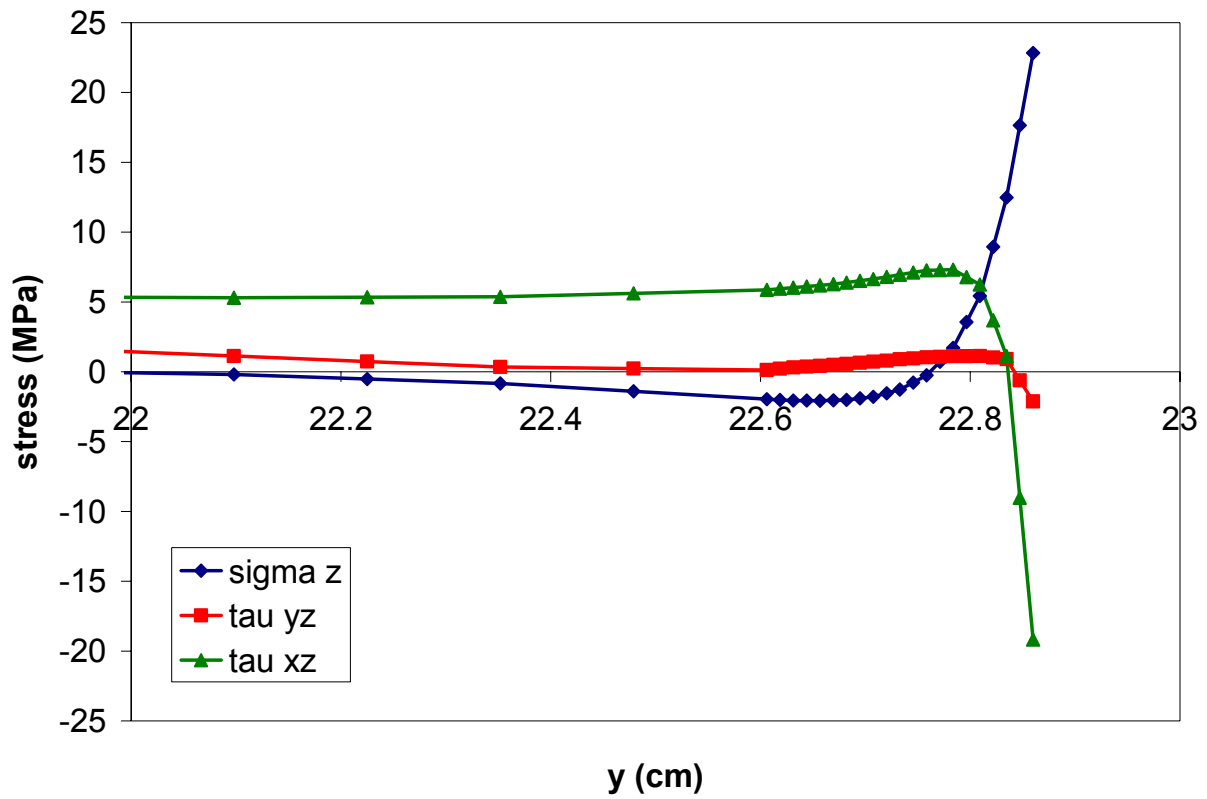


Figure 32. Free edge interlaminar stress profiles at the interface of  $\pm 45^\circ$  plies (445 kN,  $\Delta T = -114^\circ \text{C}$ ).

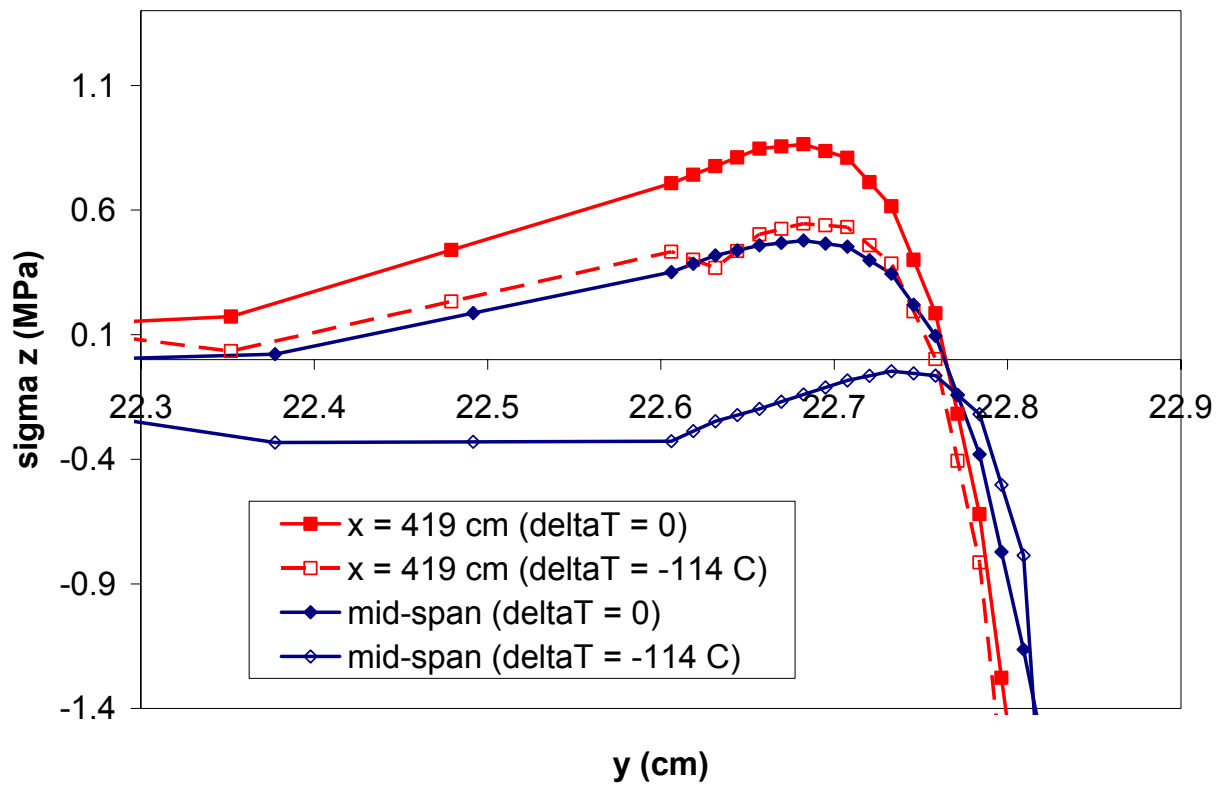


Figure 33. Comparison of the y-direction profiles for the free edge interlaminar tensile stress  $\sigma_z$  for  $\Delta T = -114^\circ\text{C}$  and  $\Delta T = 0$  at  $x = 419$  cm and at mid-span.

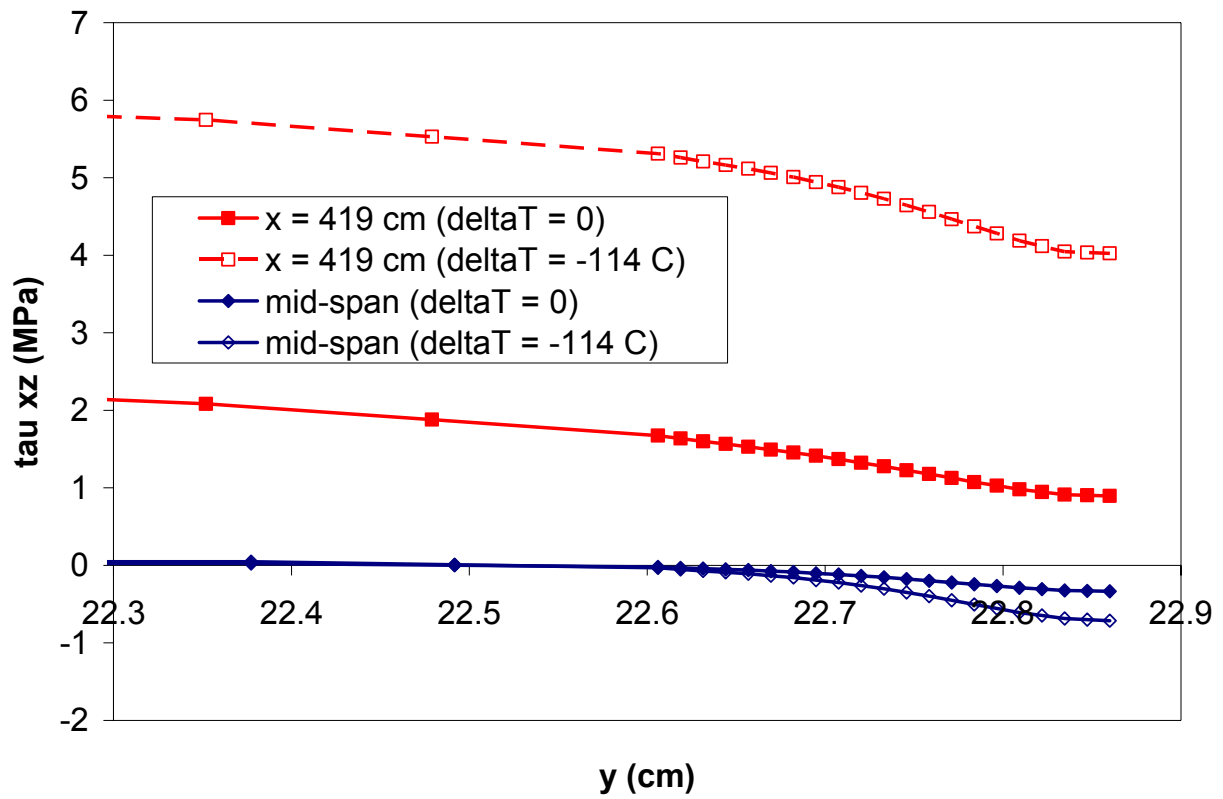


Figure 34. Comparison of y-direction profiles for the free edge interlaminar tensile stress  $\tau_{xz}$  for  $\Delta T = -205$  and  $\Delta T = 0$  at  $x = 165$  inches and mid-span.

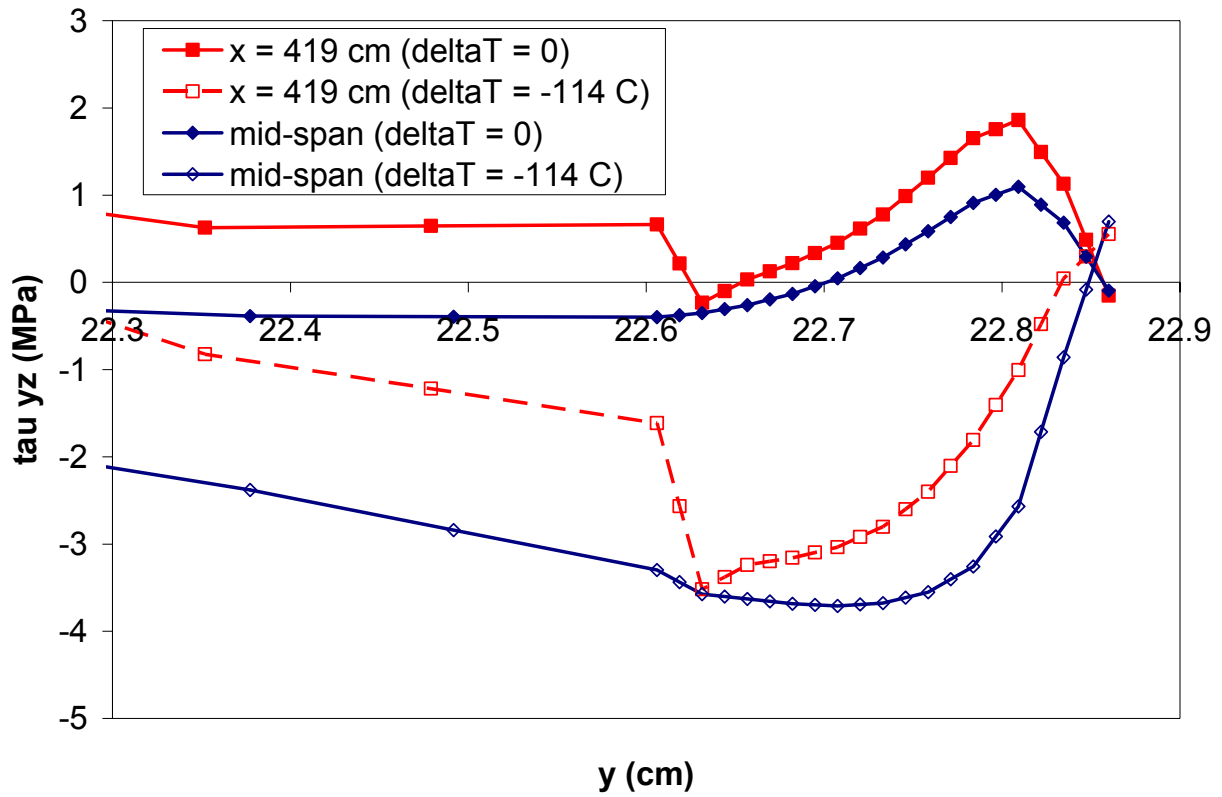


Figure 35. Comparison of the y-direction profiles for the interlaminar shear stresses  $\tau_{xz}$  and  $\tau_{yz}$  at the primary carbon/glass interface for  $\Delta T = -114\text{ }^{\circ}\text{C}$  and  $\Delta T = 0$  at  $x = 419\text{ cm}$ .

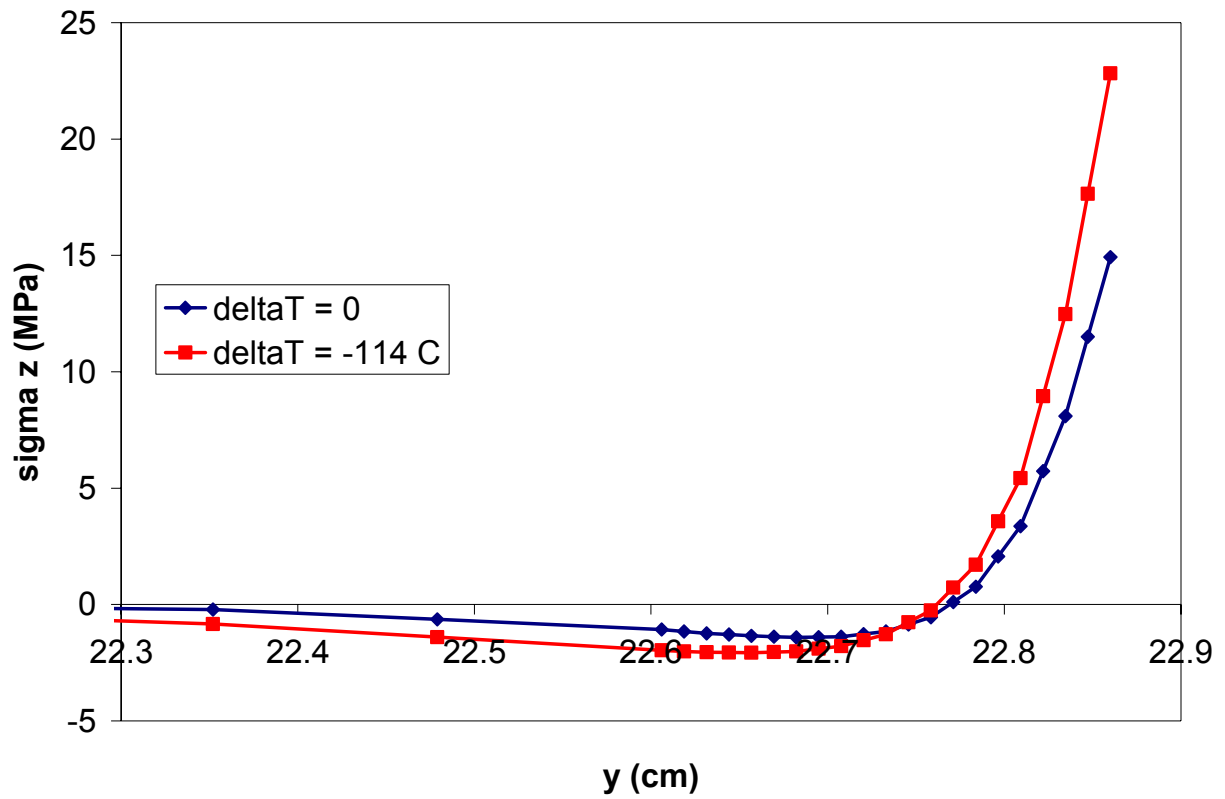


Figure 36. Effect of  $\Delta T$  on the free edge  $\sigma_z$  profile at the interface between the glass  $\pm 45^\circ$  plies.

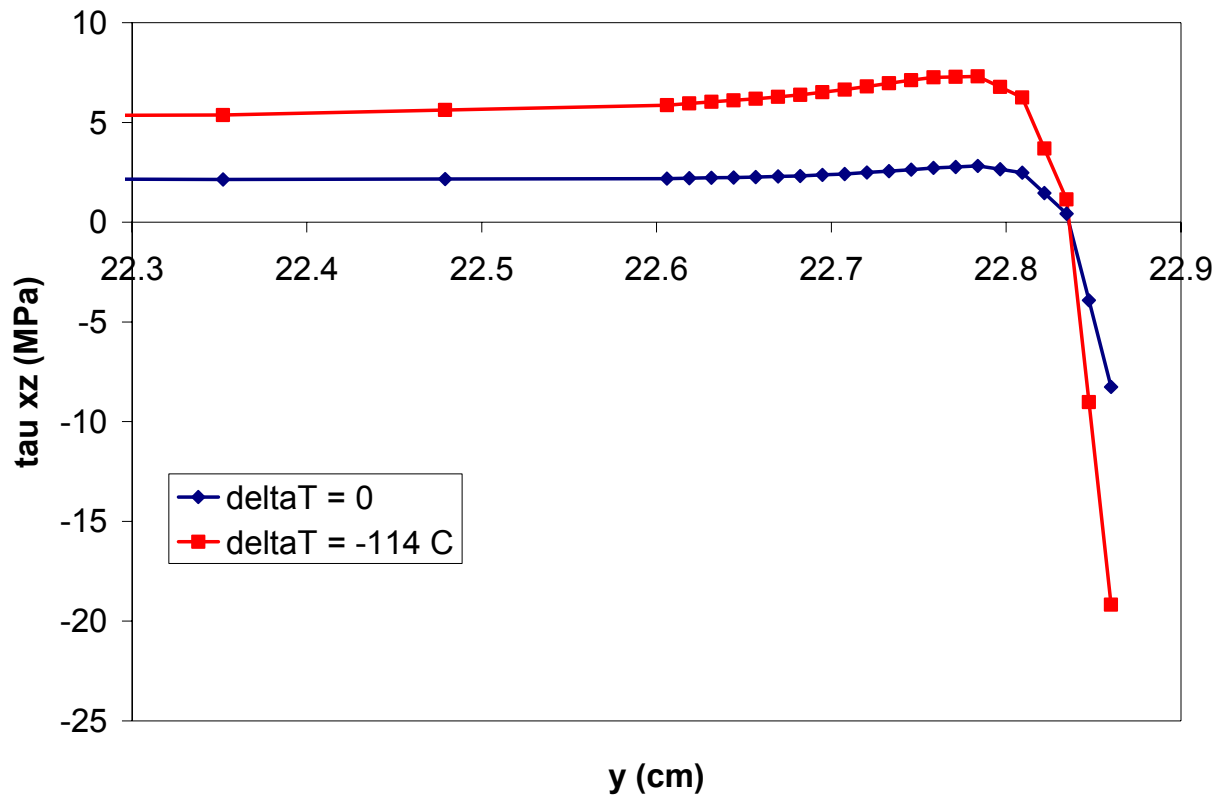


Figure 37. Effect of  $\Delta T$  on the free edge  $\tau_{xz}$  profile at the interface between the glass  $\pm 45^\circ$  plies.

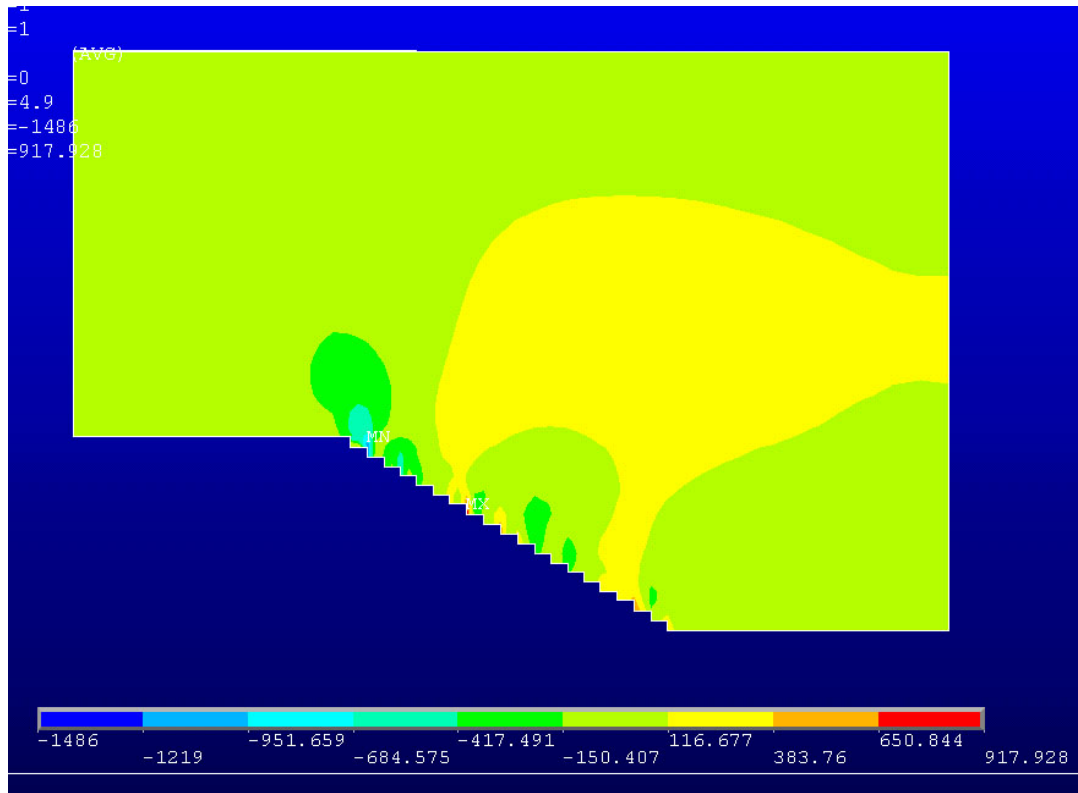


Figure 38. Contour plot of interlaminar normal stress  $\sigma_z$  in the flange taper region.

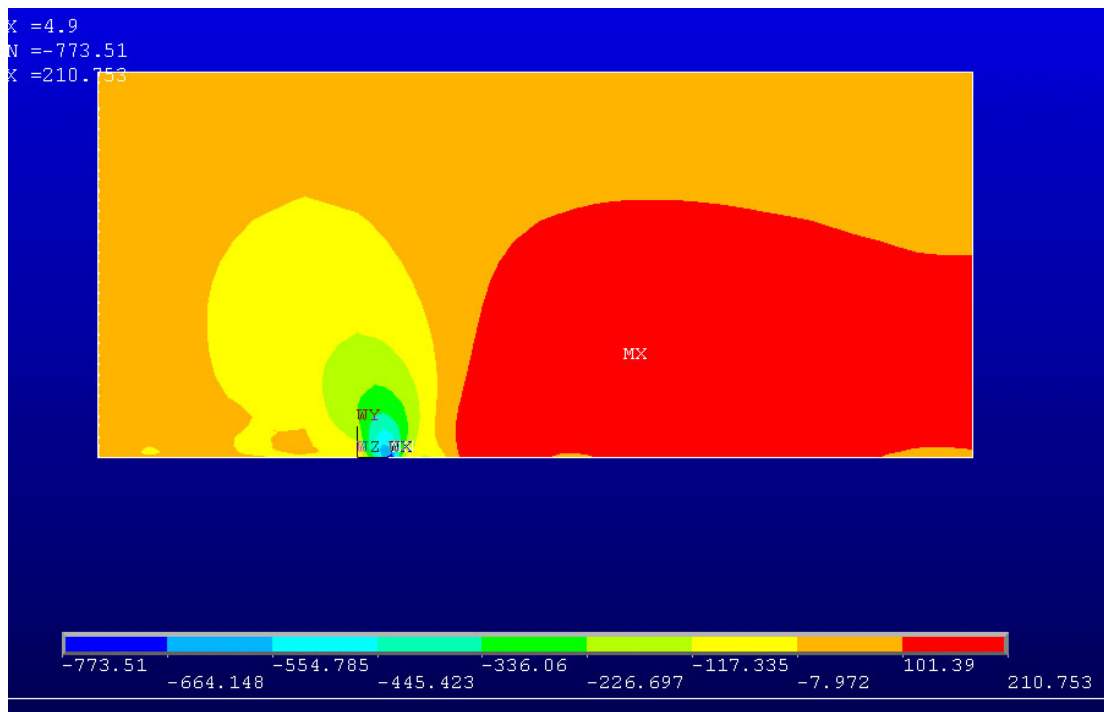


Figure 39. Contour plot of interlaminar normal stress  $\sigma_z$  in the flange taper region (outer carbon/CSM sublaminates only shown).

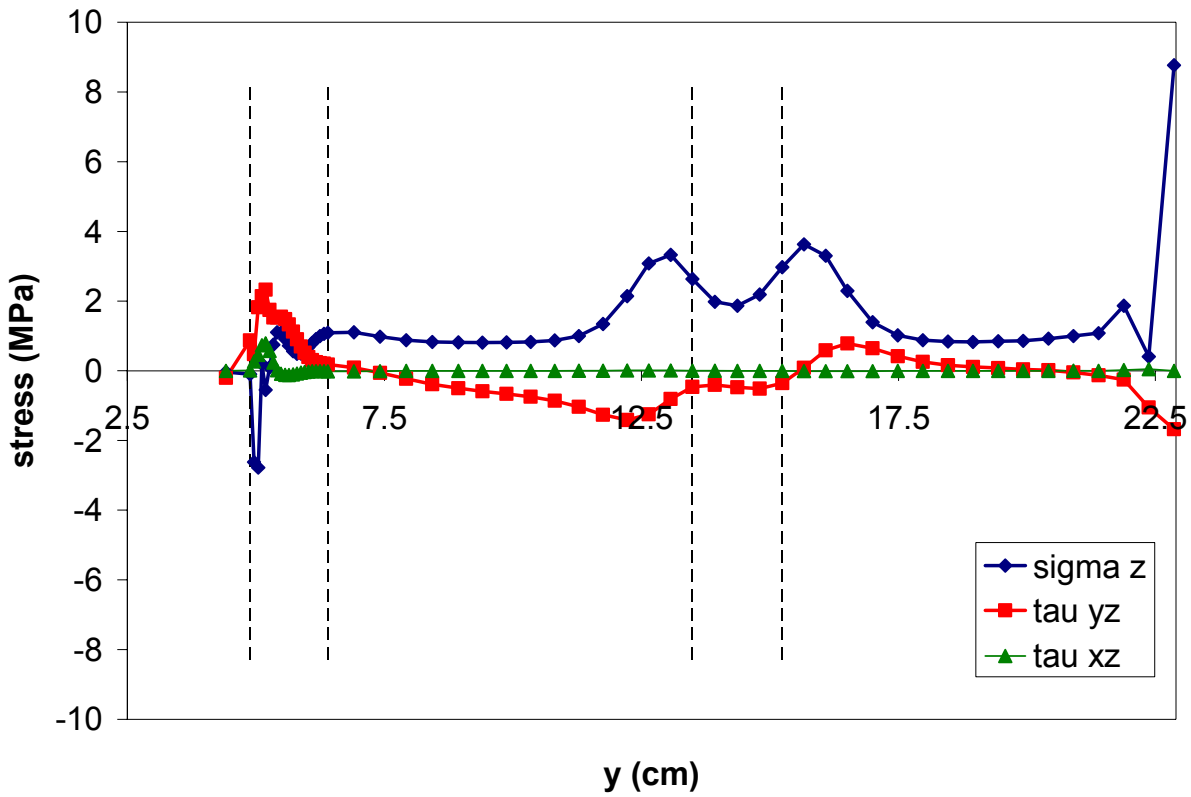
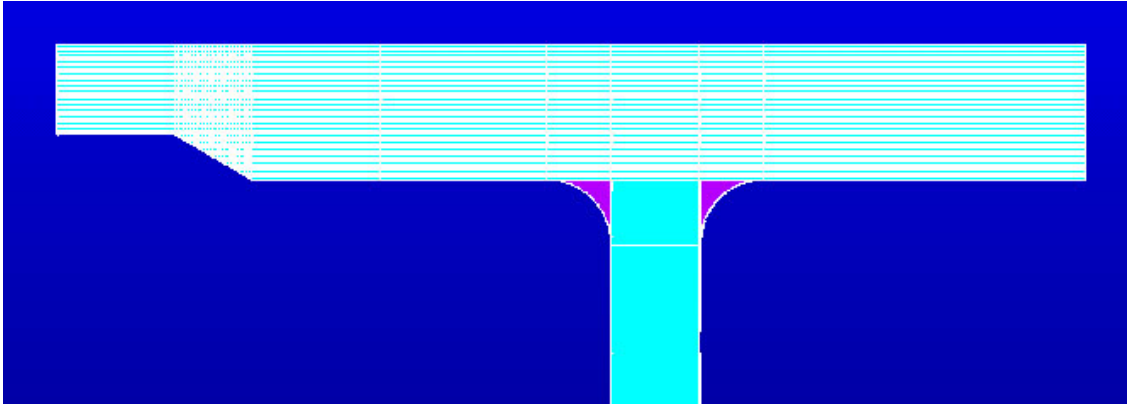


Figure 40. Interlaminar stress profiles at the primary carbon/glass interface across the width of TAPERSUB2 at MID-SPAN (dashed lines correspond to the taper and web coordinates, as shown in the schematic above).

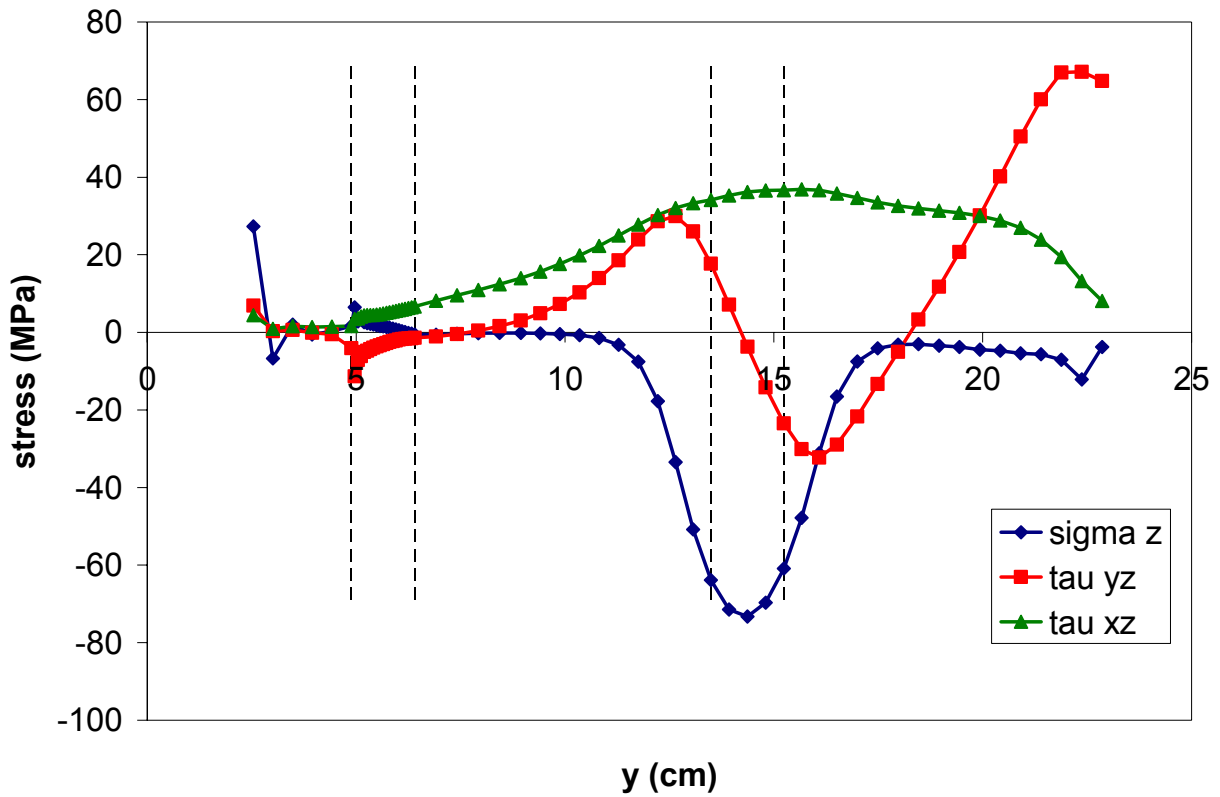
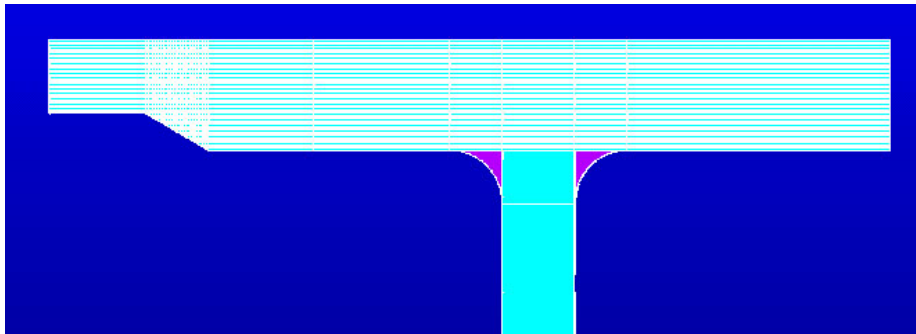


Figure 41. Interlaminar stress profiles at the primary carbon/glass interface across the width of TAPERSUB2 near a LOAD PATCH ( $x = 424$  cm or 167.5 inches).

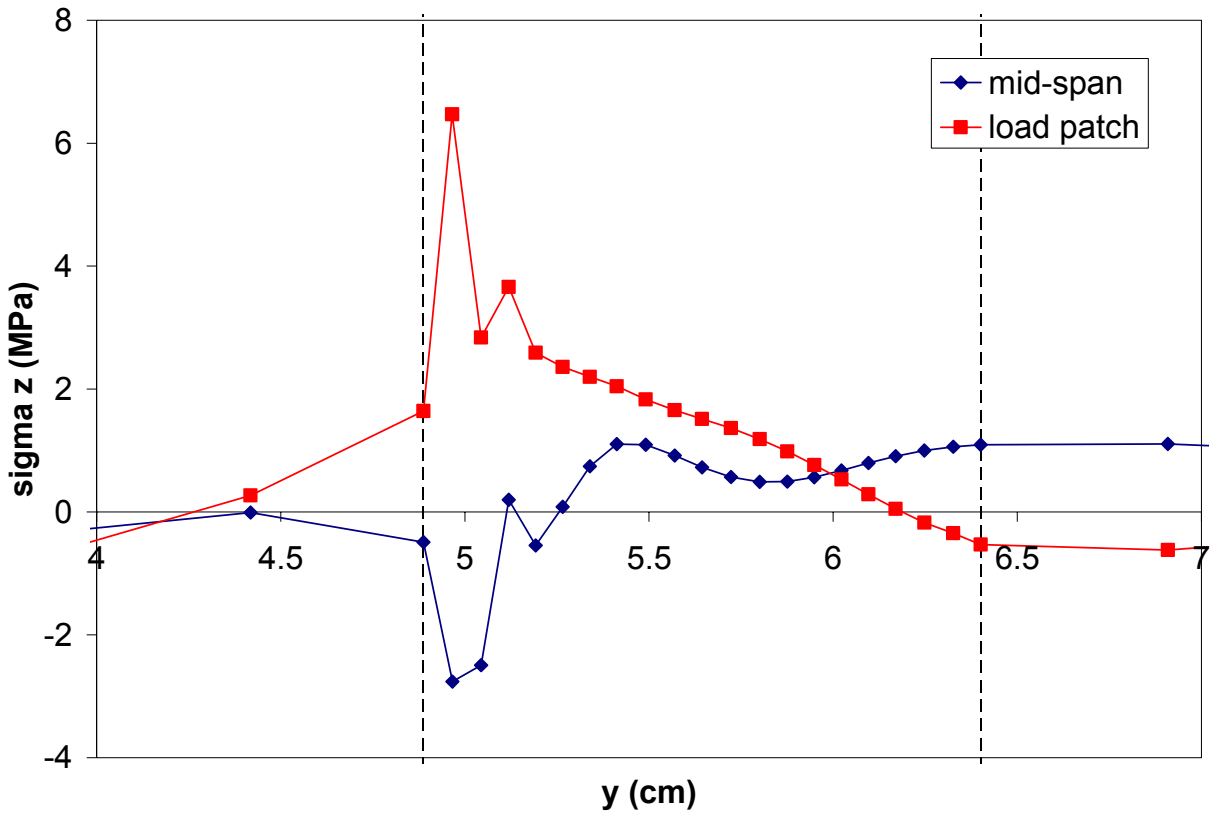
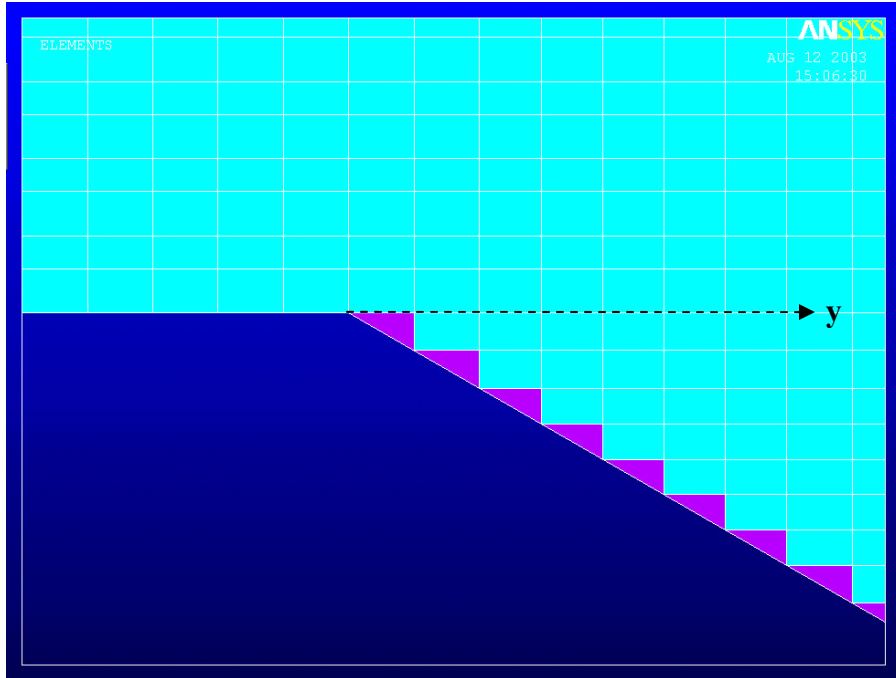


Figure 42. Comparison of the interlaminar normal stress  $\sigma_z$  along the primary carbon/glass interface at the taper tip at the mid-span and load patch ( $x = 424$  cm or 166.75 inches) locations.

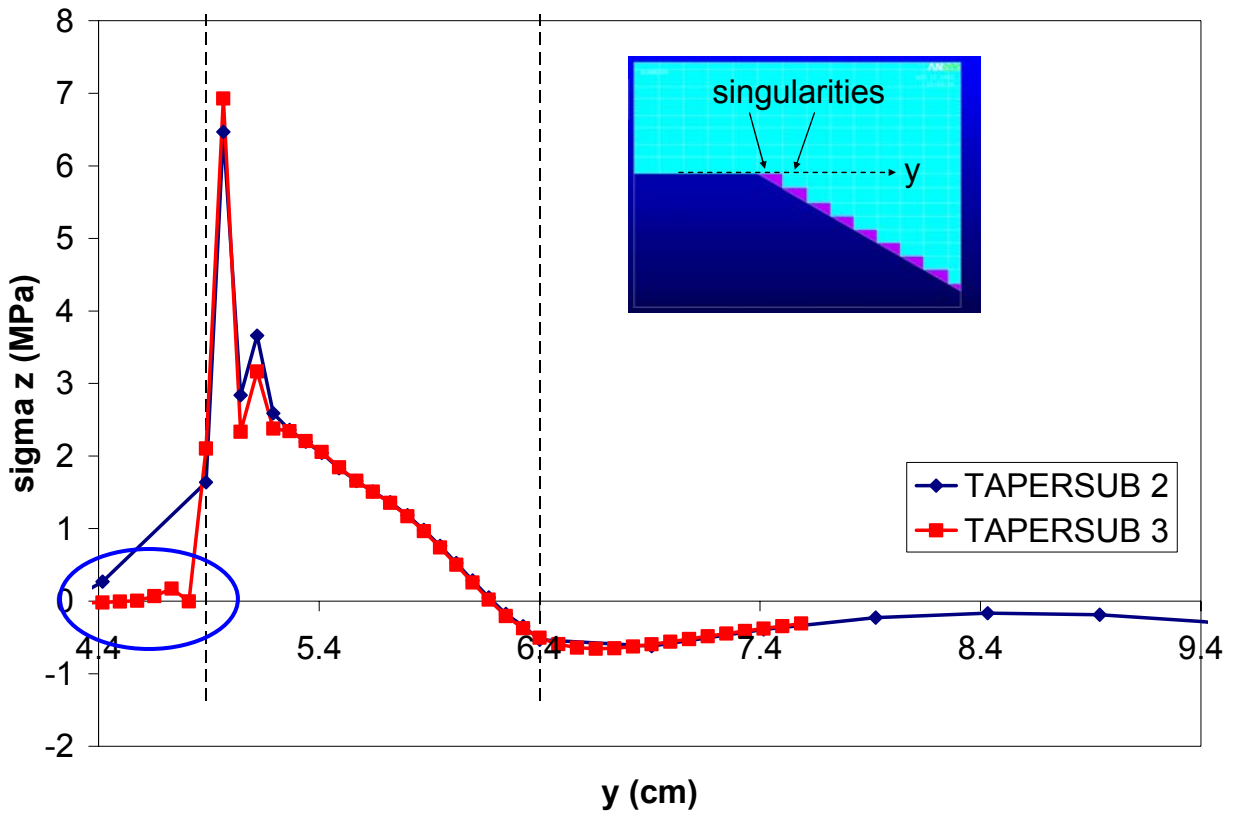


Figure 43. Interlaminar normal stress profile at the primary carbon/glass interface in the vicinity of the taper near the load patch ( $x = 424$  cm or 166.75 inches).

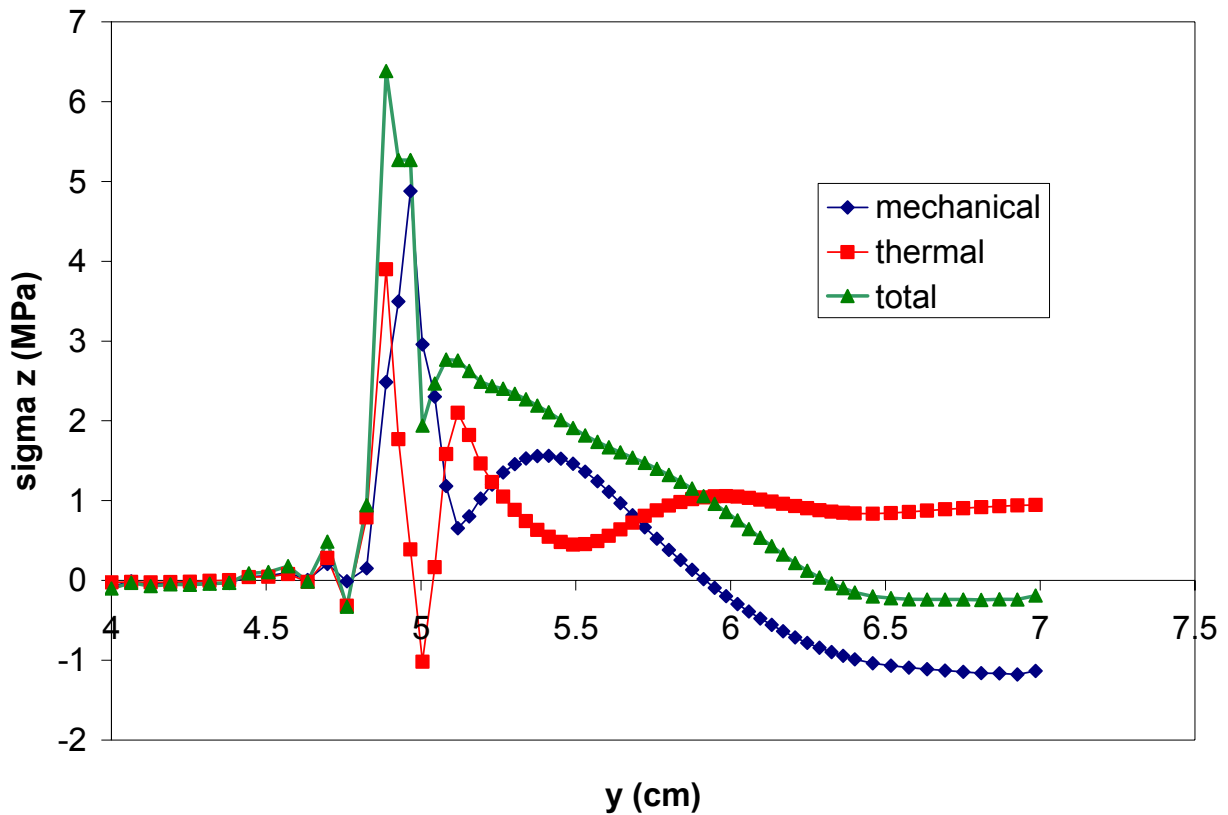
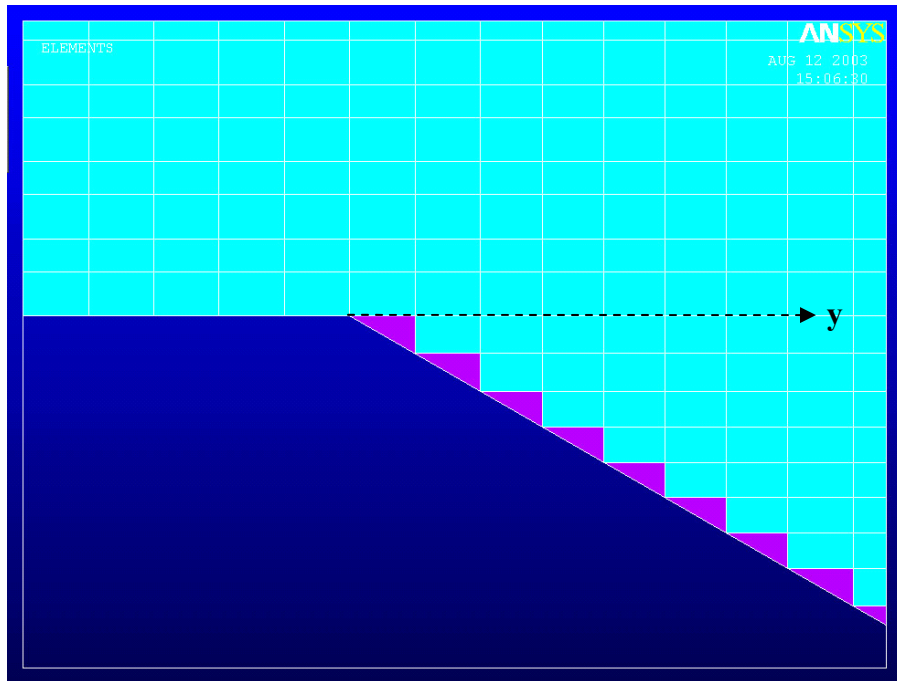


Figure 44. Mechanical (444 kN or 100 kips) and thermal ( $\Delta T = -114\text{ }^{\circ}\text{C}$  or  $-205\text{ }^{\circ}\text{F}$ ) components of the interlaminar normal stress at the primary carbon/glass interface in the vicinity of the taper at the load patch.

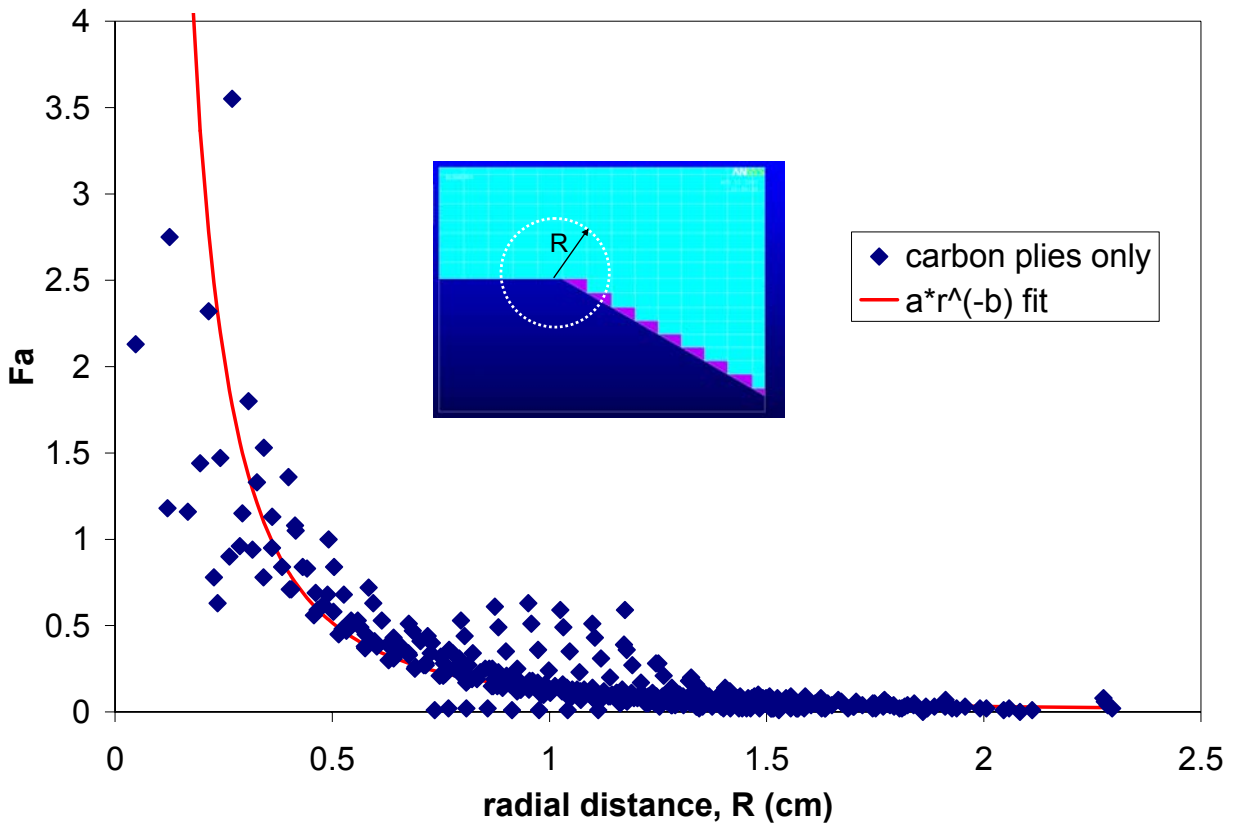


Figure 45.  $F_a$  in carbon plies in the taper region as a function of distance from the free edge of the taper (444 kN or 100 kips load per patch and  $\Delta T = -114\text{ }^\circ\text{C}$  or  $-205\text{ }^\circ\text{F}$ ).

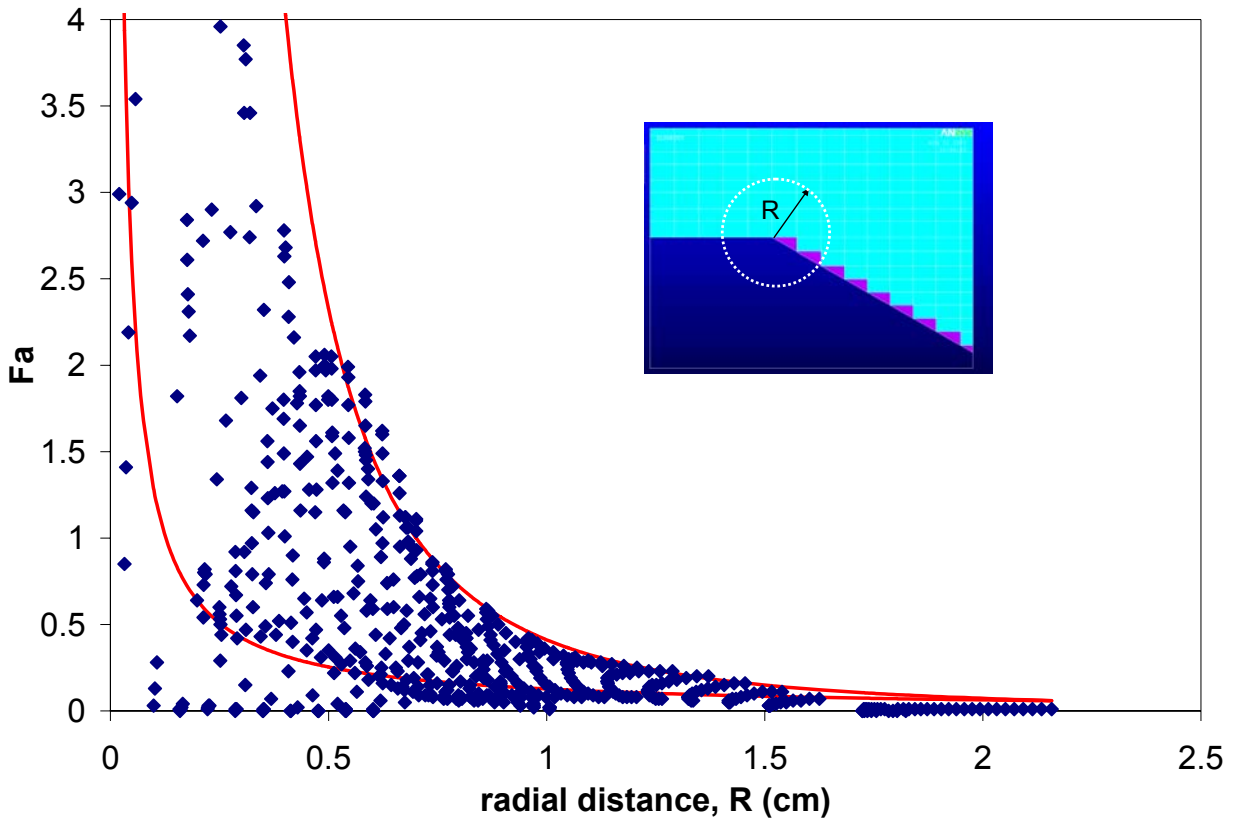


Figure 46. Fa in carbon plies in the taper region as a function of distance from the free edge of the taper (thermal loading only:  $\Delta T = -114\text{ }^{\circ}\text{C}$  or  $-205\text{ }^{\circ}\text{F}$ ).

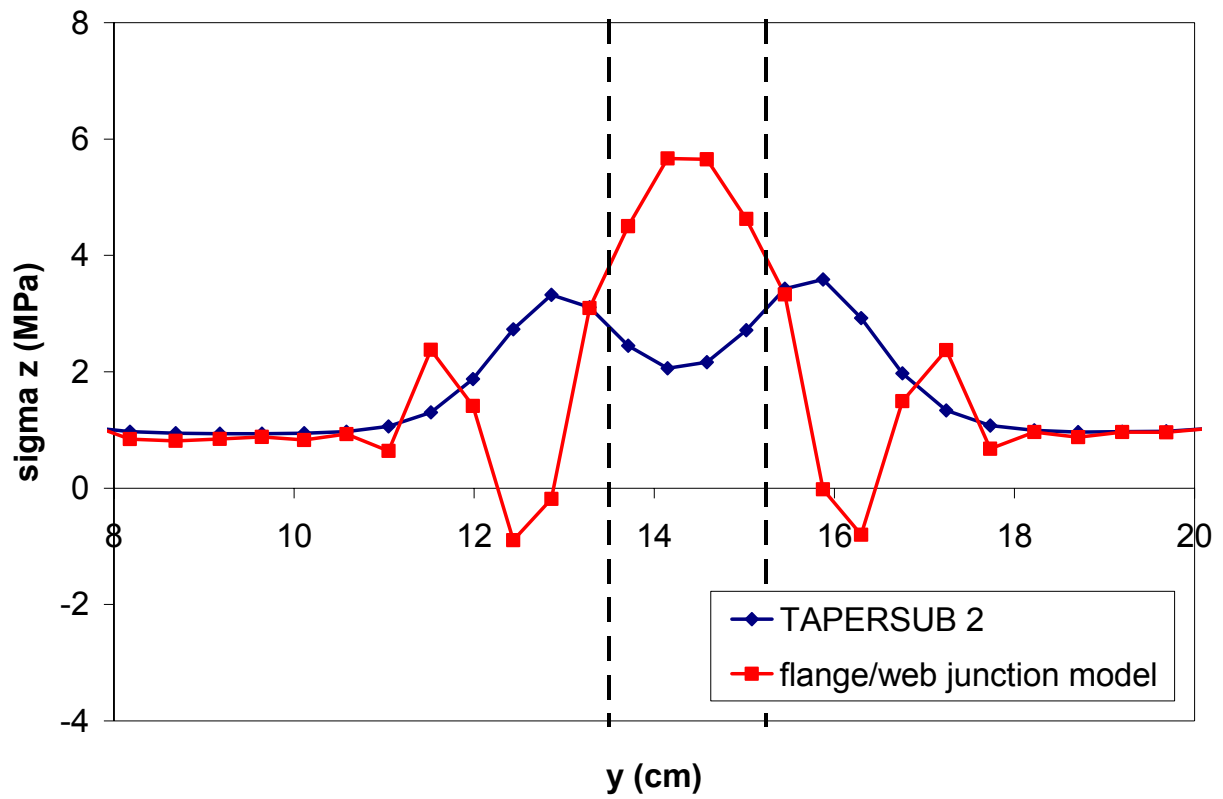


Figure 47. Comparison of detailed flange/web junction model with TAPERSUB 2 results:  $\sigma_z$  at mid-span.

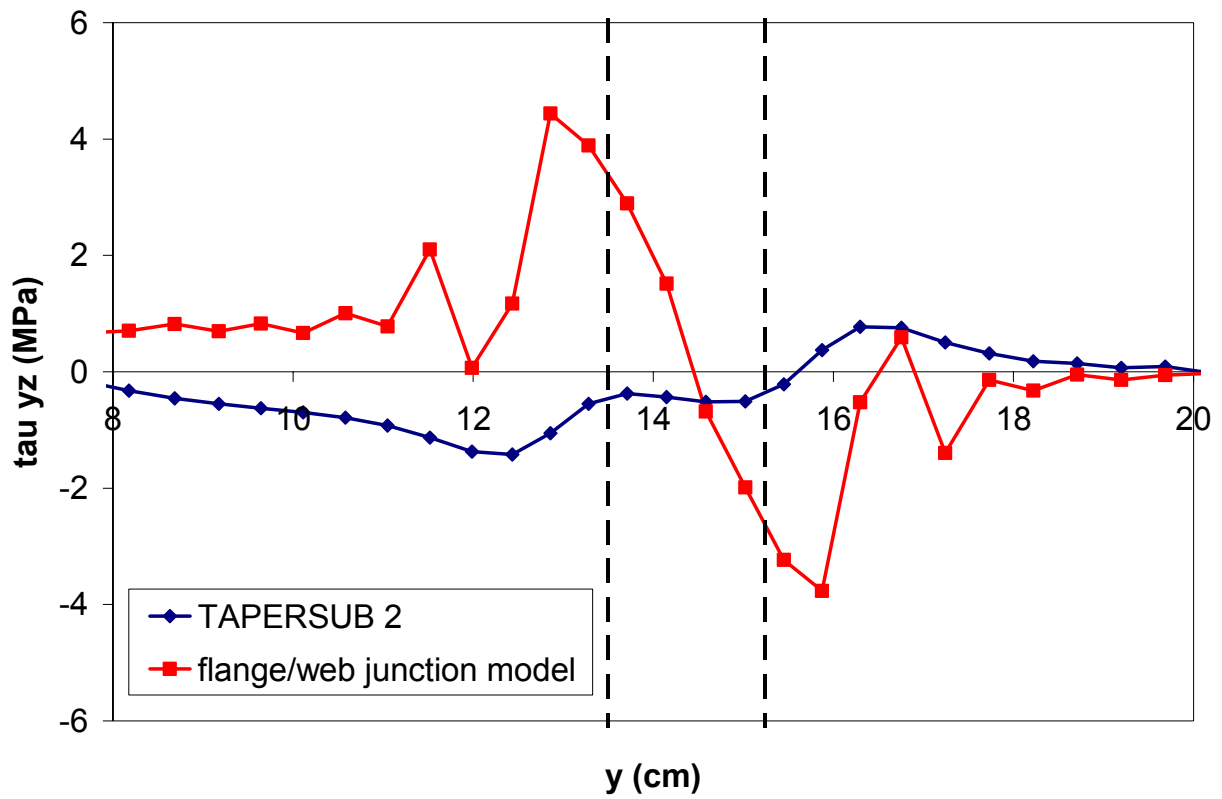


Figure 48. Comparison of detailed flange/web junction model with TAPERSUB 2 results:  $\tau_{yz}$  at mid-span.

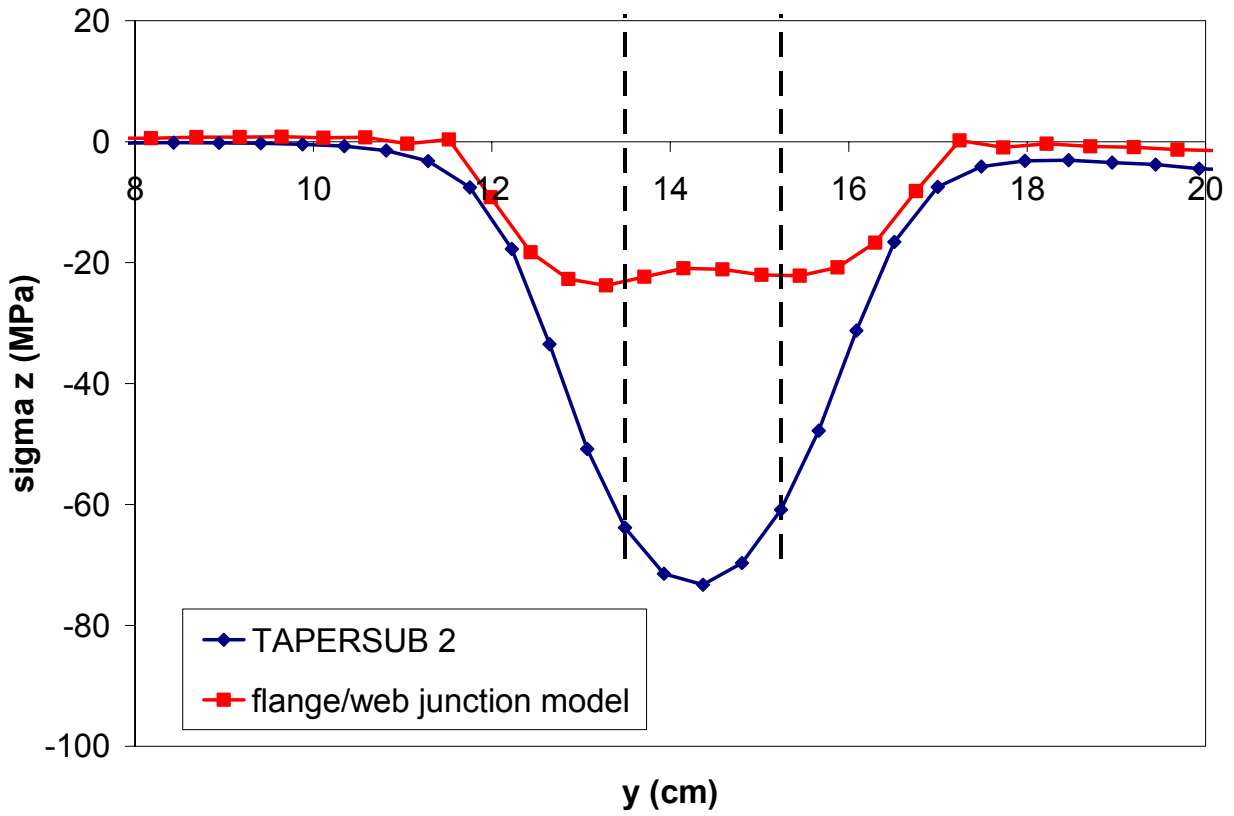


Figure 49. Comparison of detailed flange/web junction model with TAPERSUB 2 results:  $\sigma_z$  near the load patch ( $x = 424$  cm or 166.75 inches).

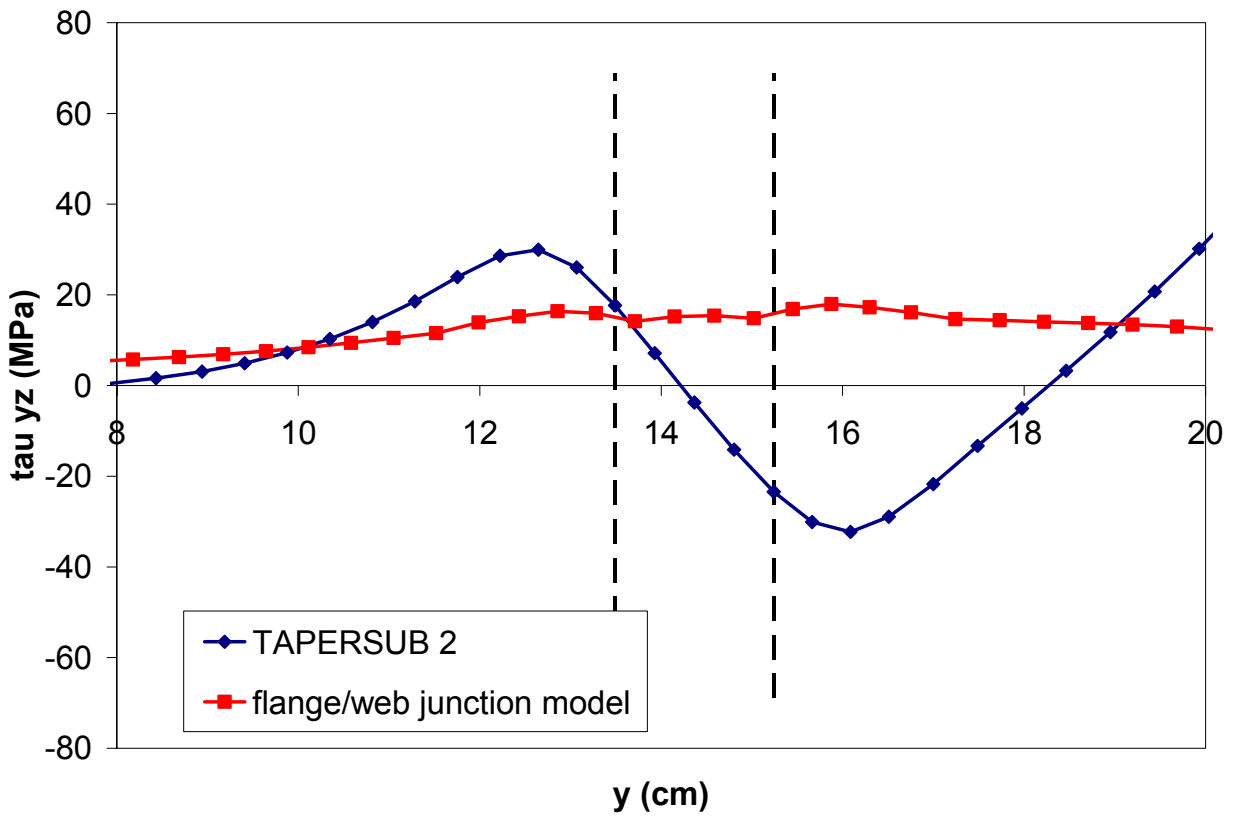


Figure 50. Comparison of detailed flange/web junction model with TAPERSUB 2 results:  $\tau_{yz}$  near the load patch ( $x = 424$  cm or 166.75 inches).

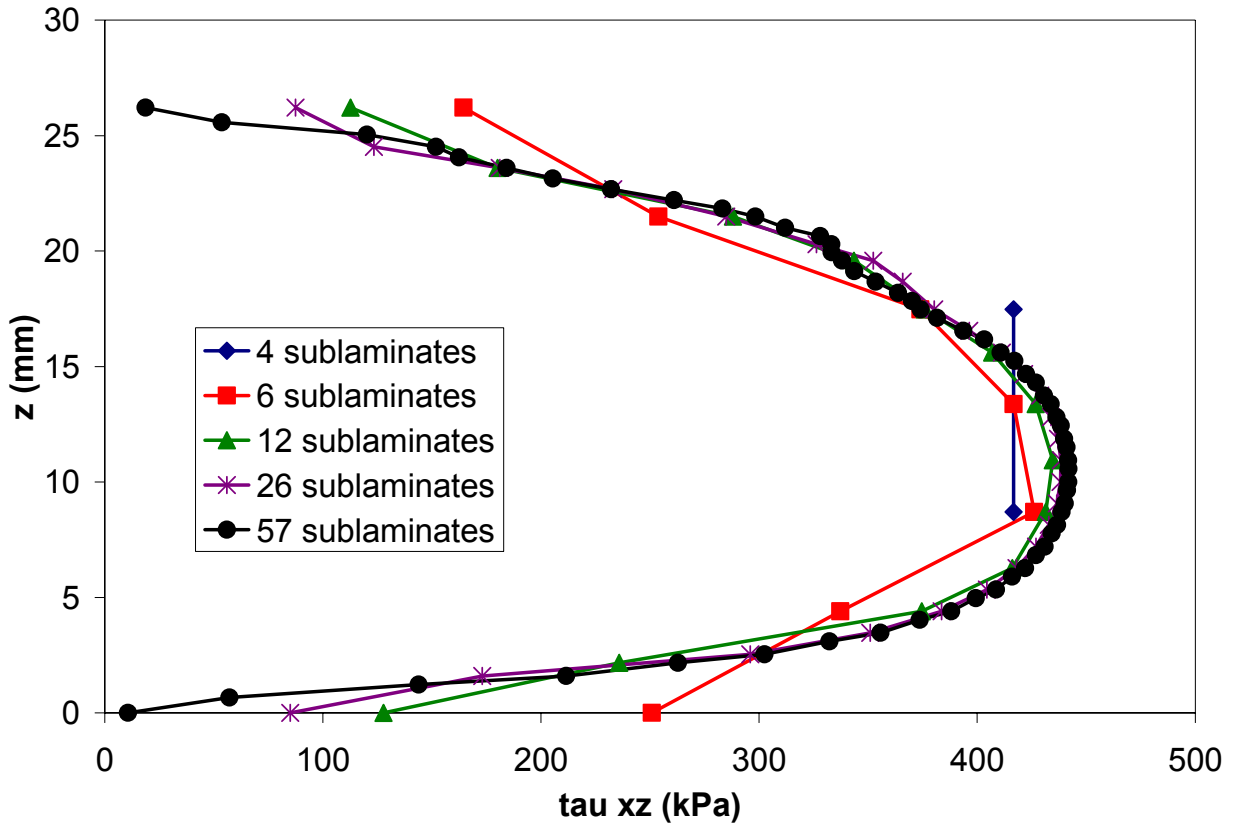


Figure 51. Effect of sub-laminate refinement on the interlaminar shear stresses at the third-point in the SBS flange specimen.

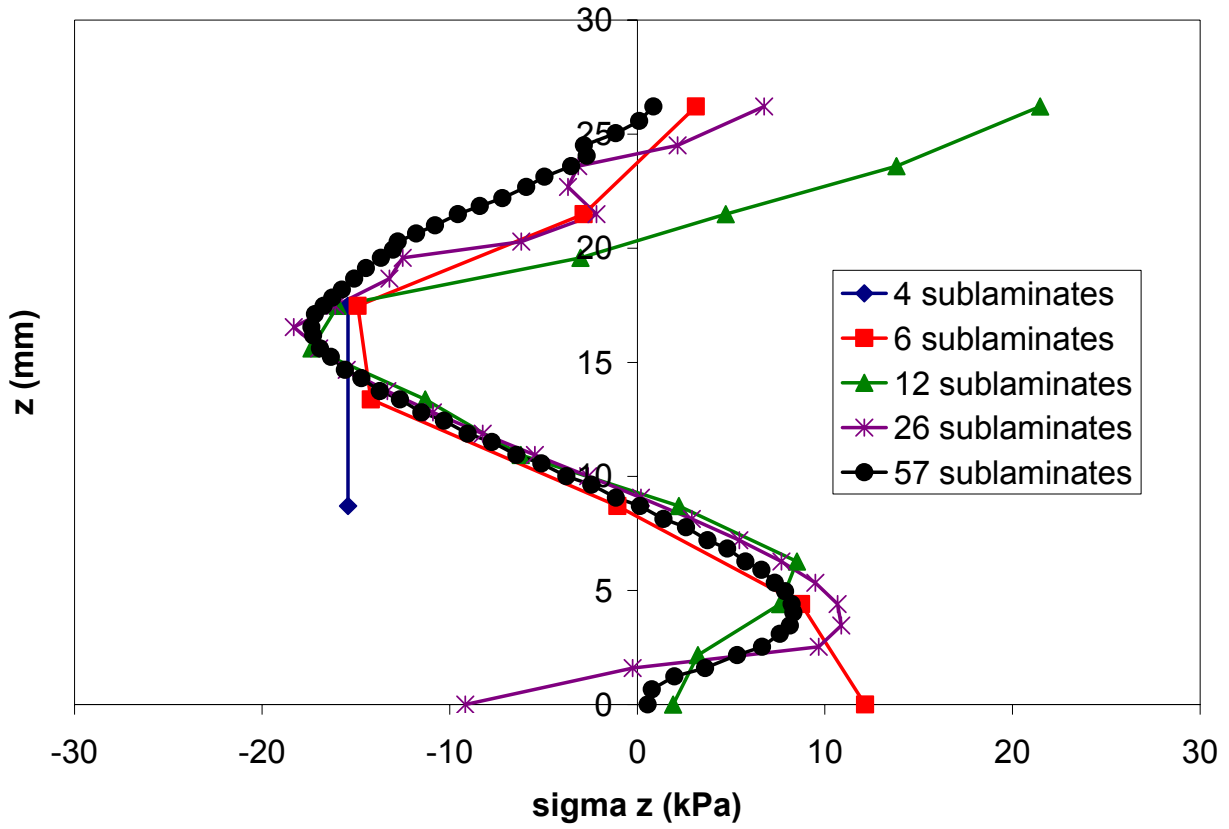


Figure 52. Effect of sub-laminate refinement on the interlaminar normal stresses at the third-point in the SBS flange specimen.

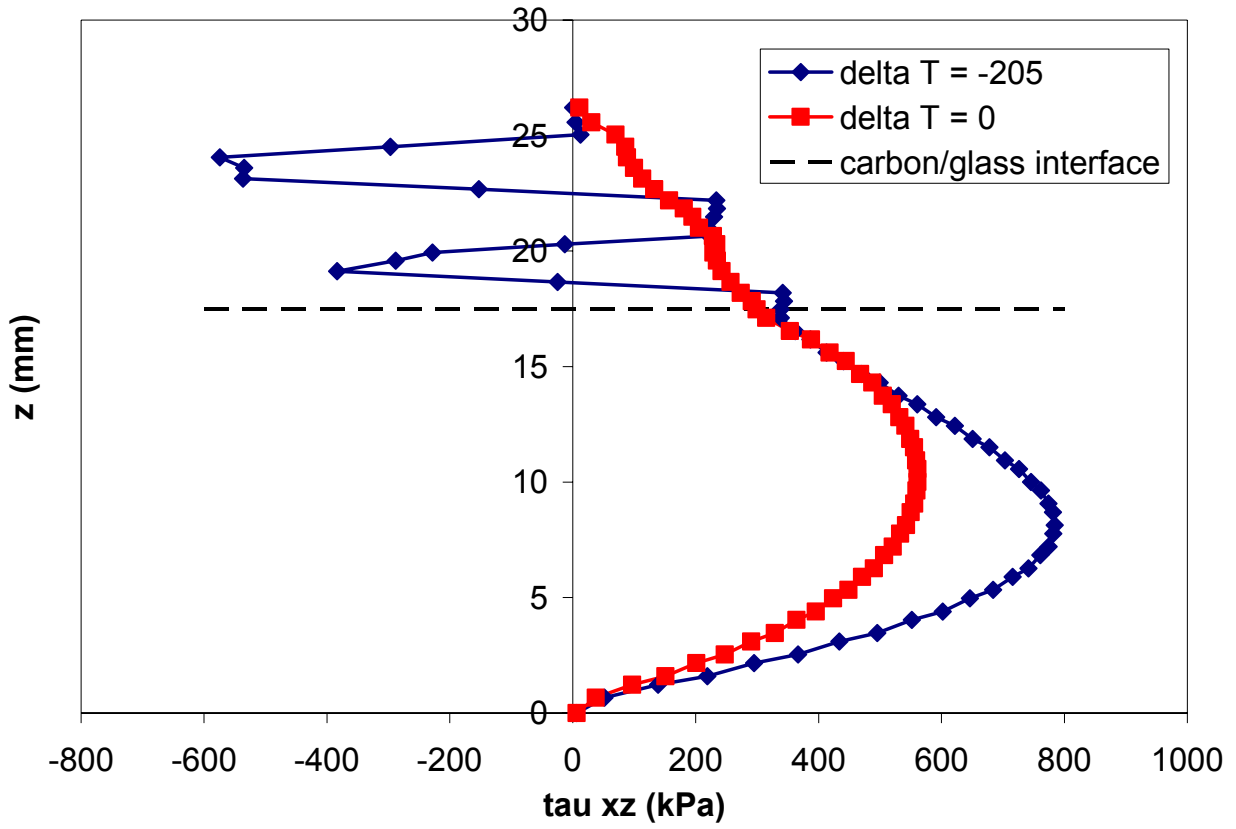


Figure 53. Effect of thermal change on the distribution of the interlaminar shear stress through the flange thickness in the SBS test (at  $x = L/3$ ).

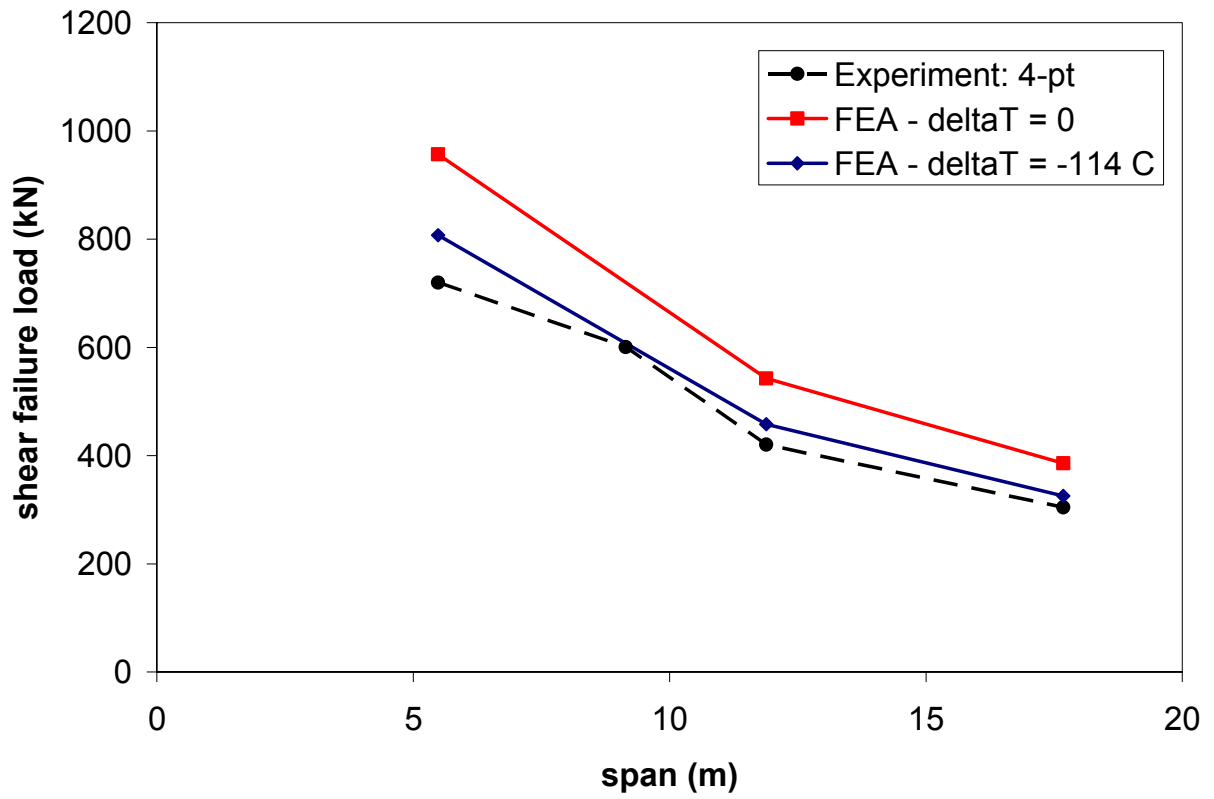


Figure 54. Comparison of the predicted shear capacity vs. span length for the compressive failure mode and the experimental results.

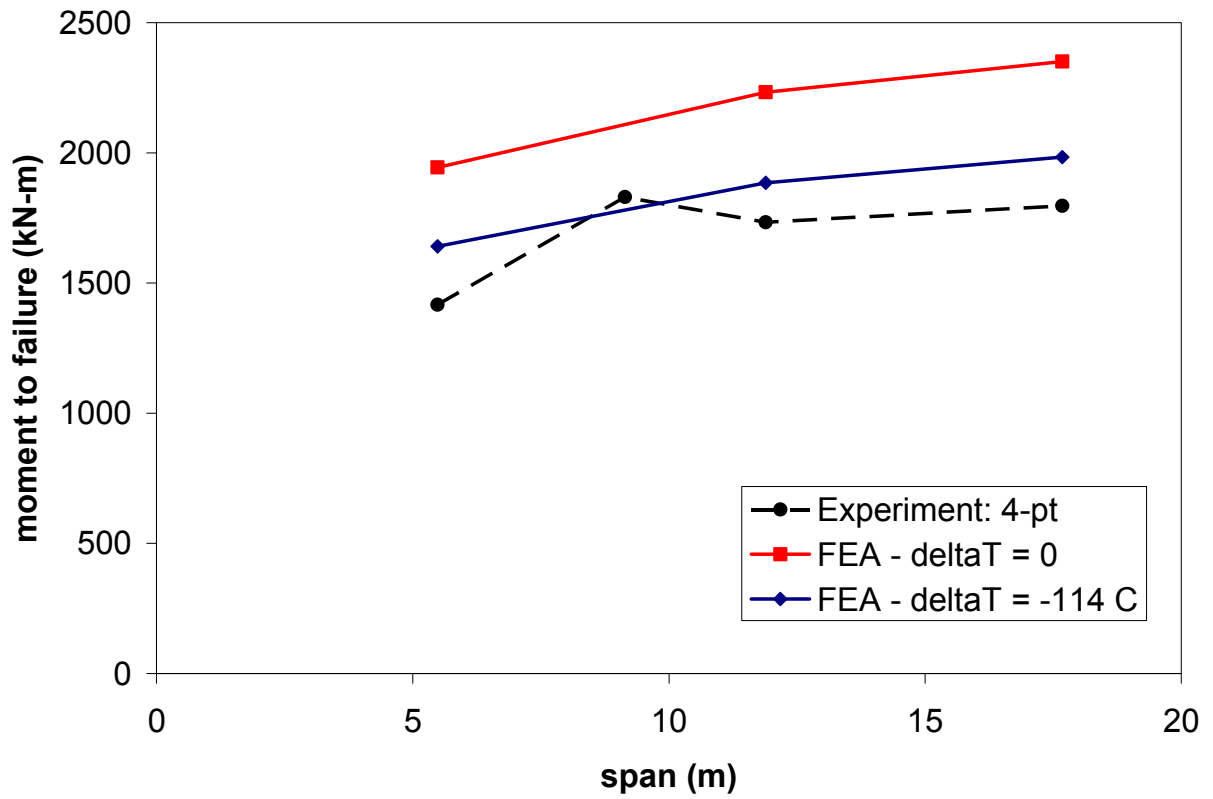


Figure 55. Comparison of the predicted moment capacity vs. span length for the compressive failure mode and the experimental results.

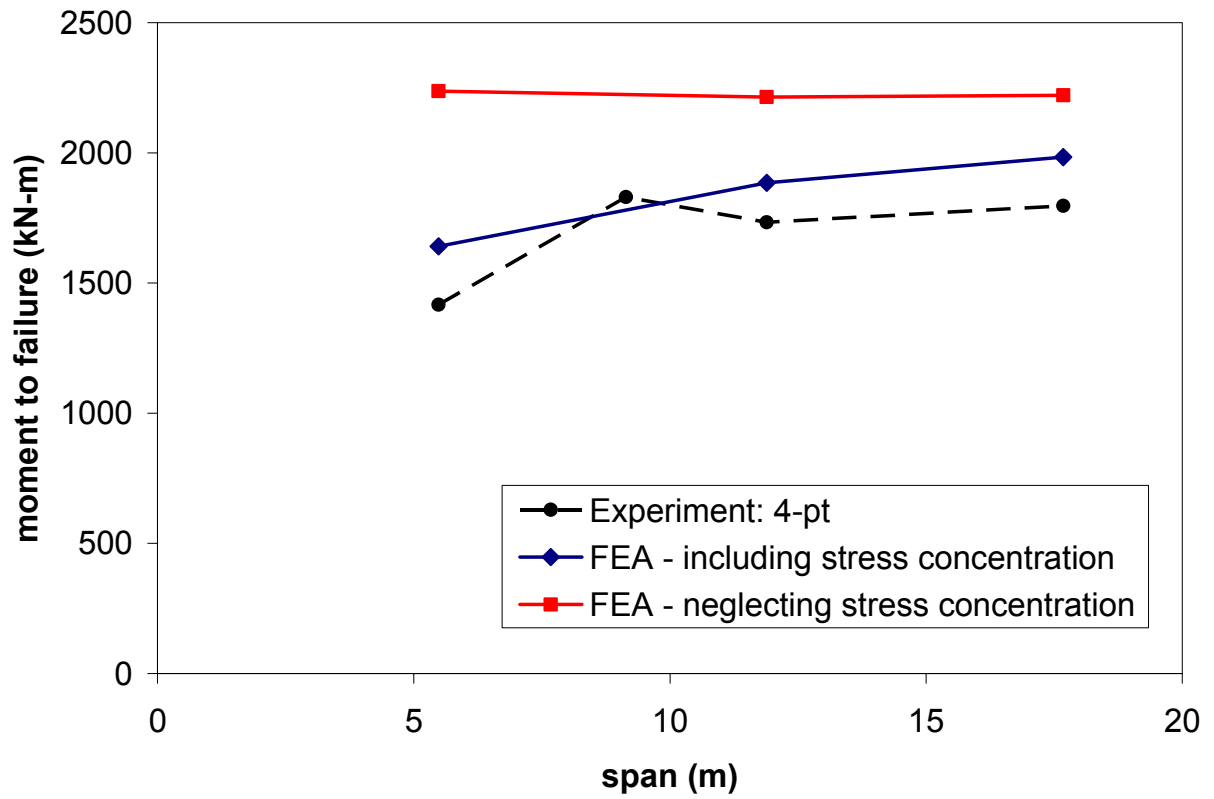


Figure 56. Effect of stress concentration on moment to failure.

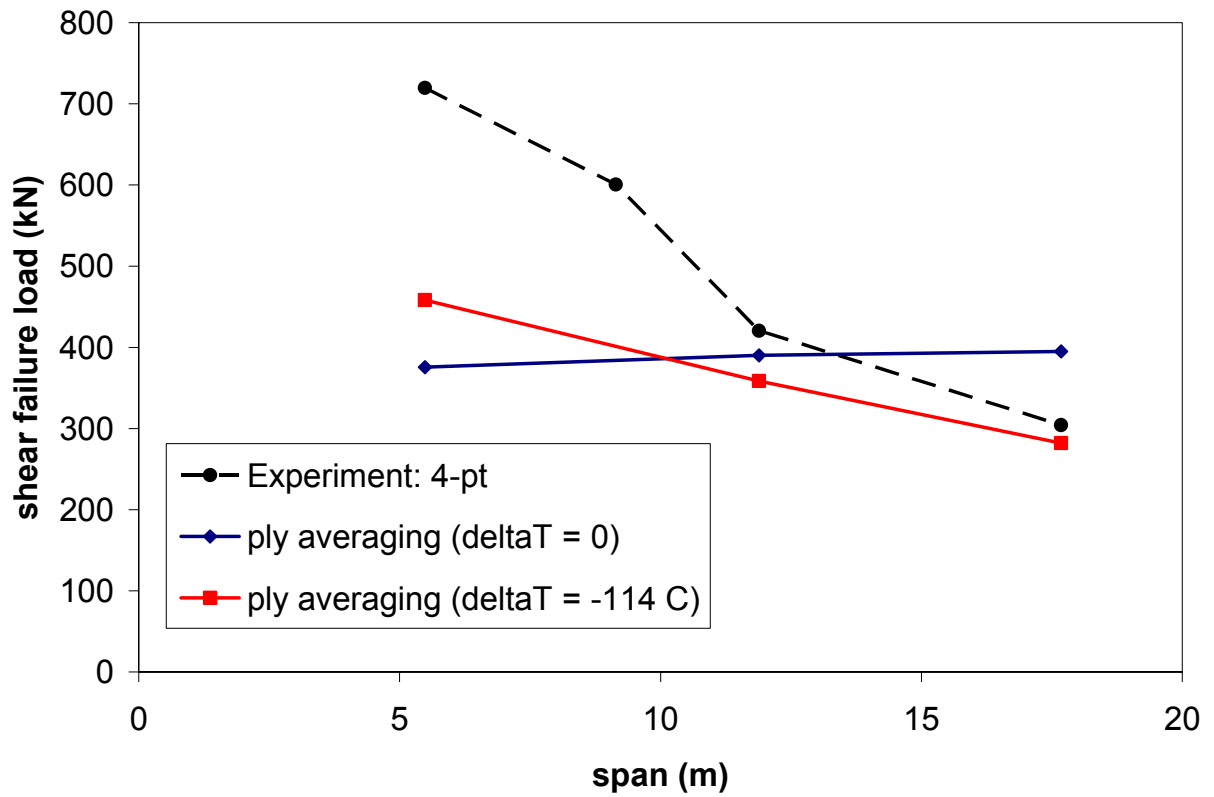


Figure 57. Comparison of the predicted shear capacity vs. span length for the taper edge delamination failure mode using the ply width stress averaging technique and the experimental results.

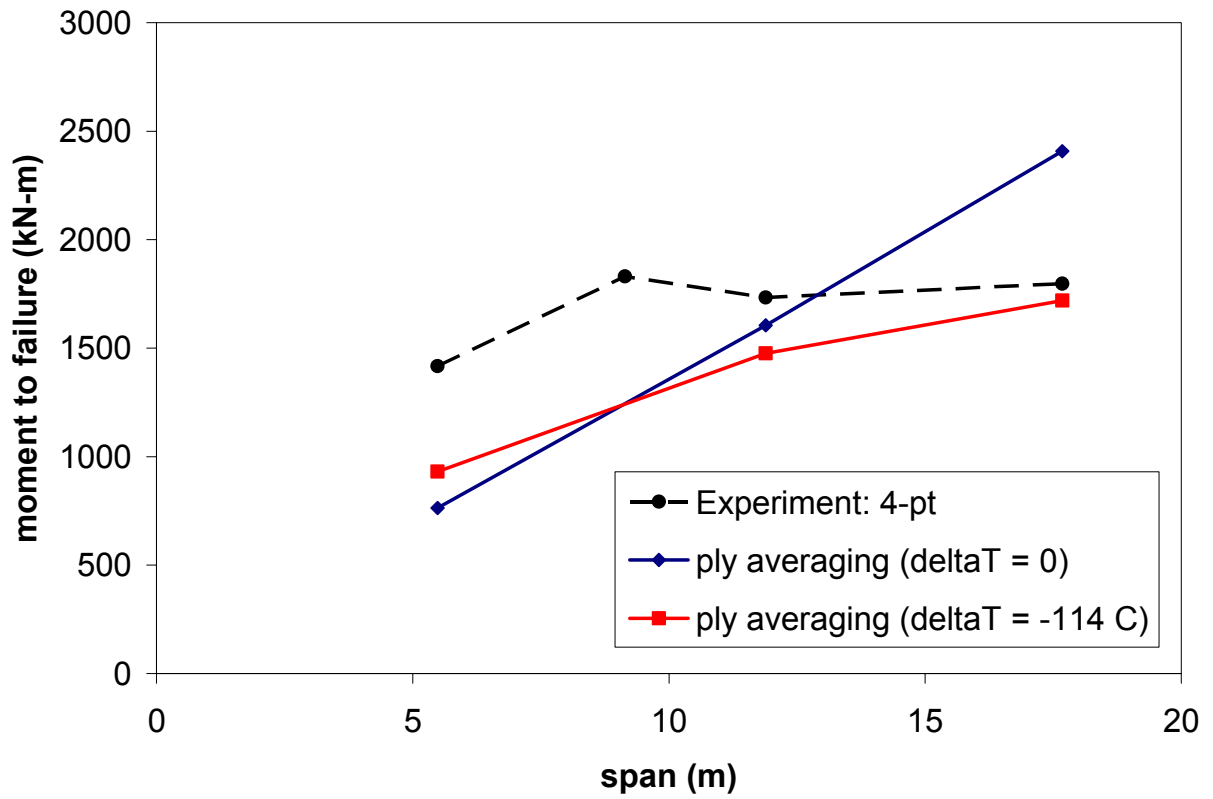


Figure 58. Comparison of the predicted moment capacity vs. span length for the taper edge delamination failure mode using the ply width stress averaging technique and the experimental results.

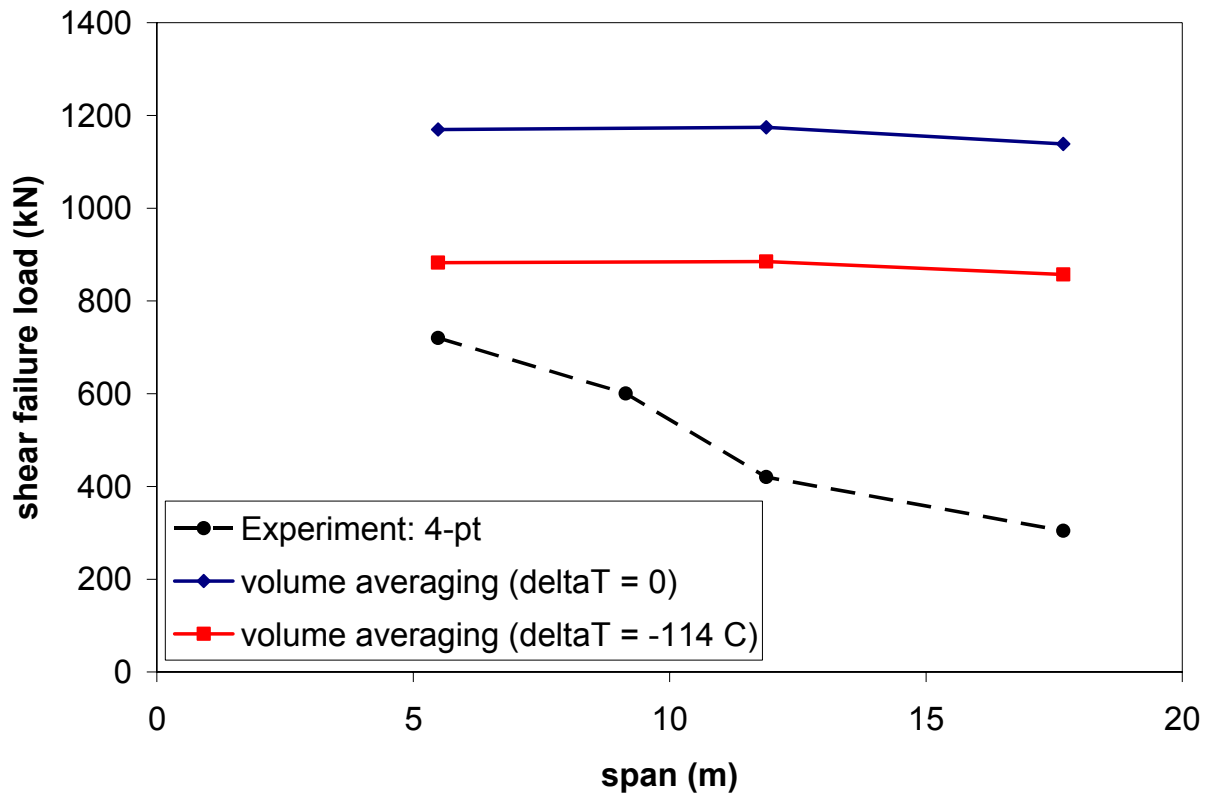


Figure 59. Comparison of the predicted shear capacity vs. span length for the taper edge delamination failure mode using the volume stress averaging technique and the experimental results.

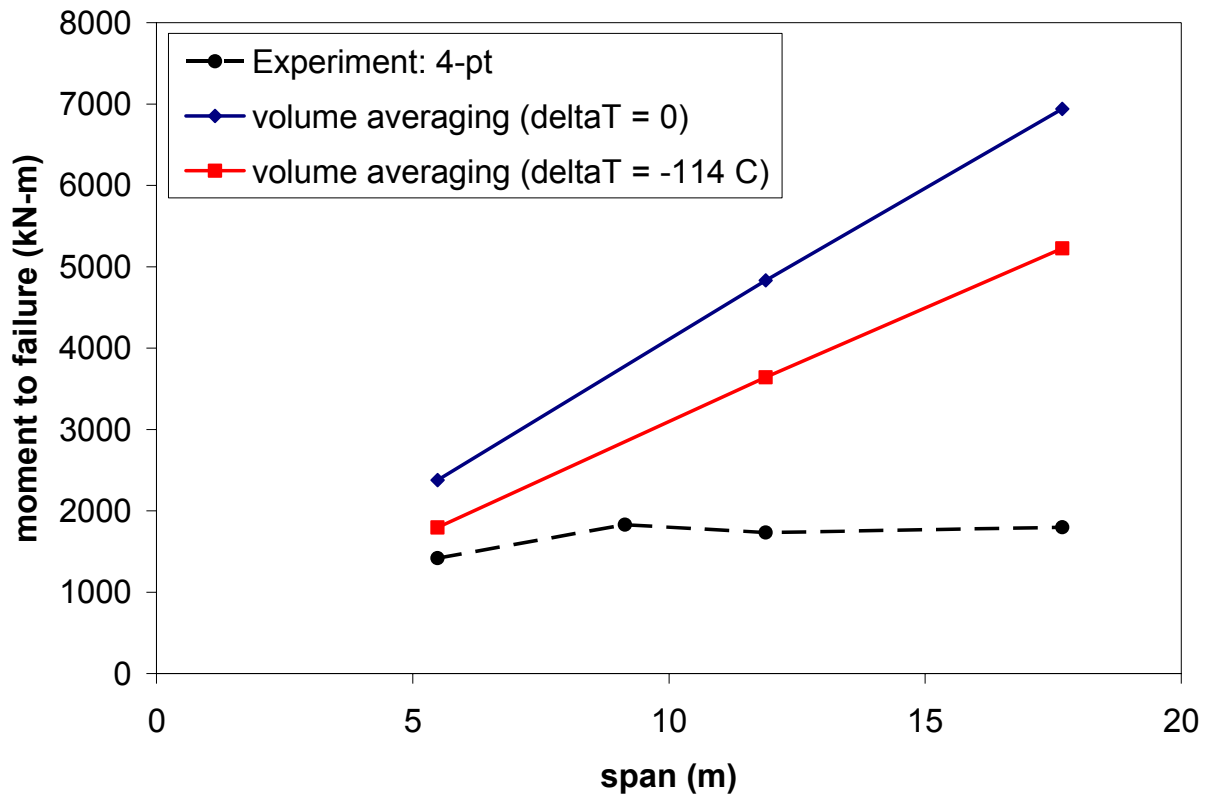


Figure 60. Comparison of the predicted moment capacity vs. span length for the taper edge delamination failure mode using the volume stress averaging technique and the experimental results.

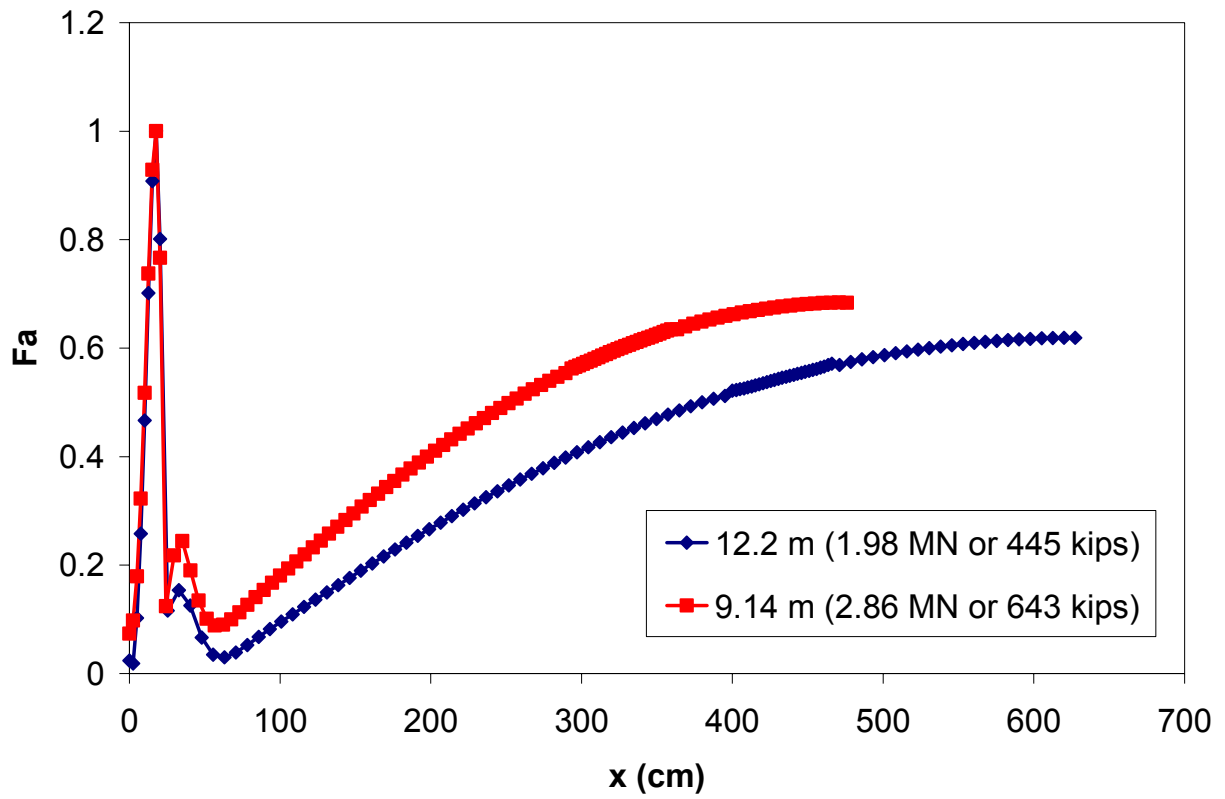


Figure 61. Variation of failure function along the length of the bottom flange using the maximum stress criterion due to a uniformly distributed load (two span lengths shown).

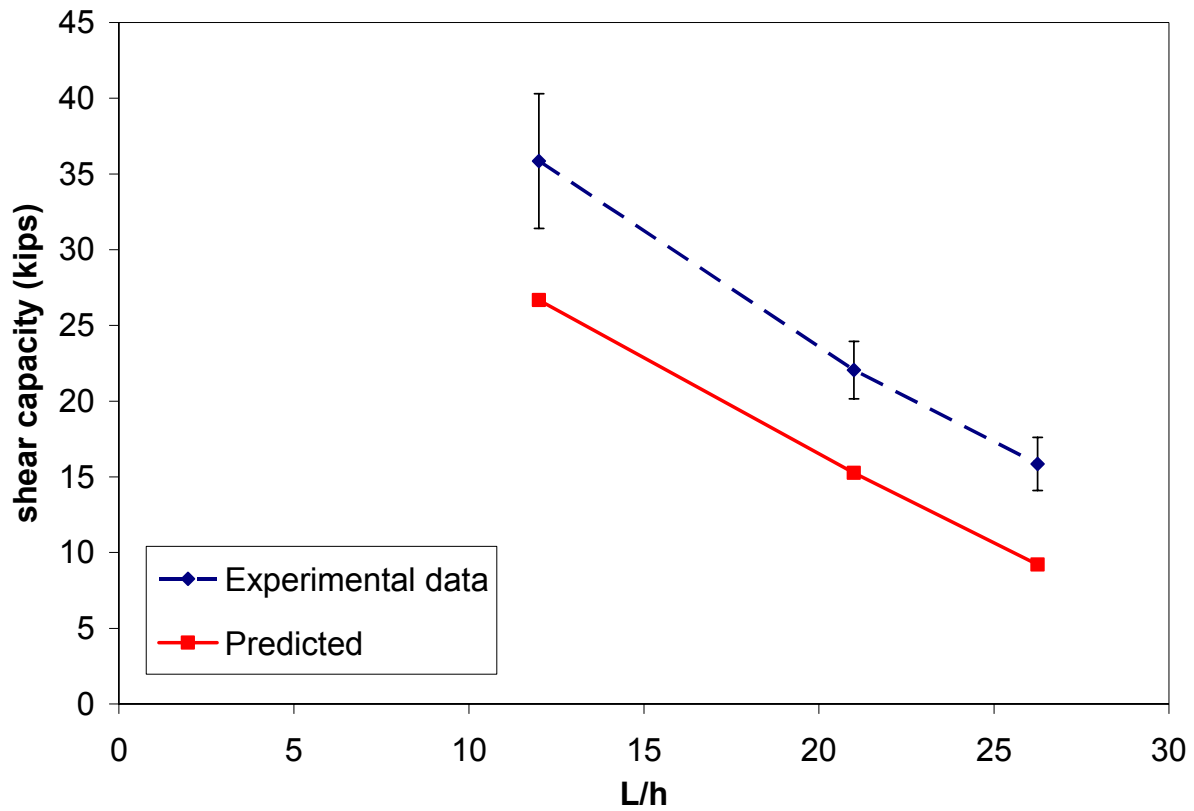


Figure 62. Compression failure predictions for the 8 inch DWB using laminated beam theory.

Table 1. Ply strength values used in the strength and life analyses.

Material	Property	Fiber Volume Fraction	Value	Source
carbon/vinyl ester	$X_{11}^c$	~55%	518 MPa (75.1 ksi)	ELSS testing of DWB flange
	$X_{12}^s$	55-58%	41.4 MPa (6 ksi)	Verghese [80]
unidirectional glass/vinyl ester	$X_{11}^t$	56%	965 MPa (140 ksi)	Phifer [12]
	$X_{22}^t$		41.2 MPa (5.97 ksi)	
	$X_{12}^s$		54.8 MPa (7.94 ksi)	

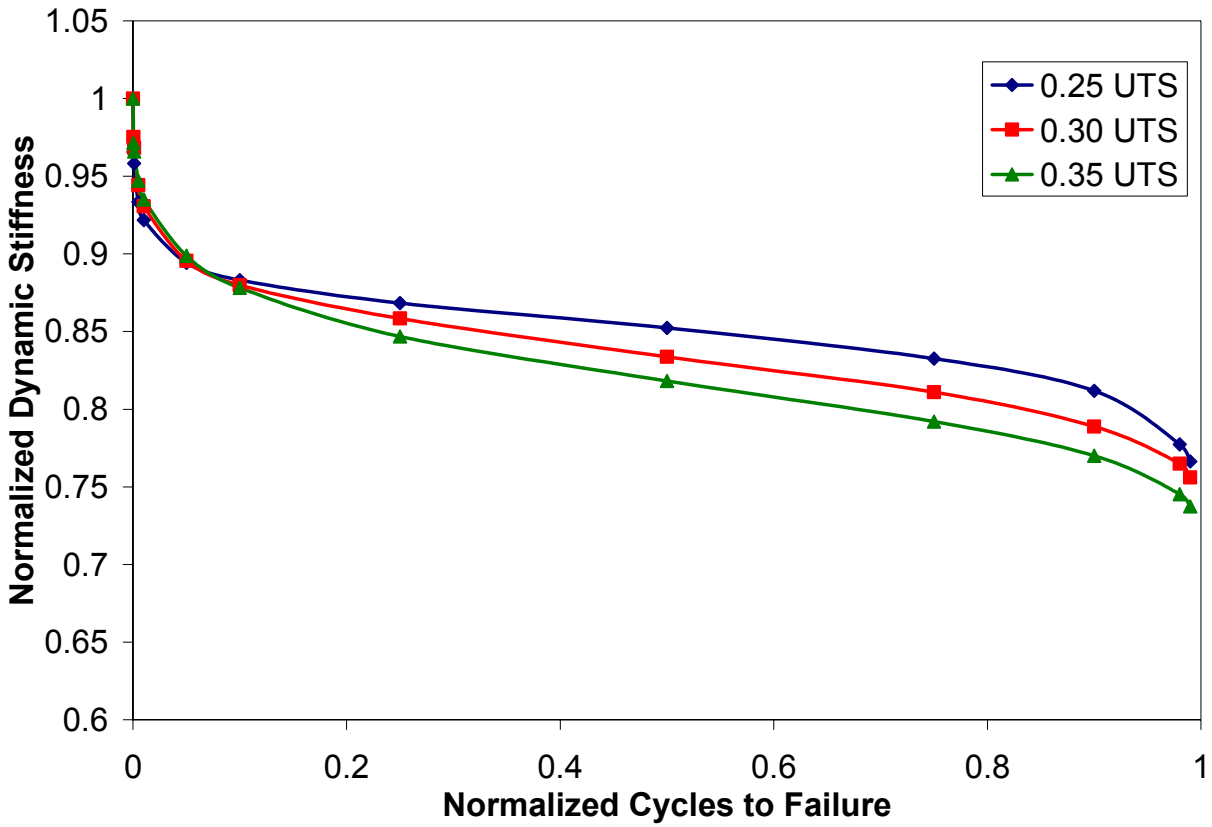


Figure 63. Stiffness reduction data for the quasi-isotropic laminate of Post et al. [83] normalized with respect to ultimate failure load and life.

Table 2. Summary of Fa ranges for off-axis plies at three applied load levels.

Load per patch		bottom flange		bottom sub-flange
		90° plies	45° plies	90° plies
30 kips	min Fa:	0.53	0.41	0.43
	max Fa:	0.66	0.48	0.56
60 kips	min Fa:	0.54	0.40	0.42
	max Fa:	0.81	0.55	0.62
90 kips	min Fa:	0.55	0.39	0.41
	max Fa:	0.97	0.62	0.67

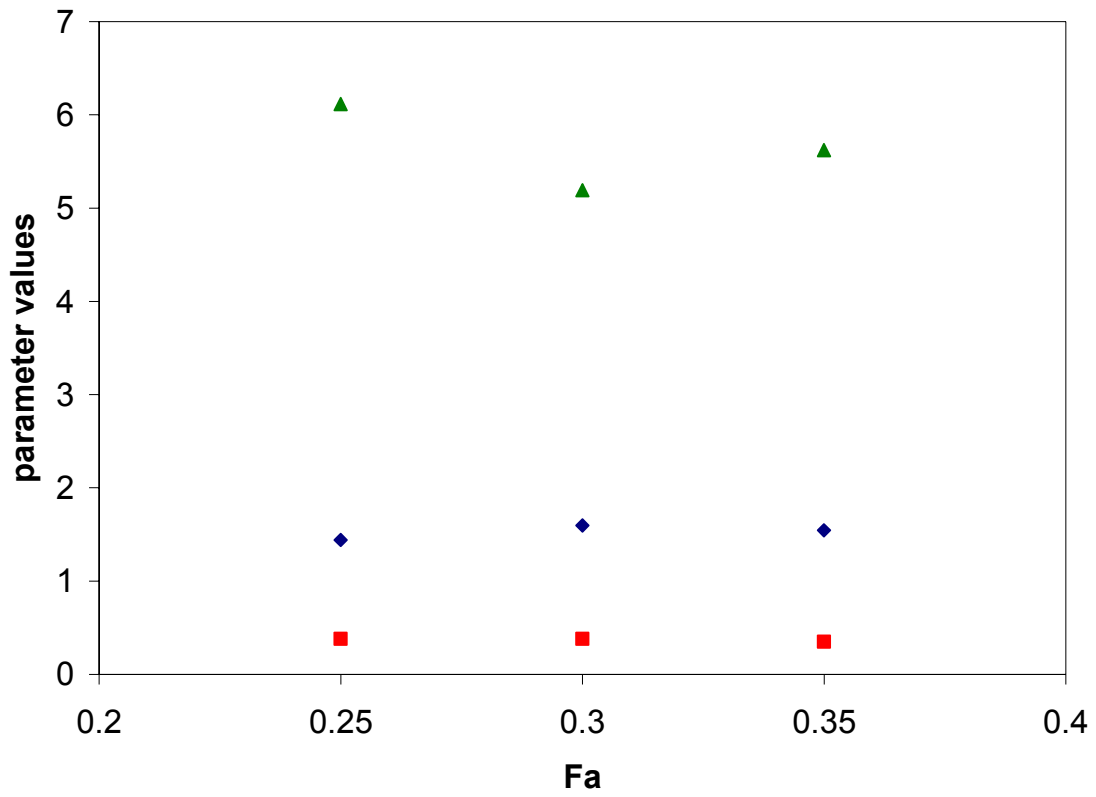


Figure 64. Stiffness reduction fit parameters  $N_2$ ,  $m_1$ , and  $m_2$  versus  $Fa$ .

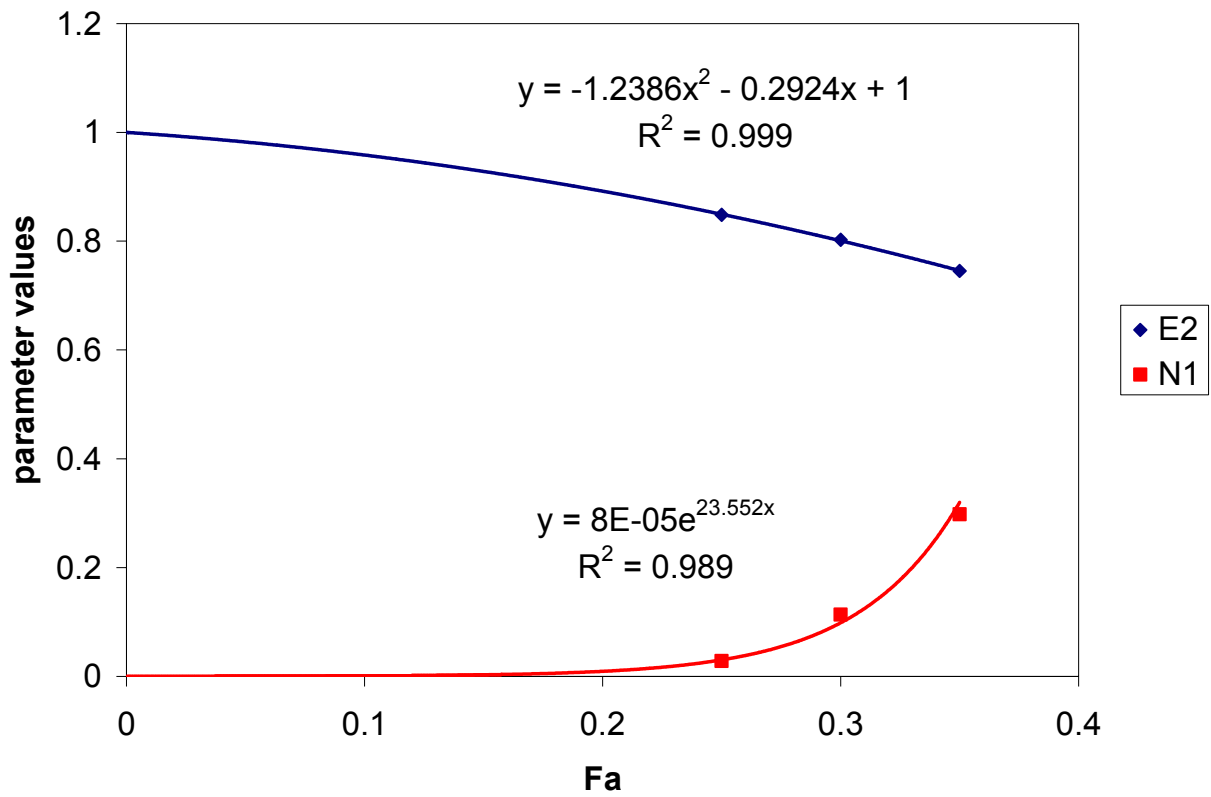


Figure 65. Stiffness reduction fit parameters  $E_2$  and  $N_1$  versus  $Fa$ .

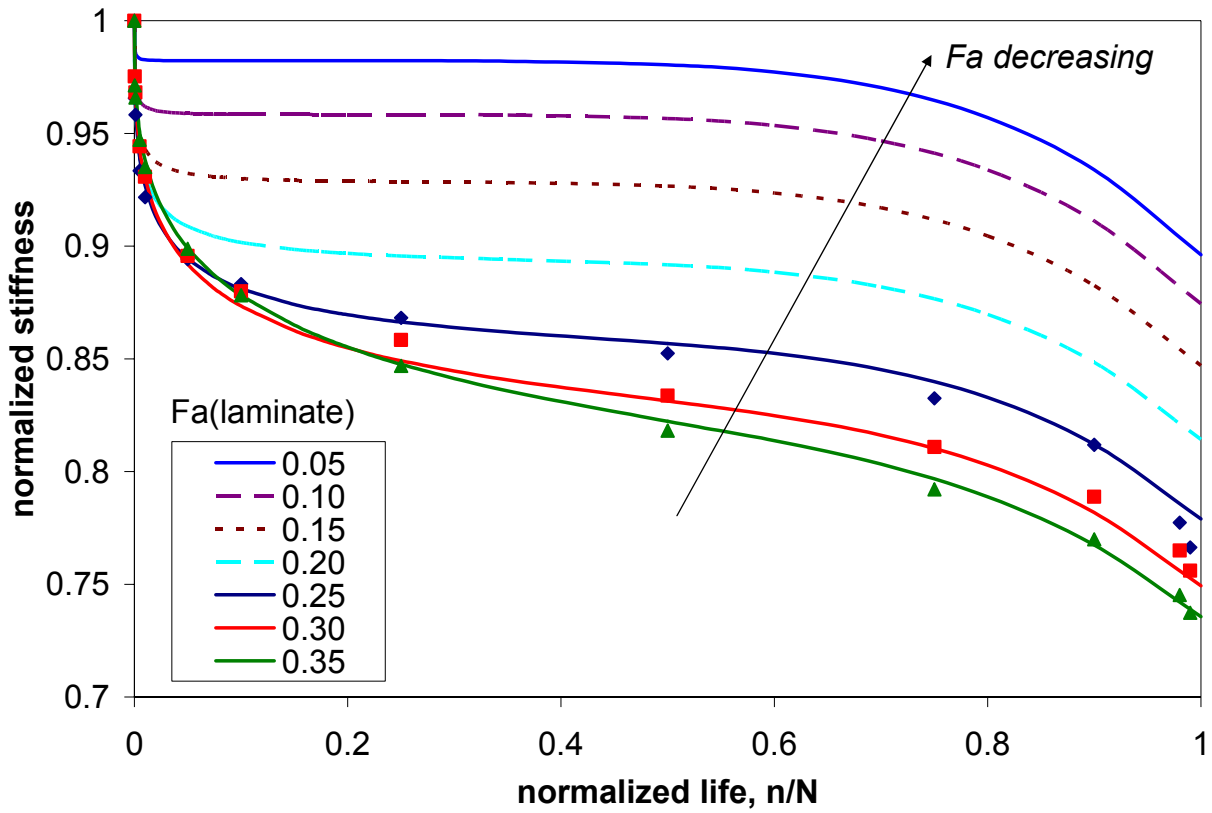


Figure 66. Estimated stiffness reduction curves extrapolated from the dynamic stiffness data of Reference [83].

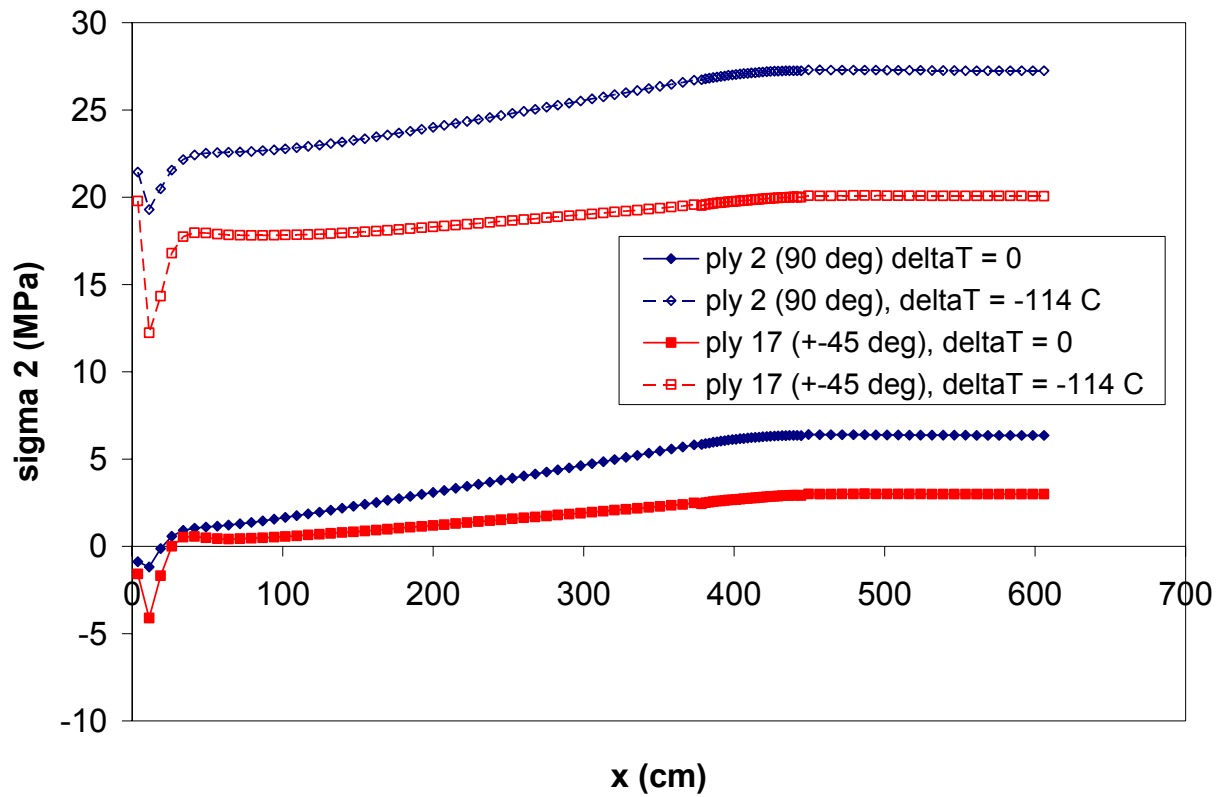


Figure 67. Effect of modeling  $\Delta T$  on the ply-level, transverse stress along the length of half of the beam in the outer 90° and CSM plies of the bottom flange (100 kips).

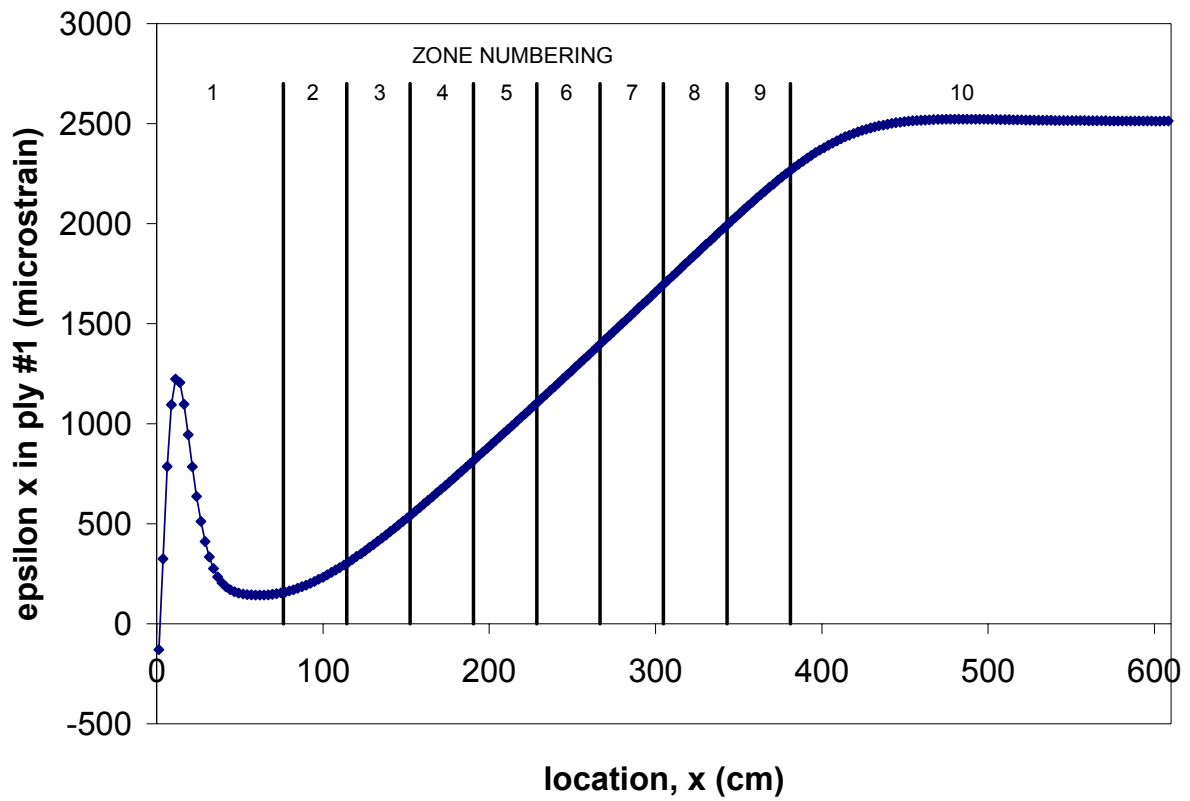


Figure 68. Zone definitions for applying stiffness reductions in off-axis plies. Axial strain for outermost carbon layer shown.

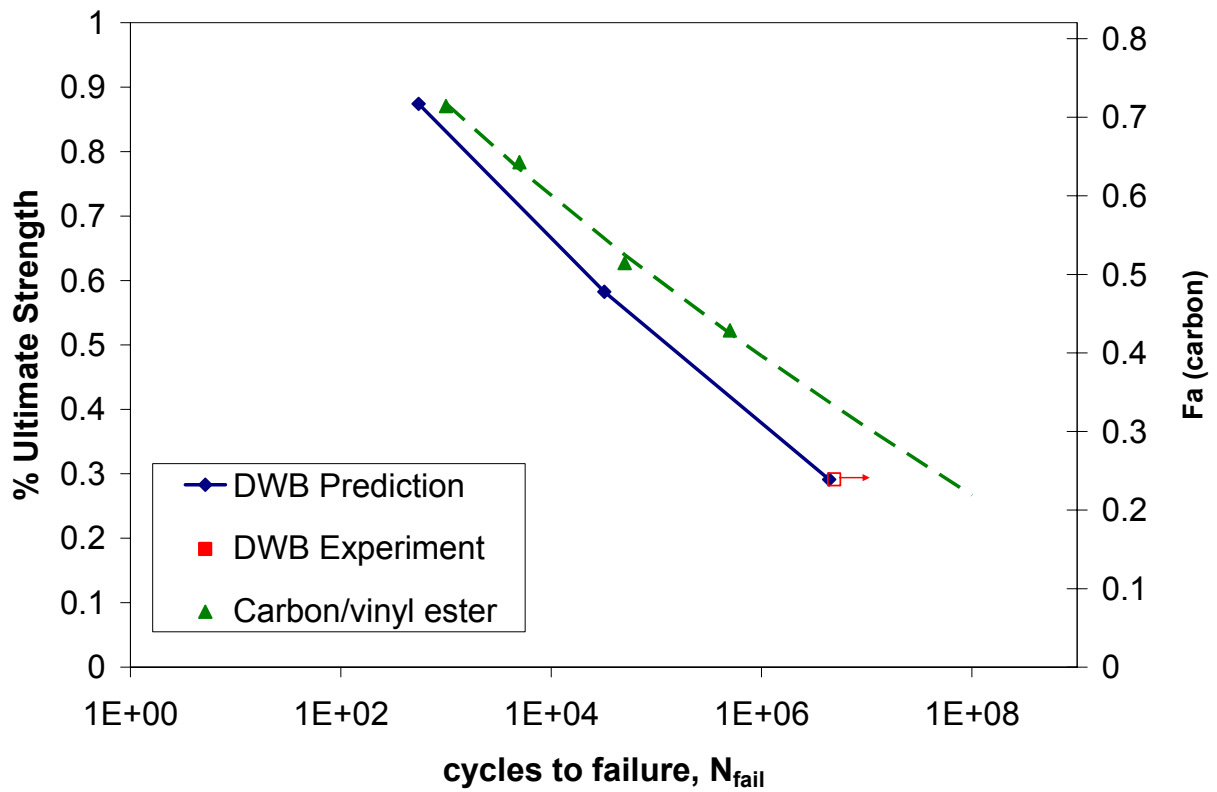


Figure 69. Predicted fatigue life S-N curve for the 11.9 m (39 ft) four-point loading geometry, compared with the experimental data and the carbon fiber fatigue life curve from Verghese [80]

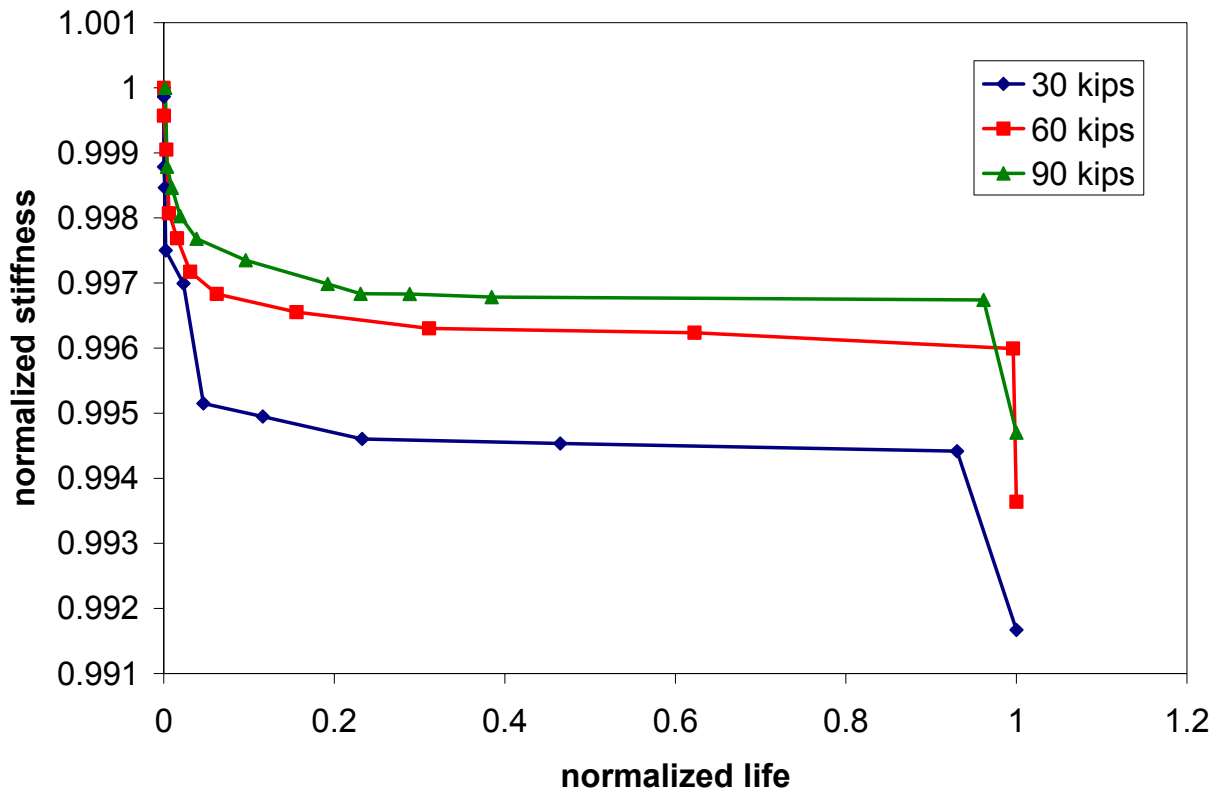


Figure 70. Normalized stiffness reduction vs. normalized life for three load levels.

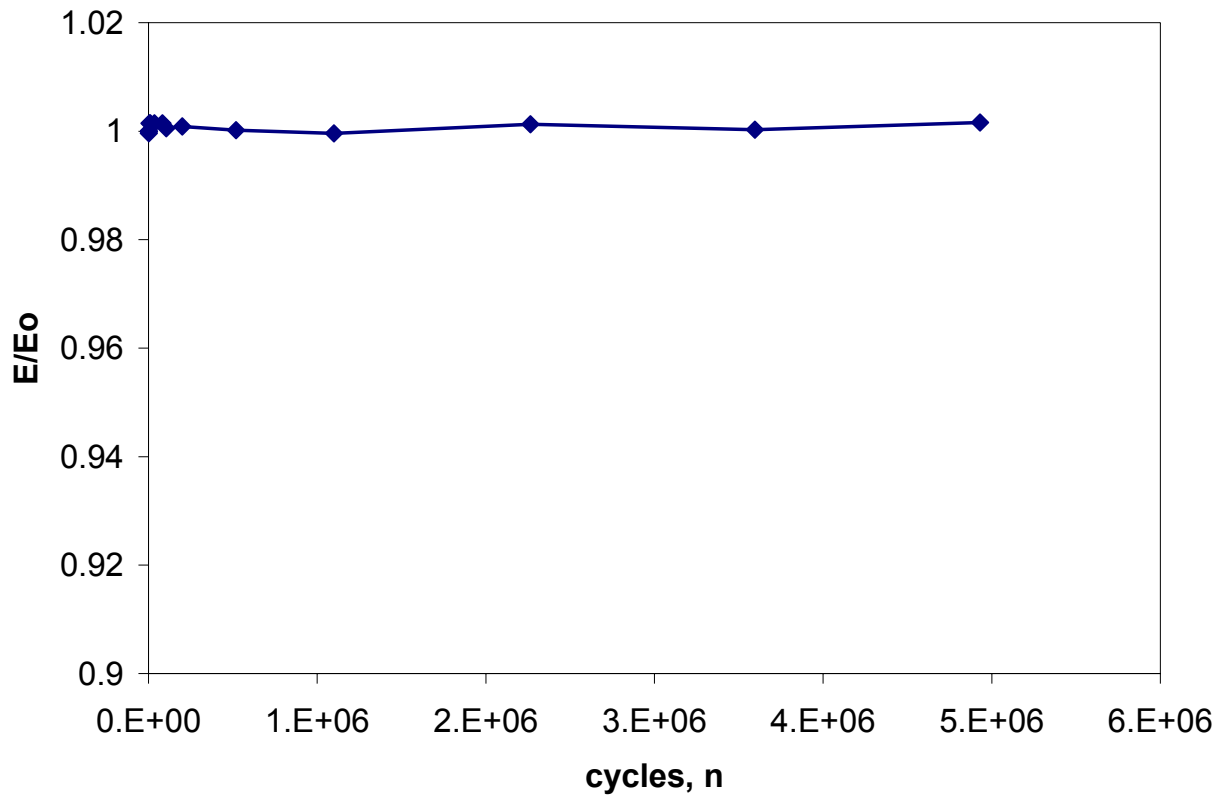


Figure 71. Normalized stiffness reduction for the experimental fatigue test at 30% ultimate capacity.

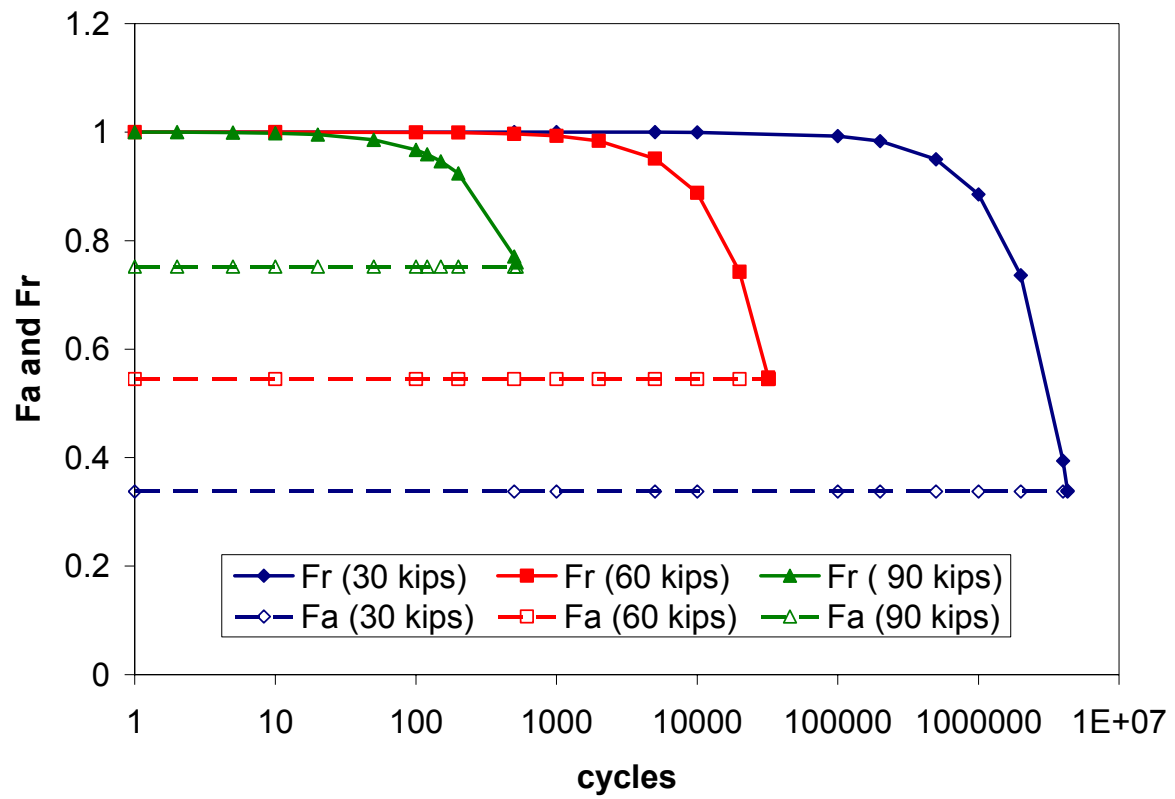


Figure 72. Remaining strength curves for three load levels.

## References

1. Hayes, M.D., et al., *Laboratory and field testing of composite bridge superstructure*. Journal of Composites for Construction, 2000. **4**(3 Aug): p. 120-128.
2. Strongwell, *EXTREN DWB<sup>TM</sup> Design Guide*. 2000.
3. Schniepp, T.J., *Design Manual Development for a Hybrid, FRP Double-Web Beam and Characterization of Shear Stiffness in FRP Composite Beams*, in *Engineering Mechanics*. 2002, Virginia Polytechnic Institute and State University: Blacksburg, Virginia.
4. Senne, J., *Fatigue Life of Hybrid FRP Composite Beams*, in *Engineering Science and Mechanics*. 2000, Virginia Tech: Blacksburg.
5. Pagano, N.J. and R.B. Pipes, *Some observations on the interlaminar strength of composite laminates*. International Journal of Mechanical Sciences, 1973. **15**(8): p. 679-88.
6. Pagano, N.J., *Interlaminar Response of Composite Materials*. Composite Materials Series, 1989.
7. Kassapoglou, C. and P.A. Lagace, *An efficient method for the calculation of interlaminar stresses in composite materials*. Journal of Applied Mechanics-Transactions of the ASME, 1986. **53**(4): p. 744-50.
8. Kassapoglou, C. and P.A. Lagace, *Closed form solutions for the interlaminar stress field in angle-ply and cross-ply laminates*. Journal of Composite Materials, 1987. **21**(4): p. 292-308.
9. Kassapoglou, C., *Determination of interlaminar stresses in composite laminates under combined loads*. Journal of Reinforced Plastics & Composites, 1990. **9**(1): p. 33-58.
10. Brewer, J.C. and P.A. Lagace, *Quadratic Stress Criterion for Initiation of Delamination*. Journal of Composite Materials, 1988. **22**: p. 1141-1155.
11. Reifsnider, K.L. and S.W. Case, *Damage Tolerance and Durability of Material Systems*. 1st ed. 2002, New York: Wiley-Interscience. 435.
12. Phifer, S.P., *Quasi-Static and Fatigue Evaluation of Pultruded Vinyl Ester/E-Glass Composites*, in *Engineering Mechanics*. 1998, Virginia Polytechnic Institute and State University: Blacksburg, VA.
13. Sims, G.D., A.F. Johnson, and R.D. Hill, *Mechanical and Structural Properties of a GRP Pultruded Section*. Composite Structures, 1987. **8**: p. 173-187.
14. Mottram, J.T., *Evaluation of Design Analysis for Pultruded Fibre-Reinforced Polymeric Box Beams*. The Structural Engineer, 1991. **69**(11): p. 211-220.
15. Barbero, E.J., Fu, and Raftoyiannis, *Ultimate Bending Strength of Composite Beams*. Journal of Materials in Civil Engineering, 1991. **3**(4): p. 292-306.

16. Bank, L.C., M. Nadipelli, and T.R. Gentry, *Local Buckling and Failure of Pultruded Fiber-Reinforced Plastic Beams*. Journal of Engineering Materials and Technology, 1994. **116**: p. 233-237.
17. Bank, L.C., T.R. Gentry, and M. Nadipelli, *Local Buckling of Pultruded FRP Beams -- Analysis and Design*. Journal of Reinforced Plastics & Composites, 1996. **15**: p. 283-294.
18. Gilchrist, M.D., et al., *Mechanical Performance of Carbon-Fibre- and Glass-Fibre-Reinforced Epoxy I-Beams: I. Mechanical Behavior*. Composite Science and Technology, 1995. **56**(1): p. 37-53.
19. Kant, T. and K. Swaminathan, *Estimation of transverse/interlaminar stresses in laminated composites -- a selective review and survey of current developments*. Composite Structures, 2000. **49**: p. 65-75.
20. Tahani, M. and A. Nosier, *Free edge stress analysis of general cross-ply composite laminates under extension and thermal loading*. Composite Structures, 2003. **60**: p. 91-103.
21. Pipes, R.B. and N.J. Pagano, *Interlaminar stresses in composite laminates under uniform axial extension*. Journal of Composite Materials, 1970. **4**: p. 538-48.
22. Puppo, A.H. and H.A. Evensen, *Interlaminar shear in laminated composites under generalized plane stress*. Journal of Composite Materials, 1970. **4**: p. 204-220.
23. Pagano, N.J. and R.B. Pipes, *The influence of stacking sequence on laminate strength*. Journal of Composite Materials, 1971. **5**: p. 50-7.
24. Rybicki, E.F., *Approximate Three-Dimensional Solutions for Symmetric Laminates Under Inplane Loading*. Journal of Composite Materials, 1971. **5**.
25. Wang, A.S.D. and F.W. Crossman, *Some New Results on Edge Effects in Symmetric Composite Laminates*. Journal of Composite Materials, 1977. **11**: p. 92-106.
26. Wang, S.S. and I. Choi, *Boundary-Layer Effects in Composite Laminates: Part 1 - Free-Edge Stress Singularities*. Journal of Applied Mechanics, 1982. **49**: p. 541-548.
27. Wang, S.S. and I. Choi, *Boundary-Layer Effects in Composite Laminates: Part 2 - Free-Edge Stress Solutions and Basic Characteristics*. Journal of Applied Mechanics, 1982. **49**: p. 549-560.
28. Lin, C., C. Hsu, and C. Ko, *Interlaminar Stresses in General Laminates with Straight Free Edges*. AIAA Journal, 1995. **33**(8): p. 1471-1476.
29. Ko, C.-C. and C.-C. Lin, *Method for calculating interlaminar stresses in symmetric laminates containing a circular hole*. AIAA Journal, 1992. **30**(1): p. 197-204.
30. Webber, J.P.H. and S.K. Morton, *An analytical solution for the thermal stresses at the free edges of laminated plates*. Composite Science and Technology, 1993. **46**: p. 175-185.

31. Connolly, M.P., *Simplified equations for interlaminar stresses in cross-ply laminates*. Journal of Reinforced Plastics & Composites, 1994. **13**(11): p. 1043-1053.
32. Flanagan, G., *An efficient stress function for the free-edge stresses in laminates*. International Journal of Solids & Structures, 1994. **31**(7): p. 941-952.
33. Kim, H.S., M. Cho, and G.-I. Kim, *Free-edge strength analysis in composite laminates by the extended Kantorovich method*. Composite Structures, 2000: p. 229-235.
34. Cho, M. and H.S. Kim, *Iterative free-edge stress analysis of composite laminates under extension, bending, twisting and thermal loadings*. International Journal of Solids and Structures, 2000. **37**: p. 435-459.
35. Cho, M. and J.-Y. Yoon, *Free-Edge Interlaminar Stress Analysis of Composite Laminates by Extended Kantorovich Method*. AIAA Journal, 1999. **37**(5): p. 656-660.
36. Kim, T. and S.N. Atluri, *Interlaminar Stresses in Composite Laminates under Out-of-Plane Shear/Bending*. AIAA Journal, 1994. **32**(8): p. 1700-1708.
37. Rose, C.A. and C.T. Herakovich, *An Approximate Solution for Interlaminar Stresses in Composite Laminates*. Composites Engineering, 1993. **3**(3): p. 271-285.
38. Kim, T. and S.N. Atluri, *Analysis of edge stresses in composite laminates under combined thermo-mechanical loading, using a complementary energy approach*. Computational Mechanics, 1995. **16**: p. 83-97.
39. Kim, R.Y. and S.R. Soni, *Experimental and Analytical Studies on the Onset of Delamination in Laminated Composites*. Journal of Composite Materials, 1984. **18**: p. 70-80.
40. Whitney, J.M. and R.J. Nuismer, *Stress Fracture Criteria for Laminated Composites Containing Stress Concentrations*. Journal of Composite Materials, 1974. **8**: p. 253-265.
41. Kim, R.Y. and S.R. Soni. *Failure of Composite Laminates Due to Combined Interlaminar Normal and Shear Stresses*. in *Composites '86: Recent Advances in Japan and the United States*. 1986.
42. Pipes, R.B. and N.J. Pagano, *Interlaminar stresses in composite laminates-an approximate elasticity solution*. Journal of Applied Mechanics, 1974. **41**(3): p. 668-672.
43. Mandell, J.F., G.B. McKenna, and F.J. McGarry. *Interlaminar Strength and Toughness of Fiberglass Laminates*. in *29th Annual Technical Conference, The Society of the Plastics Industry*. 1974.
44. Lagace, P.A. and D.B. Weems, *A Through-the-Thickness Strength Specimen for Composites*. Test Methods for Design Allowables for Fibrous Composites: 2nd Volume, ASTM STP 1003, ed. C.C. Chamis. 1989, Philadelphia: American Society for Testing and Materials.

45. *Standard Test Method for Apparent Interlaminar Shear Strength of Parallel Fiber Composites by Short-Beam Method*. 2000. p. 41-48.
46. *Standard Test Method for Shear Properties of Composite Materials by the V-Notched Beam Method*. 1998. p. 232-244.
47. He, K., S.V. Hoa, and R. Ganesan, *The study of tapered laminated composite structures: a review*. *Composites Science & Technology*, 2000. **60**: p. 2643-2657.
48. Hoa, S.V., J. Daoust, and B.L. Du, *Interlaminar Stresses in Tapered Laminates*. *Polymer Composites*, 1988. **9**(5): p. 337-344.
49. Wu, C.M.L. and J.P.H. Webber, *Analysis of Tapered (In Steps) Laminated Plates Under Uniform Inplane Load*. *Composite Structures*, 1986. **5**: p. 87-100.
50. Her, S.-C., *Stress analysis of ply drop-off in composite structures*. *Composite Structures*, 2002. **57**: p. 235-244.
51. Daoust, J. and S.V. Hoa, *Parameters Affecting Interlaminar Stresses in Tapered Laminates Under Static Loading Conditions*. *Polymer Composites*, 1989. **10**(5): p. 374-383.
52. Thomsen, O.T., et al., *Ply drop-off effects in CFRP/honeycomb sandwich panels - theory*. *Composites Science & Technology*, 1996. **56**(4 Apr): p. 407-422.
53. Thomsen, O.T., et al., *Ply drop-off effects in CFRP/honeycomb sandwich panels - experimental results*. *Composites Science & Technology*, 1996. **56**(4 Apr): p. 423-437.
54. Vizzini, A.J. and S.W. Lee, *Damage Analysis of Composite Tapered Beams*. *Journal of the American Helicopter Society*, 1995. **40**(2): p. 43-49.
55. Vizzini, A.J., *Strength of Laminated Composites with Internal Discontinuities*. *AIAA Journal*, 1992. **30**(6): p. 1515-1520.
56. Reeder, J.R., *A Bilinear Failure Criterion for Mixed-Mode Delamination*, in *Composite Materials: Testing and Design (Eleventh Volume)*, ASTM STP 1206, E.T. Camponeschi, Editor. 1993, American Society of Testing and Materials: Philadelphia. p. 303-322.
57. Miravete, A. and M.A. Jiménez, *Application of the Finite Element Method to Prediction of Onset of Delamination Growth*. *Applied Mechanics Review*, 2002. **55**(2): p. 89-106.
58. *ASTM D 5528 - 01: Standard Test Method for Mode I Interlaminar Fracture Toughness of Unidirectional Fiber-Reinforced Polymer Matrix Composites*. 2002. p. 292-302.
59. Davies, P., B.R.K. Blackman, and A.J. Brunner, *Standard Test Methods for Delamination Resistance of Composite Materials: Current Status*. *Applied Composite Materials*, 1998. **5**: p. 345-364.

60. O'Brien, T.K., *Characterization of Delamination Onset and Growth in a Composite Laminate*, in *Damage in Composite Materials*, ASTM STP 775, K.L. Reifsnider, Editor. 1982, American Society of Testing and Materials. p. 140-167.
61. O'Brien, T.K., *Mixed-Mode Strain-Energy-Release Rate Effects on Edge Delamination of Composites*, in *Effects of Defects in Composite Materials*, ASTM STP 836. 1984, American Society of Testing and Materials. p. 125-142.
62. Rybicki, E.F. and M.F. Kanninen, *A Finite Element Method Calculation of Stress Intensity Factors by a Modified Crack Closure Technique*. Engineering Fracture Mechanics, 1977. **9**: p. 931-938.
63. Raju, I.S., *Calculation of Strain-Energy Release Rates with Higher Order and Singular Finite Elements*. Engineering Fracture Mechanics, 1987. **28**(3): p. 251-274.
64. Tay, T.E., *Characterization and Analysis of Delamination Fracture in Composites: An Overview of Developments from 1990 to 2001*. Applied Mechanics Review, 2003. **56**(1): p. 1-32.
65. Krueger, R., *The Virtual Crack Closure Technique: History, Approach and Applications*. 2002, ICASE, NASA: Hampton, Virginia.
66. Krueger, R., et al., *Fatigue Life Methodology for Bonded Composite Sking/Stringer Configurations*. 2001, ICASE, NASA: Hampton, Virginia.
67. Raju, I.S., R. Sistla, and T. Krishnamurthy, *Fracture Mechanics Analyses for Skin-Stiffener Debonding*. Engineering Fracture Mechanics, 1996. **54**(3): p. 371-385.
68. Krueger, R., T.K. O'Brien, and P.J. Minguet. *Application of the Shell/3D Modeling Technique for the Analysis of Skin-Stiffener Debond Specimens*. in *American Society for Composites 17th Technical Conference*. 2002. Purdue University: CRC Press.
69. Case, S.W., *Mechanics of Fiber-Controlled Behavior in Polymeric Composite Materials*, in *Engineering Mechanics*. 1996, Virginia Polytechnic Institute and State University: Blacksburg, Virginia.
70. Reifsnider, K. and W.W. Stinchcomb, *A Critical Element Model of the Residual Strength and Life of Fatigue-Loaded Composite Coupons*, in *Composite Materials: Fatigue and Fracture*, ASTM STP 907, H.T. Hahn, Editor. 1986, American Society for Testing and Materials: West Conshohocken, PA. p. 298-303.
71. Adams, D.F. and G.A. Finley, *Analysis of Thickness-Tapered Unidirectional Composite Compression Specimens*. Journal of Composite Materials, 1997. **31**(22): p. 2283-2308.
72. Bogetti, T., J.W. Gillespie, and R.B. Pipes, *Evaluation of the IITRI Compression Test Method for Stiffness and Strength Determination*. Composites Science and Technology, 1988. **32**(1): p. 57-76.

73. *The Composite Materials Handbook MIL-17*. 2002.
74. Hashin, Z., *Failure Criteria for Unidirectional Fiber Composites*. Journal of Applied Mechanics, 1980. **47**: p. 329-334.
75. Williams, B.Y., M.D. Hayes, and J.J. Lesko, *Measurement of the Interlaminar Strength of the 36" Double Web Beam Flange*. 2002, Virginia Tech: Blacksburg, VA. p. 11.
76. Adams, D.F. and E.Q. Lewis, *Experimental Assessment of Four Composite Material Shear Test Methods*. Journal of Testing and Evaluation, 1997. **25**(2): p. 174-181.
77. O'Brien, T.K., *Generic Aspects of Delamination in Fatigue of Composite Materials*. Journal of the American Helicopter Society, 1987. **32**: p. 13-18.
78. Smith, G., *The Determination of the Interlaminar Fracture Toughness of Hybrid, Composite Beams*. 2003, Virginia Polytechnic Institute and State University: Blacksburg, Virginia.
79. Pagano, N.J. and S.R. Soni, *Global-Local Laminate Variational Model*. International Journal of Solids and Structures, 1983. **19**(3): p. 207-228.
80. Verghese, K.E., *Durability of Polymer Matrix Composites for Infrastructure: The Role of the Interphase*, in *Materials Engineering Science*. 1999, Virginia Polytechnic Institute and State University: Blacksburg, VA.
81. Lesko, J.J., *Interphase Properties and Their Effects on the Compression Mechanics of Polymeric Composites*, in *Engineering Mechanics*. 1994, Virginia Polytechnic Institute and State University: Blacksburg, Virginia.
82. Case, S., *Personal Communication: Alternate Forms of the Strength Evolution Integral*. 2003.
83. Post, N. and J. Bausano, *Personal communication: Stiffness reduction data for a glass/vinyl ester laminate*. 2003.
84. Aklonis, J.J., W.J. MacKnight, and M. Shen, *Introduction to Polymer Viscoelasticity*. 1972, New York: Wiley-Interscience.
85. Reifsnider, K., *Class Notes, "Mechanics of Composite Strength and Life"*. 2002.

## **Vita**

Michael David Hayes was born on October 26, 1972 to Jim and Sharon Hayes in Nashville, Tennessee. He grew up in Knoxville, Tennessee and graduated Farragut High School as a valedictorian in 1991. He obtained a B.S. in Engineering Science and Mechanics from Virginia Tech in 1995, and then pursued a Master's degree in Engineering Mechanics with special emphasis on composite materials. Upon completion of his M.S. in 1997, Michael went to work for Michelin Americas Research and Development Corporation in Greenville, South Carolina as a Materials Engineer. After two years, he returned to Blacksburg to earn a Ph.D. at Virginia Tech. Nine days after defending his dissertation on Thanksgiving Day, Michael proposed to Amy, his girlfriend of six years. Up graduation, Michael will join Amy in Atlanta, Georgia to pursue employment.